



UNIVERSITY OF CRETE
INTER-INSTITUTIONAL
POSTGRADUATE STUDY PROGRAMME
«OPTICS & VISION»



Development and Optimization of a High-Resolution Small Angle Light Scattering setup for Rheological applications

Thesis submitted to the Medicine school of University of Crete
in partial fulfillment of the requirements for the
Master of Science in Optics and Vision.

PETROS CHATZAKIS

Supervising Committee

Petekidis George

Associate Professor, Materials Science and Technology Department, UoC.

Papazoglou Dimitris

Assistant Professor, Materials Science and Technology Department, UoC

Fytas George

Professor, Materials Science and Technology Department, UoC

Heraklion – 2015

ABSTRACT

A high resolution Small Angle Light Scattering (SALS) setup that can be used in combination with rheology was optically designed and developed. The objective was a compact device that would cover a wider angular (2° - 30°) and q vector ($0.4\mu\text{m}^{-1}$ - $6.2\mu\text{m}^{-1}$) range than that typically covered by SALS and would be easily adapted as a modular accessory to commercially available rheometers. The setup was optically and mechanically designed and finally realized. It was successfully calibrated and verified for its angular performance, with a diffraction grating and a pinhole, while a novel way of correction, accounting for sample's thickness and vignetting, was produced. Homemade analysis software was also developed to accompany the setup, having a user friendly graphic interface and various capabilities. The performance of the apparatus was evaluated by measuring and analyzing the scattering profiles of a variety of dilute colloidal suspensions with different thicknesses, particle sizes and materials and different solvents, at rest. Preliminary measurements of concentrated colloidal suspensions were also performed at rest and under oscillatory shear, to show the setup's capabilities in combination with rheology. The setup's ability, with the addition of an extra component, to image the sample and perform Dark Field Microscopy (DFM) or Diffusing Wave Spectroscopy (DWS) measurements, was also tested with success.

Περίληψη

Μία υψηλής ανάλυσης διάταξη σκέδασης φωτός σε μικρές γωνίες (SALS) που μπορεί να χρησιμοποιηθεί σε συνδυασμό με τη ρεολογία, σχεδιάστηκε οπτικά και αναπτύχθηκε. Στόχος ήταν μία συσκευή που θα καλύπτει ένα ευρύτερο γωνιακό εύρος (2° - 30°) από ότι συνήθως καλύπτεται από διατάξεις SALS και θα προσαρμόζεται εύκολα σαν πρόσθετο, σε εμπορικά διαθέσιμα ρεόμετρα. Η διάταξη σχεδιάστηκε οπτικά και μηχανικά και τελικά κατασκευάστηκε. Βαθμονομήθηκε και ελέγχθηκε για τη γωνιακή της απόδοση, με ένα φράγμα περίθλασης και μία οπή, ενώ ένας νέος τρόπος διόρθωσης, για το πάχος του δείγματος και τη σκίαση (vignetting), παρήχθη. Επίσης, ένα λογισμικό ανάλυσης αναπτύχθηκε για να συνοδεύει τη διάταξη, έχοντας ένα φιλικό προς το χρήστη γραφικό περιβάλλον και διάφορες δυνατότητες. Η απόδοση της συσκευής αξιολογήθηκε με τη μέτρηση και ανάλυση των προφίλ σκέδασης από μία ποικιλία αραιών δειγμάτων με διαφορετικά πάχη, μεγέθη σωματιδίων και υλικών και διαφόρων διαλυτών, σε κατάσταση ηρεμίας. Επίσης πραγματοποιήθηκαν μετρήσεις δειγμάτων με υψηλότερα κλάσματα όγκου σε κατάσταση ηρεμίας και υπό διάτμηση, για να αναδειχθούν οι δυνατότητες της διάταξης σε συνδυασμό με τη ρεολογία. Η ικανότητα της διάταξης, με την προσθήκη ενός επιπλέον εξαρτήματος, να απεικονίζει το δείγμα και να εκτελεί μετρήσεις μικροσκοπίας σκοτεινού πεδίου (Dark Field Microscopy - DFM) ή σπεκτροσκοπίας διάχυσης (Diffusing Wave Spectroscopy - DWS), δοκιμάστηκε επίσης με επιτυχία.

TABLE OF CONTENTS

Abstract	3
Περίληψη	3
CHAPTER 1 Introduction.....	6
CHAPTER 2 Light Scattering Theory	11
2.1 Definitions.....	11
2.2 Light Scattering by Particles	12
2.3 Rayleigh Theory.....	13
2.4 Rayleigh - Gans - Debye (RGD) Theory	13
2.5 Mie Theory.....	17
CHAPTER 3 Development.....	21
3.1 Aim – Limitations	21
3.2 Optical Design	25
3.2.1 Optimization	25
3.2.2 Final Optimized Layout	34
3.3 Mechanical / Opto-mechanical Design	40
3.4 SALSq05 Setup Realization	43
3.5 Angular Calibration	46
3.5.1 Calibration using a Diffraction Grating	46
3.5.2 Calibration Verification using a Pinhole.....	48
3.6 Depth of Field Correction	50
CHAPTER 4 Dilute Colloidal Suspensions.....	54
4.1 Samples	54
4.2 Measurement & Analysis.....	55
4.3 Standard Deviation Alternative Analysis.....	58
4.4 Evaluation Tests Results	61
4.5 Dark Field Microscopy (DFM).....	68

CHAPTER 5 Concentrated Colloidal Suspensions	70
5.1 Static Light Scattering (SLS)	70
5.1.1 Measurements At Rest	70
5.1.2 Measurements Under Shear	73
5.2 Diffusing Wave Spectroscopy (DWS).....	76
CHAPTER 6 Conclusions.....	78
Appendix Camera Evaluation	80
Bibliography	83

CHAPTER 1

INTRODUCTION

Light Scattering Methods

Light scattering methods are a powerful tool for investigating the structure and the dynamics of soft and biological matter. Typical applications include particle sizing^{1,2}, the characterization of aggregation phenomena³, the determination of interparticle interactions, the investigation of the structure and the relaxation dynamics of complex fluids⁴⁻⁶. The typical space scales, that are probed, range from tens of nanometers to tens of microns, depending on the range of scattering angles each setup is optimized to cover.

In light scattering, the probed sample is typically illuminated by a laser beam, while photodiodes, photomultipliers or CCD - CMOS cameras are used to detect the scattered light (Fig. 1.1 left). Scattering methods can be divided in two categories: static and dynamic light scattering. In static light scattering (SLS)⁵, the structure of a sample is probed by measuring the time-averaged scattered intensity as a function of the scattering angle, while dynamic light scattering (DLS)⁶ reveals the sample's dynamics by measuring the temporal fluctuations of the scattered intensity (Fig. 1.1 right).

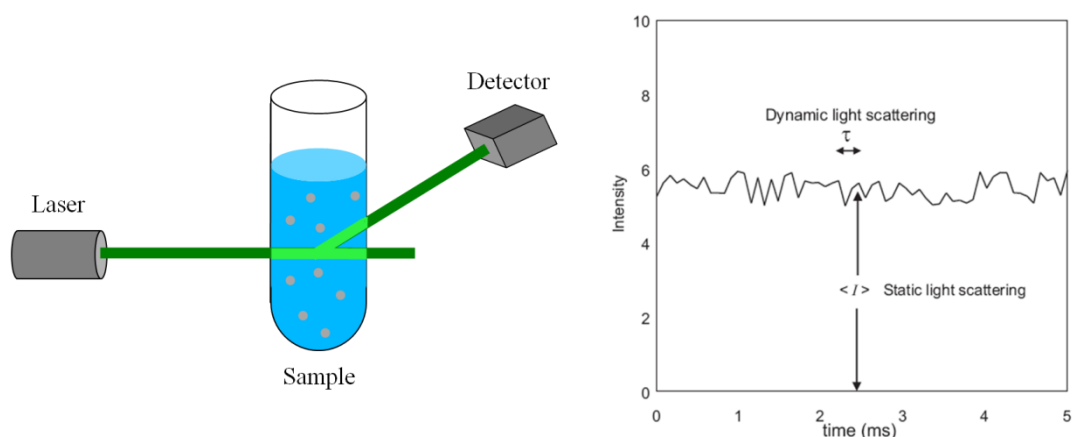


Fig. 1.1 In light scattering a sample is illuminated by a laser beam and the scattered light is detected by a photon multiplier or a CCD camera (left). Scattered intensity measurement at a certain scattering angle over time (right). SLS experiments analyze the average of the scattered intensity over time at various angles, while in DLS the temporal fluctuations of the scattered intensity are of interest.

A wide variety of light scattering setups have been developed, many of which are commercially available. Two main categories of setups exist, according to the range of scattering angles they are designed to cover. Wide angle light scattering (WALS) setups, cover approximately the range from 10 to 150 degrees. It should be noted that in practice it is difficult to obtain reliable data below 20 degrees. WALS setups are based on a goniometer to vary the scattering angle and are typically consisted of the following components: (1) the incident light source, typically a laser, (2) the light scattering cell, in most cases a cylindrical quartz glass cuvette, (3) the detector, either a photo multiplier tube (PMT) or an avalanche photo diode (APD) and its associated optics (pinhole or optical fiber), mounted on the arm of the goniometer and (4) the electronic hardware components associated with the detector used for signal processing (computer, hardware correlator, etc)⁵. The detector measures the scattered intensity from a sample at a certain angle at a time (Fig. 1.2).

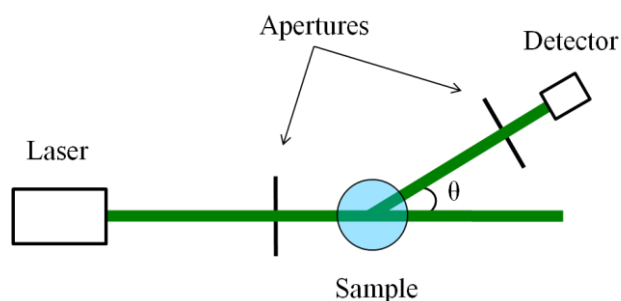


Fig. 1.2 Wide angle light scattering geometry.

Small angle light scattering setups (SALS) are designed for measurements close to the forward direction, usually covering up to 10 degrees of scattering angles. However, the past few years, SALS setups that cover scattering angles up to about 25 degrees, have been developed to fill the gap between the range of scattering angles of typical WALS and SALS setups. Overlapping WALS and SALS can be very useful, since absolute intensity measurements are difficult in light scattering, especially for SALS, making it difficult to merge data from different setups on the same scale⁷. Unlike WALS, SALS geometry (Fig. 1.3) enables measuring the 2D scattering pattern of the sample, since each scattering angle is represented on the screen by a circle centered on the axis of the incident beam⁴. Measurements of different angles are implemented simultaneously.

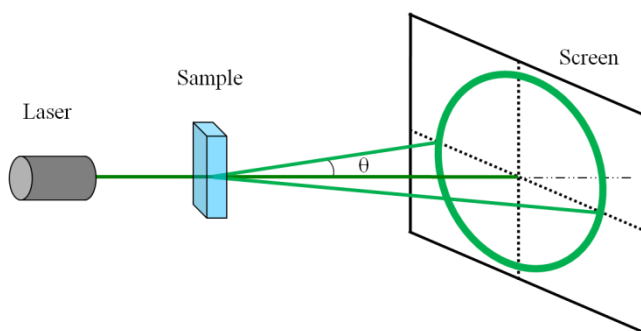


Fig. 1.3 Small angle light scattering geometry.

Small Angle Light Scattering (SALS)

Early SALS experiments⁸ simply photographed the pattern of scattered light falling on a screen (Fig. 1.3). It was required to eliminate the incident beam with either a beam stop or by creating an aperture on the screen that was letting the unscattered beam simply pass through. To obtain quantitative measurements of the scattered light, two-dimensional (2D) detectors were later used^{9,10}.

During the last years, a rapid development of small angle scattering techniques (SALS) is observed. This development is essentially related to the progress in charge-coupled device (CCD) sensor technology and to the increasing interest in the study of systems inhomogeneous on length scales of the order or larger than the wavelength of light. Systems with structural properties on these length scales include for example colloidal aggregates, gels and glasses, soft matter systems undergoing a spinodal decomposition, polymer blends, emulsions, foams, red blood cells, vesicles etc. It is also worth mentioning that SALS has immediate applications to the problem of particle sizing for practical and industrial applications like environmental pollution monitoring¹¹.

Some examples of SALS layouts are shown in Figure 1.4. In the top scheme (a), adopted for example by Caprinetti et al (1990)¹² and Romo-Uribe et al (2010)¹³, the scattered intensity is measured in the focal plane of a lens of focal length f . A point on the screen, or photodiode array detector, at a certain distance from the optical axis corresponds to a scattering angle. In order to avoid the light scattered on the detector from the intense transmitted beam, a hole is drilled on it to let the transmitted beam pass through. Detectors used in such a configuration must often be custom-made to efficiently remove the transmitted beam. The Figure 1.4 (b) scheme, described by Ferri et al (2001)¹⁴ and Nishida et al (2008)¹⁵, is equivalent to the top one, with the difference of the sample being placed between the lens and the detector. The advantage is that large scattering angles may be attained simply by reducing the sample's distance from the lens, without changing f . Performing experimental SALS measurements is not so easy, because in the forward direction one must deal with the strong transmitted beam and with the unavoidable straylight. For this reason, more elaborate optical layouts became essential to deal with such difficulties.

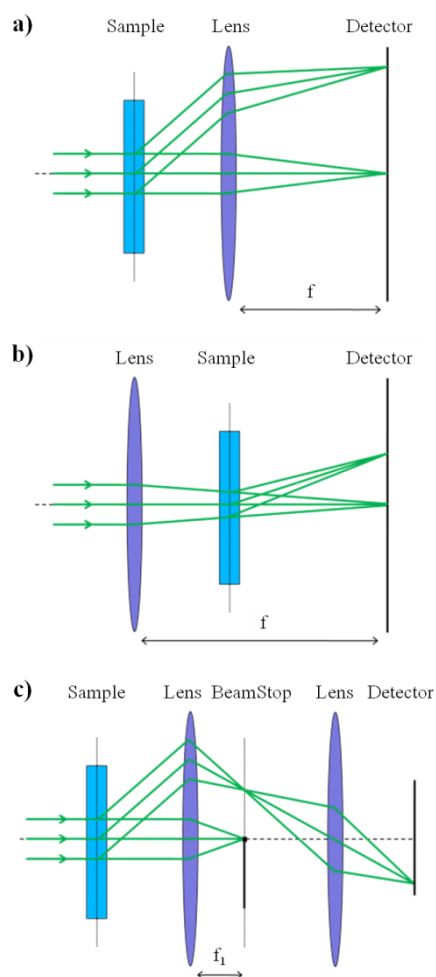


Fig. 1.4 SALS layouts

To overcome these difficulties, a CCD-based SALS apparatus, following the scheme of Figure. 1.4 (c), was proposed by Ferri (1997)⁹. The light emerging from the sample (transmitted and scattered light) is collected by a lens placed immediately after the sample. It is known from Fourier Optics¹⁶ that the far field intensity distribution of the light scattered from the sample appears in the focal plane of this lens together with the diffraction spot of the un-scattered beam. This latter is much more intense than the scattered light and must be blocked by using a beam stop accurately positioned on the focal plane. An image of this plane is then formed onto the CCD sensor which collects a 2D projection of the scattered intensity. The limitations imposed by straylight on SALS measurements can be attenuated by carefully subtracting a background signal, obtained by filling the experimental cell with the pure solvent.

Although typical SALS apparatuses usually cover up to 10 to 15 degrees, several setups have been presented using custom made cells and dedicated photodiode arrays and electronics to overcome this limit¹⁷. Recently, a CCD-based mid angle light scattering apparatus that covers the scattering angle range from 0.5 to 25 degrees, using only standard components that are readily available off the shelf, was presented⁷.

When SALS is combined with rheology, the relation of microscopic structure, dynamics and interparticle interactions with rheological properties of soft matter systems under shear can be probed. Various rheo-SALS setups¹⁸⁻²¹ have been used to study shear-induced orientation phenomena and structure changes in polymeric solids and fluids. For the study of structural changes on a micron scale, induced by shear flow, SALS is particularly useful because structural changes can be measured on line with rheological experiments (Fig. 1.5²²). The diversity of systems that can be studied makes the technique appealing for both research laboratories and industry. As a consequence, commercial Rheo-SALS instruments are available on the market, covering scattering angles up to 25 degrees²².

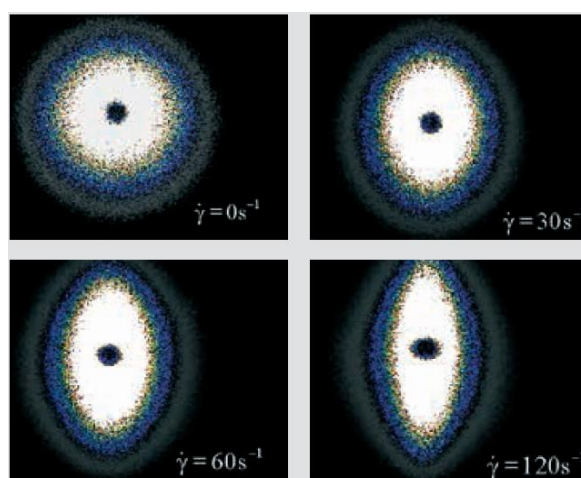


Fig. 1.5 Scattering pattern of a polymer blend at different shear rates, measured with a commercially available rheometer - combined SALS system (by Anton Paar²²) that covers scattering angles from 1° to 25°.

Objective

Exceeding the limit of 25 degrees of the currently existing commercially available Rheo-SALS instruments would give the opportunity to study even smaller length scales. Multi-functionality of the system, ease of use and modularity were some of the set goals. Thus, a high resolution CCD-based Small Angle Light Scattering (SALS) apparatus was designed and developed (Fig. 1.6), covering scattering angles from 2 to 30 degrees. It can be used for measurements on the bench with a cuvette and can be easily adapted as a modular accessory to commercially available rheometers, performing rheology-combined Static and Dynamic Light Scattering measurements (SLS, DLS). With the addition of an extra optical component, it performs Dark Field Microscopy (DFM) and Diffusing Wave Spectroscopy (DWS) measurements, providing the opportunity with a single instrument to probe a wide variety of samples (transparent and opaque) using different techniques. This combination of rheology with SLS, DLS, DFM or DWS through a single apparatus is not reported in bibliography, making this setup unique.

In the following chapters will be summarized the theory behind light scattering by particles, while a precise explanation of the developed SALS setup will be presented. Some possible applications of the SALS apparatus will also be provided, with measurements of dilute and concentrated colloidal suspensions.

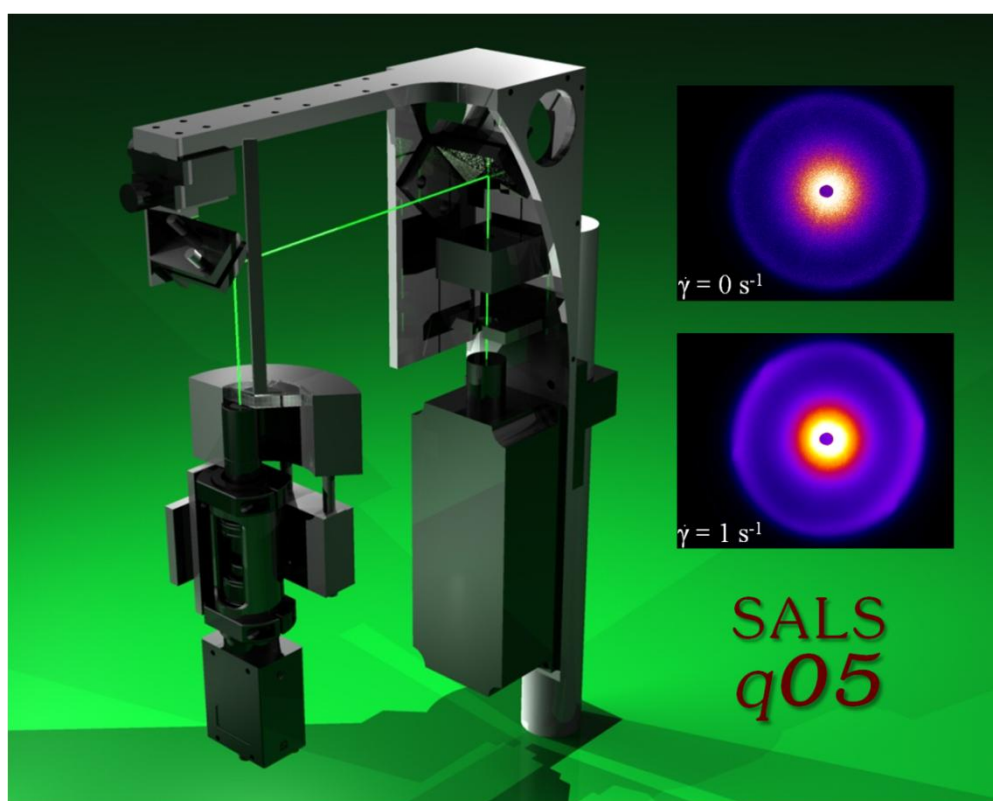


Fig. 1.6 Modular Rheo-SALS setup that was developed in this work. Insets show the scattering patterns of a concentrated colloidal suspension (PMMA spherical particles, with radius $R = 640$ nm, in squalene solvent, at volume fraction $\phi = 0.59$) at rest (top) and under oscillatory shear (bottom), measured with the SALS setup on a rheometer with parallel plate geometry (0.5 mm gap, 1000% shear strain).

CHAPTER 2

LIGHT SCATTERING THEORY

2.1 Definitions

Light is defined as the visible electromagnetic radiation, having a wavelength λ ranging from ~ 400 (violet) to ~ 750 nm (red) and a frequency f between 8×10^4 and 4×10^{14} Hz. It covers only an extremely narrow portion of the electromagnetic spectrum. The ratio of the velocity of light $c = f \cdot \lambda$ in vacuum (3×10^8 m/sec) to the velocity of light in a particular material v is called index of refraction n of the material.

$$n = \frac{c}{v} \quad (2.1)$$

Being precise, n is the real part of the complex refractive index m , describing absorbing materials, that have non-negligible electrical conductivity.

$$m = n + i\kappa \quad (2.2)$$

The imaginary part of the index of refraction κ , is related to the absorption in the material. For non-absorbing materials it equals to zero. The absorption coefficient A of a material is related to the complex part of the index of refraction with the following relation:

$$A = \frac{4\pi\kappa}{\lambda} \quad (2.3)$$

Moreover, for particles surrounded by a medium, the relative index of refraction m_r is used, which is defined as the ratio of the velocity of light in the ambient medium v_m to the velocity in a the particle v_p .

$$m_r = \frac{v_m}{v_p} = \frac{m_p}{m_m} \quad (2.4)$$

The refractive index of air is considered equal to 1, however, particles suspended in liquids have a **relative index of refraction** that defines the contrast between them, which affects their scattering efficiency as will be seen later on.

Scattering of light is governed by the ratio of the particle size to the wavelength of the radiation in the medium $\lambda = \lambda_o/n_m$, with λ_o being the vacuum wavelength. Therefore, this ratio which is called (dimensionless) **size parameter x** is given by:

$$x = k \cdot R = \frac{2\pi m R}{\lambda}, \quad (2.5)$$

where $k = 2\pi/\lambda$ is the wavenumber, m the index of refraction for the ambient medium and R the particle radius^{23,24}.

2.2 Light Scattering by Particles

When light passes through a transparent medium (other than a perfect vacuum), its oscillating electric field induces synchronous oscillating dipoles in the molecules of the medium, which re-emit the radiation. As long as the medium is homogenous, this effect is self-canceling, and the light is simply refracted. However, if the medium contains discrete variations in refractive index, as caused by the presence of particles, the re-emission from these inhomogeneities is detectable as scattering in all directions²⁴. In this context we assume that particles are spherical and non-absorbing, having imaginary part of refractive index equal to zero, and elastic light scattering occurs, meaning that light scattered by a particle is emitted at the identical frequency of the incident light.

The scattering intensity I_θ measured at a given angle θ and distance from the scattering center is sensitive in general to the particle size, shape and refractive index as well as the wavelength of light. This direct dependence on the particle's size, with small (compared to the wavelength of light used) particles scattering at high angles and larger ones scattering mostly at the forward direction (Fig. 2.1), makes light scattering information invaluable for particle sizing.

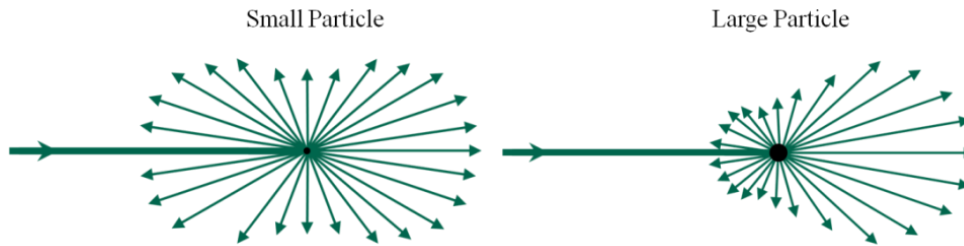


Fig. 2.1 Scattering of light by a small (left) and a large (right), compared to the wavelength of illumination, spherical particle.

There are several light scattering theories to describe the scattering patterns of particles in literature. The most known theoretical frameworks are the Rayleigh, the Rayleigh-Gans-Debye and the Mie theory. All theories are based on the Maxwell equations and model the scattering of a plane monochromatic optical wave by a single particle. Rayleigh theory is applicable only to particles that are much smaller than the optical wavelength, Rayleigh-Gans-Debye theory for particles with small relative particle to medium refractive indices, whereas Mie theory is valid for homogenous isotropic spheres of any size.

2.3 Rayleigh Theory

The classical light scattering theory, also called Rayleigh theory, was derived by Lord Rayleigh and applies only to small non-absorbing particles. It mainly assumes that the element scattering the light is sufficiently small relative to the wavelength of light so that the element can be approximated as a dipole located at a discrete point in space. The elements are also assumed to be sufficiently well separated so that the light striking them is the incident field and multiple scattering is negligible.

The scattered intensity as a function of scattering angle from an infinitely small particle, known as Rayleigh scattering I_θ , for un-polarized illumination of wavelength λ and intensity I_o , is given by^{23,24}:

$$I_R(\theta) = I_o \frac{8\pi^4 a^6}{r^2 \lambda^4} \left[\frac{m^2 - 1}{m^2 + 2} \right]^2 (1 + \cos^2 \theta), \quad (2.6)$$

where m is the refractive index of the particle relative to that of the medium, a the molecular polarizability being proportional to the particle's size, r the distance to the particle and θ the scattering angle. Thus, for particles smaller than $\sim \lambda/20$, the distribution of the detected scattered intensity over scattering angle is independent of the particles' size, which only affects the overall scattered intensity.

For particles larger than ~ 20 nm, several oscillating dipoles are created simultaneously within one given particle. As a consequence, some of the emitted light waves possess a significant phase difference. Accordingly, interference of the scattered light emitted from such an individual particle, leads to a nonisotropic angular dependence of the scattered light intensity, described by the Rayleigh-Gans-Debye scattering theory^{5,23-25}.

2.4 Rayleigh - Gans - Debye (RGD) Theory

Rayleigh generalized his analysis to particles of arbitrary size and shape, provided the difference of refractive index between the particle and medium was not too large. Further contributions were later made by Gans and Debye, and the theory is now termed Rayleigh-Gans-Debye (RGD) scattering. The general criterion for the validity of the RGD approximation is^{24,26,27}

$$\frac{2\pi d}{\lambda} |m - 1| \ll 1, \quad (2.7)$$

where d is the largest linear dimension of the particle and m the relative refractive index.

The particle is thought of as subdivided into small volume elements, each of which is considered as a Rayleigh scatterer (Fig. 2.3). The contributions of each element can be summed to give the net scattering intensity at any point of observation. The closeness of the refractive indices permits this summing because there is then little distinction between light travelling through the particle or the medium, since the total phase shift of the incident light wave is negligible. It is

evident that there will be mutual interference between the scattered rays emerging from the different volume elements^{24,26,27}. The net result is a reduction of the scattered intensity that may be expressed as:

$$I_{RGD}(\theta) = I_R(\theta) \cdot P(\theta), \quad (2.8)$$

where $P(\theta) \leq 1$, known as the “form factor”, describes the decrease of the scattered light intensity with increasing angle of observation, due to intramolecular interference of light beams scattered by different points of the same particle. Thus, $P(\theta)$ represents the modification of the intensity due to the finite size of the particles and to their deviation from sphericity²⁴. Depending on the size and shape of the particles, the form factor contains information for their form.

When it comes to the description of the inner workings of light scattering it turns out that the scattering angle θ is an inconvenient quantity to work with. Instead one uses a less intuitive quantity, the scattering vector q . Its definition is based on the wavevector k , which is a vector pointing in the direction of propagation of the light (the electromagnetic wave). When a light wave, with the wavevector k_{in} , impinges on a particle and emerges with a different direction (scattered), its wavevector changes accordingly into k_{out} (Fig. 2.2). The change in the wavevector is called the scattering wave vector q .

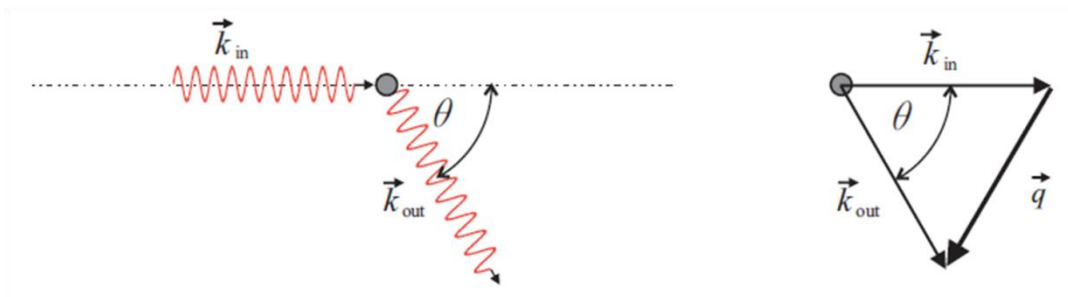


Fig. 2.2 Geometry of the scattering wave vector q .

The magnitude of $q = k_{out} - k_{in}$ is calculated by

$$q = \frac{4\pi}{\lambda} \sin \frac{\theta}{2}, \quad (2.9)$$

where θ is the scattering angle and λ the wavelength of the light in the medium surrounding the particle⁵.

A general expression of the form factor $P(q)$ as a function of the scattering vector is^{5,28}:

$$P(q) = \frac{1}{N^2} \sum_i \sum_j \exp[-i\vec{q}(\vec{r}_i - \vec{r}_j)], \quad (2.10)$$

in which the scattering object has been subdivided into N differential elements with r_{ij} being the separation distance between the i^{th} and j^{th} elements, as described in Figure 2.3.

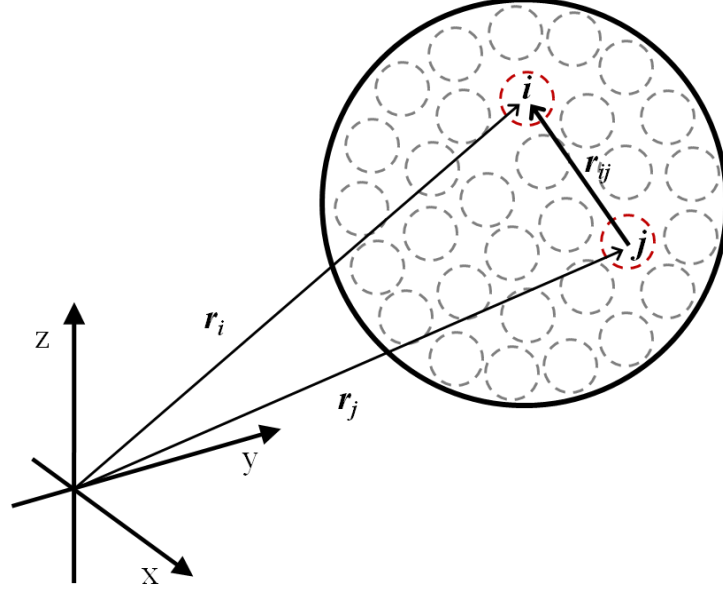


Fig. 2.3 A scattering object subdivided into N differential elements, each of which is considered as a Rayleigh scatterer. The separation distance between the i^{th} and j^{th} elements is r_{ij} .

$P(q)$ has been worked out for spheres, random coils, rods and other shapes. The analytical result for spheres of radius R is:

$$P(q) = \left[\frac{3 [\sin(qR) - qR \cos(qR)]}{(qR)^3} \right]^2 \quad (2.11)$$

This expression corresponds to an oscillating function, as shown in Figure 2.4. The position of the first minimum is found at $q \cdot R = 4.49$, which can be used to easily determine the particle radius r . Note that the oscillations are not as well pronounced for scattering from polydisperse spherical particles. Due to polydispersity the scattering profile will be the result of the superposition of the scattered light by particles of slightly different size, resulting in smoother minima.

For hollow spheres of radius R with very thin shell the form factor is:

$$P(q) = \left[\frac{\sin(qR)}{qR} \right]^2 \quad (2.12)$$

While, for random coils with radius of gyration R_g is:

$$P(q) = \frac{2}{(qR_g)^4} \cdot (\exp(-(qR_g)^2) - 1 + (qR_g)^2) \quad (2.13)$$

Figure 2.4 shows the form factors for spheres, hollow spheres and random coils with the same radius of gyration, as well as the form factor for spheres with polydispersity $\sigma = 0.05$.

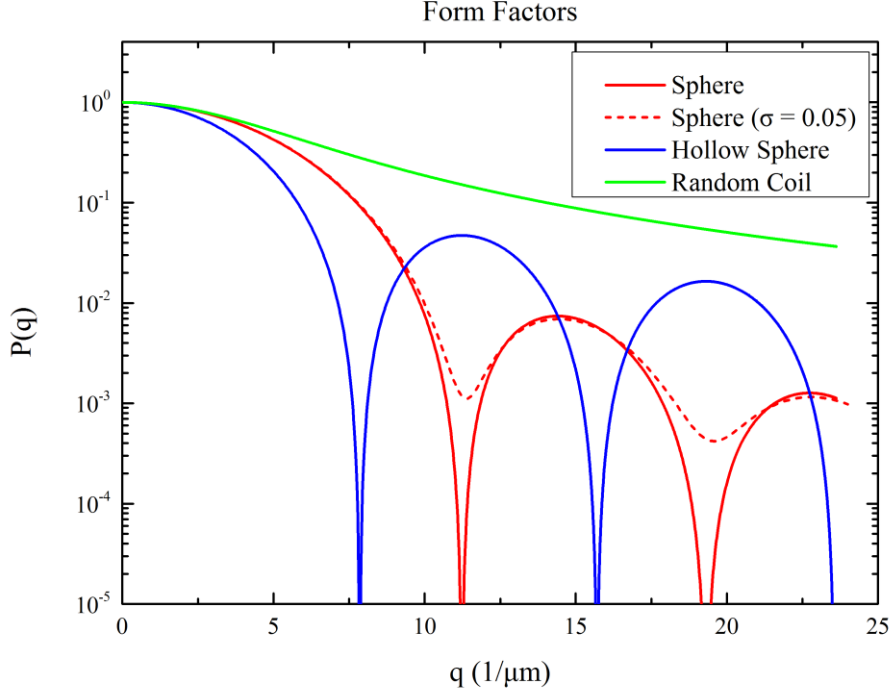


Fig. 2.4 Form factors for monodisperse spherical particles (red line), hollow spheres (blue line) and random coil (green line) and Spherical particles with polydispersity $\sigma = 0.05$ (red dashed line). All form factors correspond to the same radius of gyration. The sphere and hollow sphere radius is set at $R = 0.4 \mu\text{m}$ while the random coil radius is set at the value $R_g = \sqrt{3/5} \cdot 0.4 \mu\text{m}$. The whole q range corresponds to a vacuum wavelength $\lambda_0 = 532\text{nm}$ and a range of scattering angles from 0° to 180° .

An underlying assumption in the foregoing is that the dispersions under investigation are sufficiently dilute, that single scattering occurs, i.e., light scattered by any particle passes directly to the detector without being scattered by any other particles. As the particle volume fraction increases, particles come closer to each other and interference of scattered waves by different particles occur. On top of adding all point scatterers in one particle you need to add also those from different particles. So the double sum of equation 2.10 contains now terms referring to different particles. These may be accounted for in with the use of an additional factor, $S(q)$, called the structure factor²⁹.

$$I_{RGD}(q) = I_R(q) \cdot P(q) \cdot S(q), \quad (2.14)$$

It is evident that the structure factor depends on the structure of the dispersion. Experimentally the structure factor of a monodisperse system can be determined by measuring the scattered intensity of a dilute suspension $I_D(q)$, for which $S(q) = 1$ and the scattering intensity of the concentrated suspension $I_C(q)$. An experimental estimate of the structure factor would be calculated by:

$$S(q) = \frac{C_D}{C_C} \cdot \frac{I_C(q)}{I_D(q)}, \quad (2.15)$$

where C_D and C_C the concentration of the dilute and the concentrated suspension respectively.

When a particle becomes comparable in size or larger than the wavelength, several complications arise. If the index of refraction of the particle is different from its surroundings, refraction can occur at the interface that will contribute an angular dependence to the scattered light. This is referred to as anomalous diffraction. In addition, the total scattered field will be a superposition of light scattered from elements internal to the particle. When these individual contributions are summed, phase differences must be considered and will affect the result in two ways: (a) the incident light striking any element may be changed in phase due to a previous scattering interaction by another element, and (b) there will be phase interference (constructive and destructive) when individual contributions are added to calculate the total field^{4,23,24}. The more complex Mie theory accounts for all these.

2.5 Mie Theory

For particles outside the RGD range, a general theory is required, involving the full solution of the Maxwell equations. There is no distinct boundary between the so-called Mie and Rayleigh scatterers. Mie theory includes Rayleigh theory, which is a limiting theory strictly applicable only as the size of the particle shrinks to zero. Mie scattering theory has no size limitations and converges to the limit of geometric optics for large particles, though it assumes spherical, homogeneous, isotropic and non-magnetic particles in a non-absorbing medium. Understanding of Mie theory is not an easy task and the derivation of the equations is somewhat elaborate^{23,24}.

By comparing the measured scattering pattern (having known wavelength and medium refractive index) to the predicted from Mie theory, it is possible to obtain both the particle size and refractive index. The complex computation of the scattering patterns is usually done with the use of computer based algorithms. MiePlot software³⁰ is one of them, while during this project homemade software was developed, based on a previously published Matlab code³¹ for Mie scattering.

To better visualize the scattering pattern from a particle, according to Mie and RGD theory as well as their differences, some computations using MiePlot software will be presented. The wavelength of illumination used is 532 nm, while the medium refractive index is 1.42 for all computations. Three different particle sizes (radius $R = 0.2 \mu\text{m}$, $0.4 \mu\text{m}$ and $1 \mu\text{m}$) and refractive indices (1.42001, 1.49 and 1.6) were chosen.

Figure 2.5 shows both theory calculations for spherical particles with refractive index equal to 1.42001 suspended in medium with refractive index equal to 1.42. The relative refractive index m satisfies the RGD theory criterion and as seen, the respective size curves are identical. Changing the radius of the particles, changes the scattering profile observed. The first minimum (and the whole profile) is shifting to the left (smaller scattering angles) as the particles' size increases.

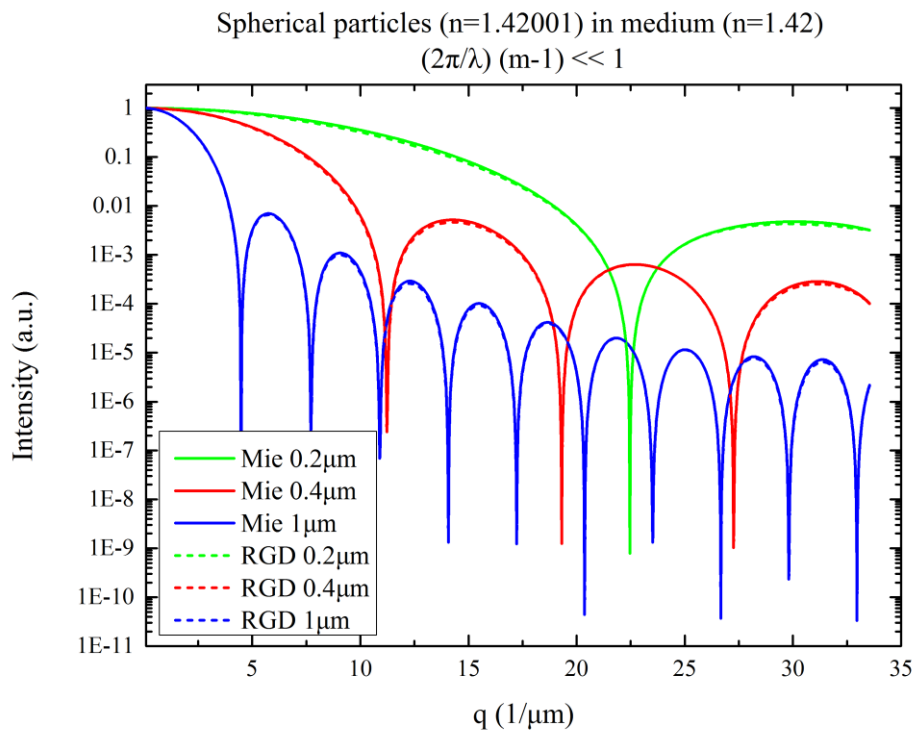


Fig. 2.5 Scattered intensity as a function of scattering vector q of spherical particles with a radius of $0.2 \mu\text{m}$ (green), $0.4 \mu\text{m}$ (red) and $1 \mu\text{m}$ (blue). Particles having refractive index 1.42001 are suspended in a medium with refractive index 1.42, creating a very small difference in the refractive indices. Calculations are according to Mie (solid lines) and RGD (dashed lines) theory.

The same calculations, using a particles' refractive index equal to 1.49 are presented in Figure 2.6. Now, the relative refractive index induces a greater contrast than before. The RGD criterion is not fulfilled and the calculations from the Mie and RGD theories start to deviate. It is notable that the difference in the refractive indices appears to be small (0.07) nevertheless discrepancies at scattering vectors above $\sim 10 \mu\text{m}^{-1}$ imply that a better index matching is required. Furthermore, even if the RGD

criterion is not satisfied, the scattered intensities at scattering vectors below $\sim 7 \mu\text{m}^{-1}$ (which is the experimental window of the SALS apparatus that was developed), calculated from the two theories are relatively similar. Another point to be additionally noted is that although the current calculations are without polydispersity, the minima of the scattering profiles according to Mie theory are shallower. This is quite important, since the effect of particles' polydispersity is exactly the same in RGD theory.

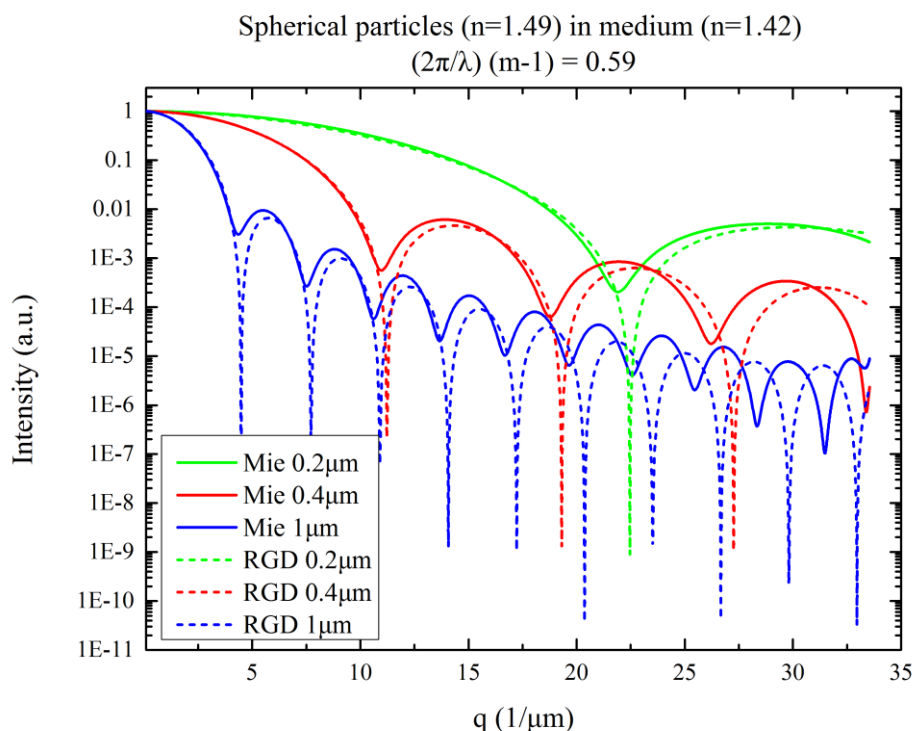


Fig. 2.6 Scattered intensity as a function of scattering vector q of spherical particles with a radius of $0.2 \mu\text{m}$ (green), $0.4 \mu\text{m}$ (red) and $1 \mu\text{m}$ (blue). Particles having refractive index 1.49 are suspended in a medium with refractive index 1.42 , creating a small but not negligible difference in the refractive indices. Calculations are according to Mie (solid lines) and RGD (dashed lines) theory.

When the contrast of the particles' - medium refractive indices becomes bigger, as calculated for particles' refractive index equal to 1.6 , the two theories start to deviate significantly as seen in Figure 2.7. This time, discrepancies appear at low scattering angles as well as for small particles. The first minima acquired from the different theories are not placed at the same q values. For RGD theory the minima are displaced to higher q values. Thus, if RGD theory is used outside its validity, it is leading to wrong estimation of the particles' size. Often the size of the particle is determined from the position of the first minimum according to $q \cdot R = 4.49$ for spherical particles. Here for example that would give the following radii $R_{(0.2\mu\text{m})} = 0.21 \mu\text{m}$, $R_{(0.4\mu\text{m})} = 0.42 \mu\text{m}$ and $R_{(1\mu\text{m})} = 1.2 \mu\text{m}$, which are off by 5% , 5% and 20% respectively.

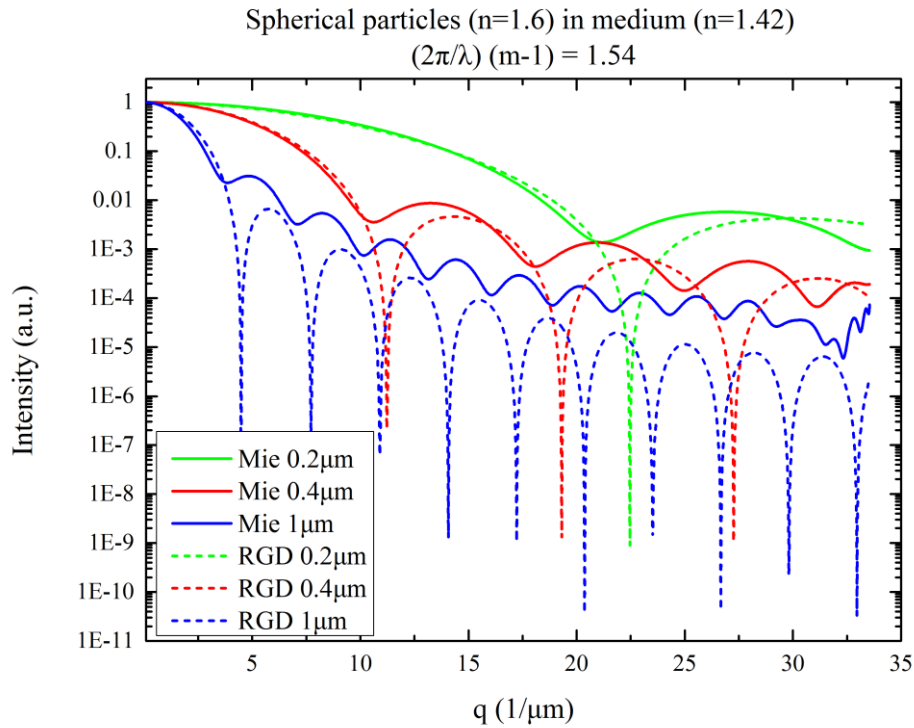


Fig. 2.7 Scattered intensity as a function of scattering vector q of spherical particles with a radius of 0.2 μm (green), 0.4 μm (red) and 1 μm (blue). Particles having refractive index 1.6 are suspended in a medium with refractive index 1.42, creating a significant difference in the refractive indices. Calculations are according to Mie (solid lines) and RGD (dashed lines) theory.

Concluding this short theoretical overview on the theory of light scattering from particles, it must be noted that data acquired through a small angle light scattering setup, should be analyzed according to this theory. This is due to the experimental window of possible scattering angles that is limited to the forward direction and mainly refers to particles with size comparable or higher than the wavelength of light. Rayleigh-Gans-Debye theory can be used as well, if the relative refractive index of the particles to the medium approaches 1.

CHAPTER 3

DEVELOPMENT

In this chapter we present the whole procedure, from idea to realization, for the development and optimization of a compact, high resolution, small angle light scattering (SALS) setup, that can be used for rheological applications.

3.1 Aim – Limitations

The basic goal of the current project was to create a compact device, that will fit under a rheometer and perform small angle light scattering measurements reliably, without compromising resolution and performance. Thus, for the process to begin, as in every development procedure, all limitations introduced by equipment to be used and various performance goals were defined.

Rheometer

The target rheometer, on which the SALS apparatus was going to fit, was an *Anton Paar MCR-501* (Fig. 3.1). The main spatial limitation introduced, was the bottom plate of the rheometer, which must be noted that is the same for several Anton Paar rheometers, making the setup usable for other Anton Paar models as well.

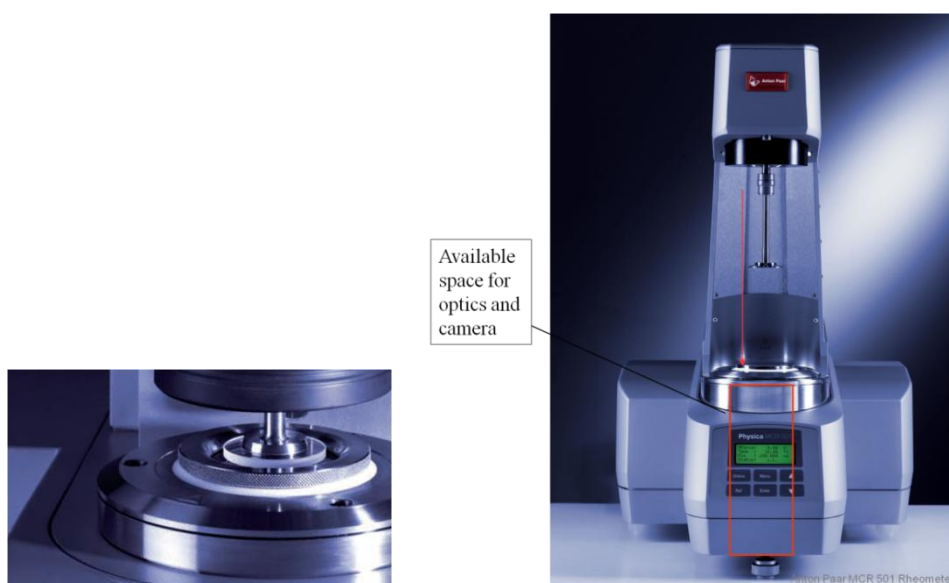


Fig. 3.1 Anton Paar MCR-501, showing available space for acquisition part of SALS to be developed.

All dimensions of interest of the bottom and top plates were physically measured, with a micrometer, and 3D drawn in CAD design software, for easier calculation of the limitations they introduced (Fig. 3.2).

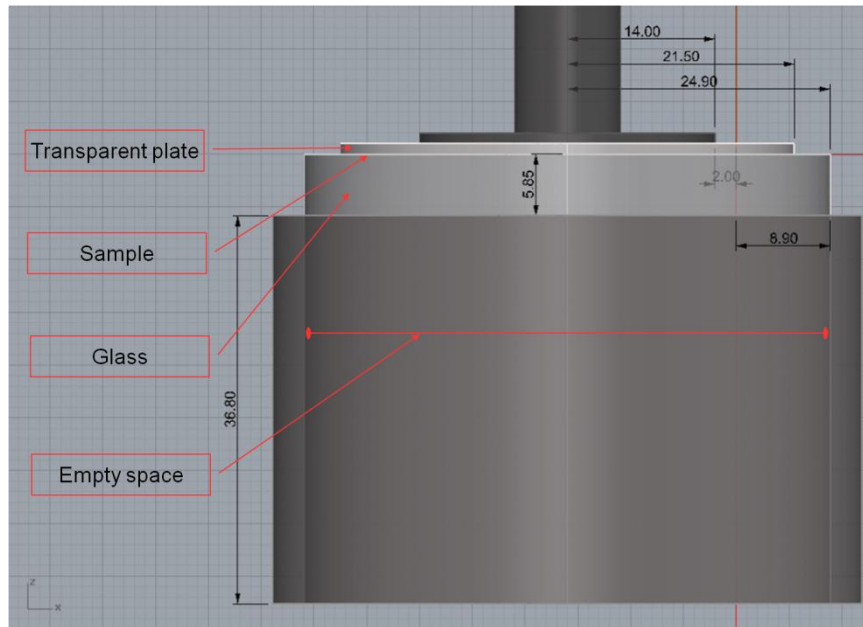


Fig. 3.2 2D drawing of rheometer's limiting dimensions. (Dimensions in mm)

First of all, the glass of the bottom plate, on which the sample is loaded, is 5.85 mm thick, affecting the minimum sample to system distance. Secondly, the available empty space may be about 50 mm in diameter, but the top plate, having a non transparent metallic part holding the transparent plate, affects the position of the incoming beam that should pass through the sample and extend to the center of the system's optical axis. Consequently, for at least 36.8 mm the system should be no more than 8.9 mm in radius. Finally, the height available from bottom plate's glass bottom to the optical table is 220 mm; therefore this is the maximum total length of the system, including the physical dimension of the camera.

Camera

The camera that was to be used for the detection part of the system, was a *Point Grey Grasshopper 14S3*. This specific camera was chosen for its wide dynamic range, extracting 16-bit raw images produced from a 14-bit analog-to-digital converter. It uses a *Sony ICX267* 1/2" progressive scan CCD sensor with 1384x1032 resolution and 4.65x4.65 μm pixel size, resulting in a sensor size of 6.435x4.798 mm. The sensor to back end of the camera distance is 55 mm, which reduces the maximum effective total length of the system to 165 mm.



Fig. 3.3 *Point Grey Grasshopper 14S3* camera.

Laser

For the illumination part of the system, a *Roithner MSL-FN-532-20mW* laser system was used. This is a CW green diode pumped solid state laser, working at single longitudinal mode, producing 20 mW output power. Basic specifications of the laser are presented in Table 3.1.

Wavelength	532 nm
Output Power	20 mW
Transverse Mode	TEM ₀₀
Power Stability	< 1%
M ² Factor	< 1.2
Beam Divergence	< 1.5 mrad
Beam Diameter	~2 mm
Polarization	> 100:1

Table 3.1 Basic specifications of *Roithner MSL-FN-532-20mW* laser system.

The minimum specification of the laser for the SALS setup comprise power stability being less than 5%, TEM₀₀ beam profile with diameter less than 3 mm and small divergence (< 2 mrad). Since the beam characteristics of this laser were acceptable for the setup, no additional collimation or beam manipulation was necessary. A *Bernhard Halle* Glan-Thompson polarizer (extinction ration better than 10⁻⁶) was used, to adjust the incident beam polarization, an *Edmund Optics* neutral density filter (optical density $OD = 3$), to reduce beam power and two dielectric mirrors mounted on kinematic mirror mounts to direct it, as will be described later in the text.

Optical Components

The main optical components of the acquisition system are lenses. Although the use of custom made lenses broadens optical design options and capabilities, commercially available lenses were used, in order to keep the cost of the system within reasonable limits. The maximum diameter available for the system, limited by the reometer, was calculated to be 8,9 mm. Taking the required mechanical support of the lenses into consideration and the fact that a great variety of lenses come into half inch diameter (for small focal lengths), the lenses to be used for the setup were “limited” to 0.5” diameter. The maximum possible size was used, in order to have the maximum possible numerical aperture, for the system to collect the required angular field, as will be described. All lenses have an anti reflection coating at the visible spectrum, since reflections could affect significantly small angle light scattering measurements.

Conclusion – System Specifications

Summing up all equipment introduced limitations (Table 3.2), and combining them with system requirements, some valuable information were extracted for the development to commence.

Wavelength (λ)	532 nm
Beam Diameter ($2w_0$)	2 mm
Optics Diameter (D)	12.7 mm
Effective Total Length (L)	165 mm
Minimum sample to 1st lens Distance (S1)	6 mm
CCD sensor size	6.435x4.798 mm

Table 3.2 Equipment introduced limitations for the system to be developed.

The main requirement of the system was to collect an angular field (θ) of 30 degrees. In Figure 3.4 we show the dependence of the acquired angular field, from an optical system's distance to a scattering sample. The closer the optical system goes to the sample, the greater scattering angles (θ) it can collect.

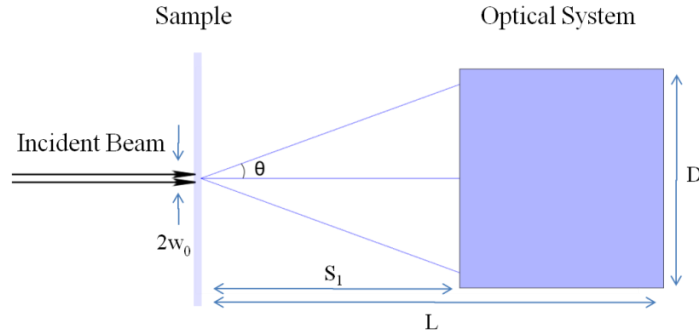


Fig. 3.4 Drawing of the relative position of a black box optical system to a scattering sample. The acquired angular field depends on the sample to system distance (S_1).

Using simple geometry and taking the waist width ($2w_0$) of the incident beam into consideration, the maximum sample to first lens distance can be calculated, after equation 3.1.

$$S_1^{max} = \frac{\frac{D}{2} - w_0}{\tan \theta_{max}} \approx 9.2 \text{ mm} \quad (3.1)$$

Consequently, for the first lens to be able to handle the incoming rays, its maximum focal length should be no more than about 9mm. It must be noted that the use of a microscope objective was excluded, since the minimum distance from the sample was too big.

3.2 Optical Design

In order to have a detailed performance overview of the system under development, all calculations and simulations were performed in optical design software (2009 release of *Zemax Radiant*). *Zemax* offered the opportunity to optimize the system according to requested requirements, eliminate aberrations and extract various diagnostic graphs³² (Fig. 3.5), becoming an invaluable tool for the optical design process which was mainly guided by optics handbooks^{16,33–37}. Commercially available lenses were imported from a lens catalog, featuring *Zemax*, containing various manufacturers. This way, different layouts, using different lenses at different positions, were tested and finally, an optimized system layout was produced.

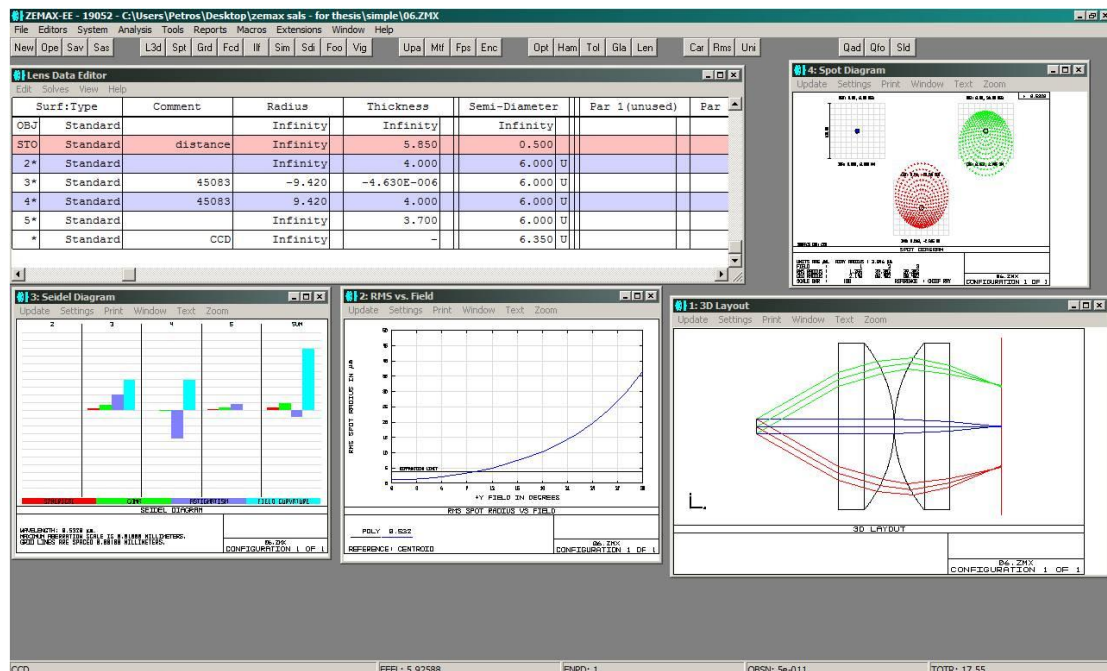


Fig. 3.5 Screenshot of Zemax optical design software interface.

3.2.1 Optimization

According to basic laws of propagation of light, when parallel rays intersect a converging lens, they focus in one single spot at a distance equal to its focal length. This way a converging lens images the far field intensity distribution of the light scattered from a sample on its back focal plane. This back focal plane is known as the Fourier transform plane, where the spatial image is transformed into a spatial frequency spectrum. This is a remarkable and useful property of a converging lens, known in such a configuration as “Fourier lens”, having the ability to perform two-dimensional Fourier transforms¹⁶. Figure 3.6 simulates a Ray tracing of parallel rays for different angles (0° blue, 30° green, -30° red) after passing through a thin lens. The lens is positioned at one focal length (f) distance from the input plane (being the scattering sample) and the output plane (being the sensor) of the system.

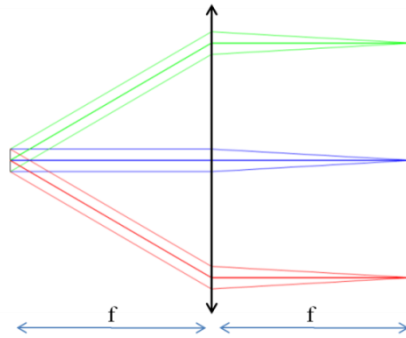


Fig. 3.6 Ray tracing for different angles (0° blue, 30° green, -30° red) after passing through a thin lens, simulated in *Zemax*. The lens is positioned at one focal length (f) distance from the input plane (scattering sample) and the output plane (sensor) of the system.

Optimization Example

An optimization example will be presented, for the reader to understand that optical design of an optical system is a complex, time-consuming process, having the main goal to eliminate aberrations that are introduced from the optical elements, while meeting the set system's purpose. Each type of lens, introduces different amounts of different aberrations, depending on how and where it is placed. Combinations of lenses, introducing positive and negative respective aberrations, are usually used in order to manipulate those aberrations. Of course, this procedure cannot carry on forever. For this reason, there is a point when some set of requirements are met, although certain amounts of aberrations may remain. Optical design procedure should be considered as an ongoing.

Lenses do not really form perfect images. This imperfection is due to aberrations (deviation from perfect imaging) introduced by the optical elements. Standard monochromatic aberrations are the spherical aberration, astigmatism, coma and field curvature. These are related to the object's relative position to the optical axis. Spherical aberration causes incident rays, from a point source on the optical axis, that reach the center and the periphery of the lens to be focused at different locations. If the point source is off-axis, then rays passing through the center and periphery of the lens are focused at different locations, creating a comet like tail after which coma aberration is named. Astigmatism, like coma, is an off-axis aberration. Rays from an object point passing through the horizontal and vertical diameters of a lens are focused as a short streak at two different focal planes, resulting in different focusing in the horizontal and vertical axis. Finally, due to field curvature, rays coming from points of an extended object that are off axis focus before rays from points near the optical axis, resulting in a curved image^{34,38}. Aberrations depend not only on the lens' power, thus the radii of its surface curvatures and its diameter, but on their position also. The main purpose of the optical design process is to eliminate these aberrations by properly modifying the surface curvature and positioning for each lens in a way to generate a layout that meets the system requirements with the least amounts of aberrations.

The various steps involved in the process of using optical raytracing software like *Zemax* in the optimization of an optical system can be clearly shown through the design of a simple imaging system. An example on how positioning and combination of lenses can affect aberrations and finally image quality, on such a system, will be presented. All lenses used are commercially available plano-convex lenses of 12 mm effective focal length and 12.7 mm diameter. The scope of the system is to image parallel rays into spots with the smallest possible size. This procedure is called optimization. The angular field used is up to 30° . System evaluation was performed through various analysis diagrams, generated in *Zemax*. A ray tracing diagram for different angles, a Spot diagram for the respective fields, an RMS Spot Radius versus angular field diagram and a Seidel aberration analysis diagram.

In the first system, presented in Figure 3.7, a plano-convex lens is placed with the convex surface facing front. Parallel rays entering the lens at zero angle are focused perfectly to a circular spot of $0.5\mu\text{m}$ diameter. However, as the angular field increases, the spot size increases remarkably, reaching 250 microns of RMS spot radius at 30° . Through the Seidel aberration analysis diagram (Fig. 3.7 top right) one can see the types of aberrations introduced by each lens' surface and their final addition. This system exhibits a great amount of astigmatism and field curvature, some coma but no spherical aberration. Astigmatism is obvious in the Spot Diagram (Fig. 3.7 bottom left) for the $\pm 30^\circ$ angular field, which appear elongated in one direction, while field curvature is visualized easily in the Ray tracing diagram (Fig. 3.7 top left), where rays for the $\pm 30^\circ$ angular field focus before the paraxial image plane.

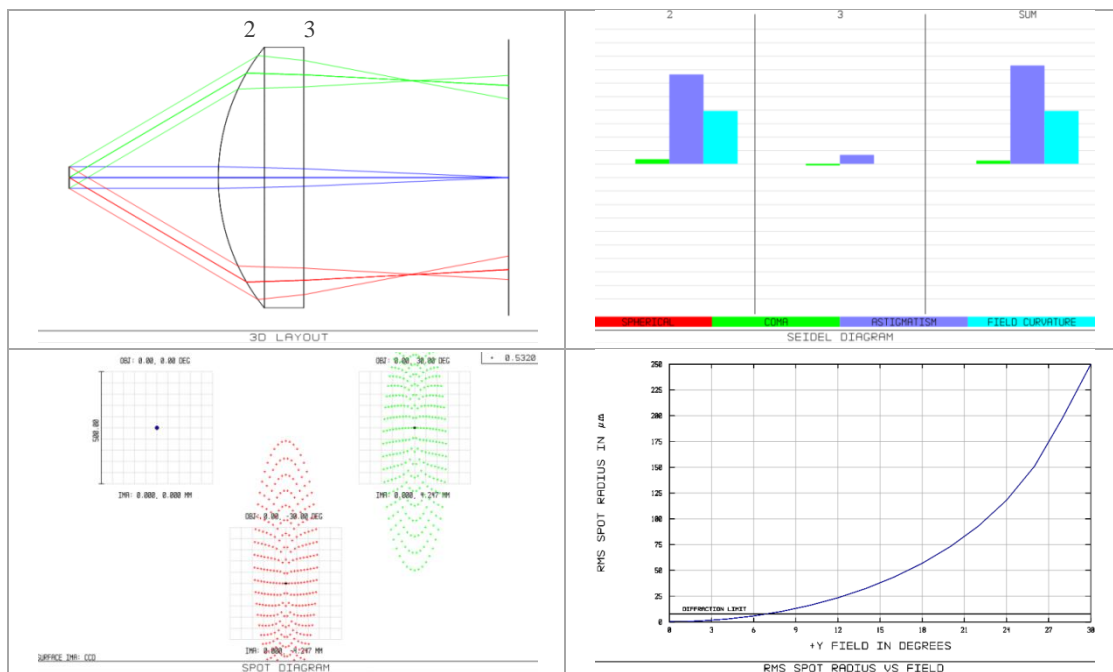


Fig. 3.7 Ray tracing (top left) for different angles (0° blue, 30° green, -30° red) after passing through a plano-convex lens, having the plano surface facing back, with effective focal length 12 mm and positioned such to acquire optimum focus at 0° field. Spot Diagram (bottom left) for respective fields with maximum scale $500\mu\text{m}$ and RMS Spot Radius versus angular field (bottom right) with maximum scale $250\mu\text{m}$. Seidel aberration analysis diagram (top right) shows main aberrations with maximum scale $10\mu\text{m}$, introduced from each lens' surface and finally summed. All diagrams simulated in *Zemax*.

A variation of the previous system is generated by inverting the lens. After inverting the lens, placing the plano surface facing front, optical performance changes (Fig. 3.8). Again, parallel rays inserting the lens at zero angle are focused perfectly while as the angular field increases, the RMS spot size increases. However, this time the RMS spot radius at 30° is 120 microns. Furthermore, by just inverting the lens the maximum RMS spot radius was reduced to half. An analysis of the aberrations through the Seidel aberration analysis diagram (Fig. 3.8 top right) shows that, field curvature remains the same, some spherical aberration appears in a small amount but interestingly astigmatism is reduced.

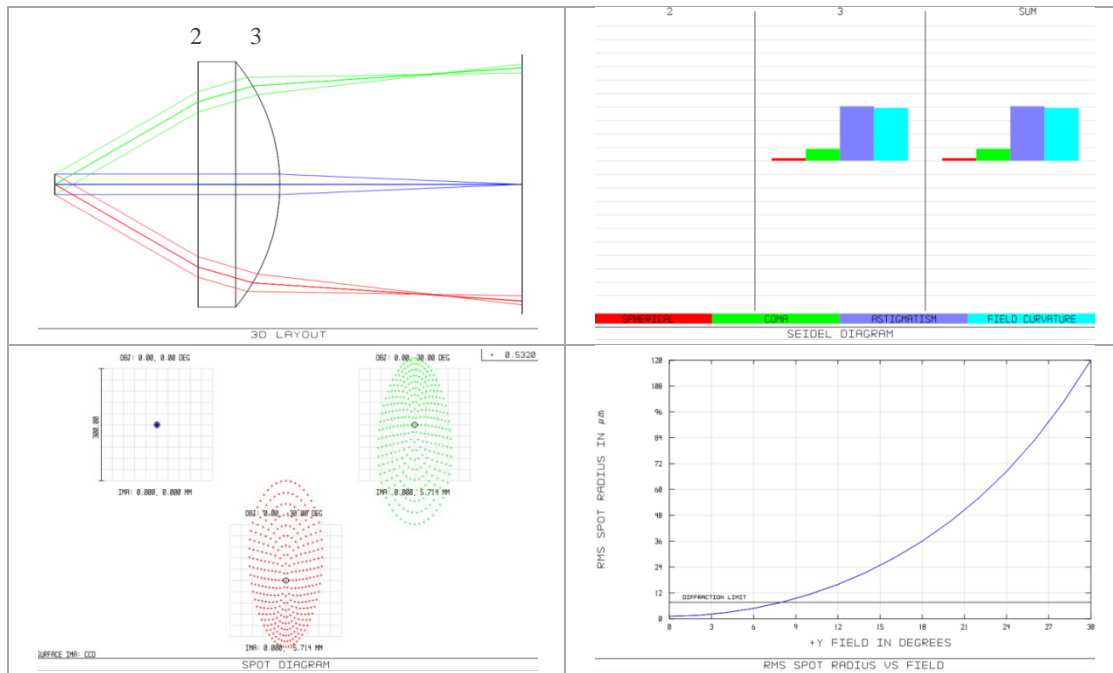


Fig. 3.8 Ray tracing (top left) for different angles (0° blue, 30° green, -30° red) after passing through a plano-convex lens, having the plano surface facing front, with effective focal length 12 mm and positioned such to acquire optimum focus at 0° field. Spot Diagram (bottom left) for respective fields with maximum scale 300 μm and RMS Spot Radius versus angular field (bottom right) with maximum scale 120 μm . Seidel aberration analysis diagram (top right) shows main aberrations with maximum scale 10 μm , introduced from each lens' surface and finally summed. All diagrams simulated in *Zemax*.

A further improvement of the optical performance can be achieved by the two previous systems, thus by placing one lens with its plano surface facing front followed by a second identical, but reversed, lens having its plano surface facing back. Now a lenslet of higher power is created (Fig. 3.9). This system collects the same angular field, imaging it at a smaller area. Parallel rays inserting the lens at zero angle are focused perfectly, while as the angular field increases, the RMS spot size increases like previously. However, this more complex system produces a maximum RMS spot radius of 75 microns (at 30°). Through the Seidel aberration analysis diagram (Fig. 3.9 top right), one can see that the second lens introduces negative astigmatism that cancels out positive astigmatism introduced by the first one. Finally all aberrations, except for field curvature, remain at small values. This system shows that by combining lenses, aberrations introduced by a lens, can be used in favor of the final system's performance.

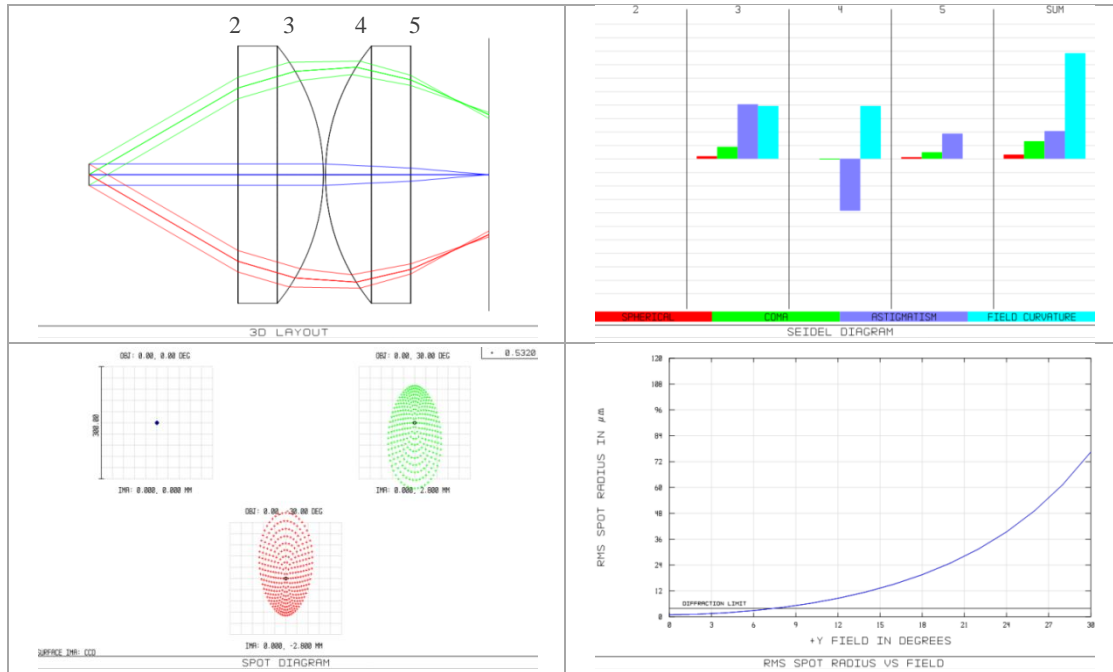


Fig. 3.9 Ray tracing (top left) for different angles (0° blue, 30° green, -30° red) after passing through a plano-convex lens, having the plano surface facing front followed by another one inverted and at 0.1 mm distance. Both lenses have effective focal length 12mm and are positioned such to acquire optimum focus at 0° field. Spot Diagram (bottom left) for respective fields with maximum scale 300 μm and RMS Spot Radius versus angular field (bottom right) with maximum scale 120 μm . Seidel aberration analysis diagram (top right) shows main aberrations with maximum scale 10 μm , introduced from each lens' surface and finally summed. All diagrams simulated in *Zemax*.

Zemax optical design software automatically optimizes a system by changing relative positions of elements in order to acquire the least RMS spot radius according to set goals. Figure 3.10 shows the system with the two plano-convex lenses after optimization. The changes made concerned the object - first lens distance (from 7 mm to 5.85 mm), the second lens - sensor distance (from 3.67 mm to 3.7 mm) and the distance between the two lenses (from 0.1 mm to 0 mm). This final system reached a maximum RMS spot radius at 30° of 36 microns. The only remaining significant aberration is field curvature, which is unavoidable when only converging lenses are used. To cancel out or reduce it, additional lenses, preferably diverging, should be used.

The RMS spot radius as a function of the angular field, for all four different systems described, is presented in Figure 3.11. There, the overall effect of the optical design procedure is visualized. The initial system had a maximum RMS spot radius exceeding 250 microns that was reduced down to 36 microns (a $7\times$ reduction) after the optimization. Of course, reducing spot size is not the only concern in an optical design. In this example the target was to reduce the spot size. For this purpose a combination of lenses was used, changing the system's power and final magnification. First priority is to meet the set of requirements with the least possible amounts of aberrations.

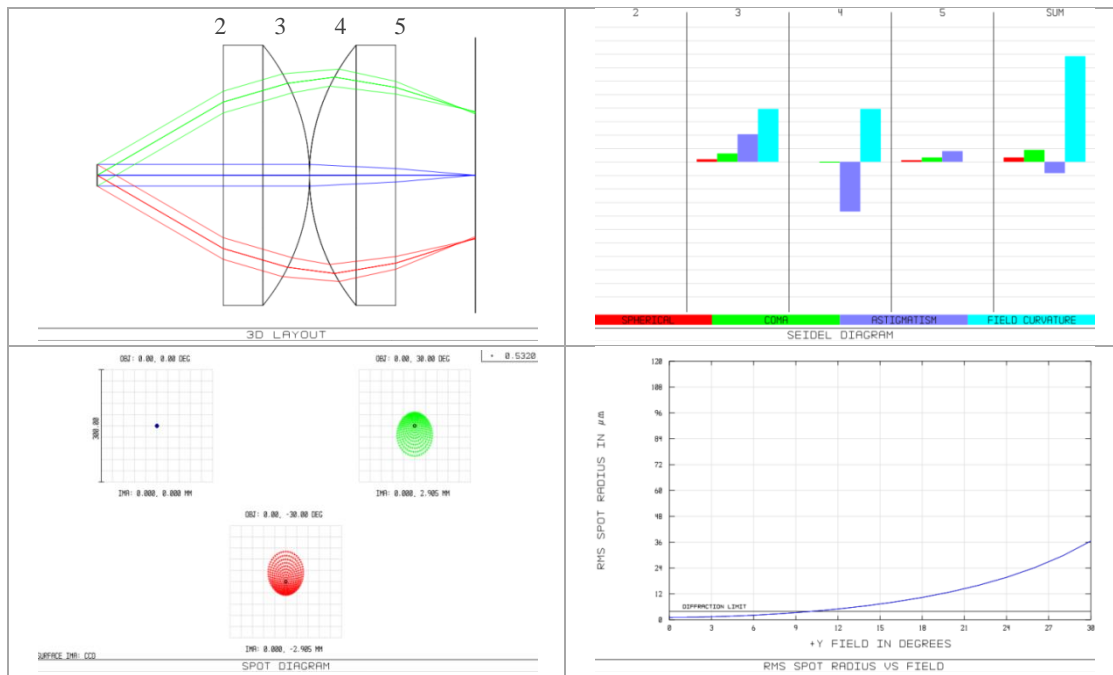


Fig. 3.10 Ray tracing (top left) for different angles (0° blue, 30° green, -30° red) after passing through a plano-convex lens, having the plano surface facing front followed by another one inverted. Both lenses have effective focal length 12 mm and their relative positions have been optimized to acquire the least RMS spot radius possible. Spot Diagram (bottom left) for respective fields with maximum scale 300 μm and RMS Spot Radius versus angular field (bottom right) with maximum scale 120 μm . Seidel aberration analysis diagram (top right) shows main aberrations with maximum scale 10 μm , introduced from each lens' surface and finally summed. All diagrams simulated in *Zemax*.

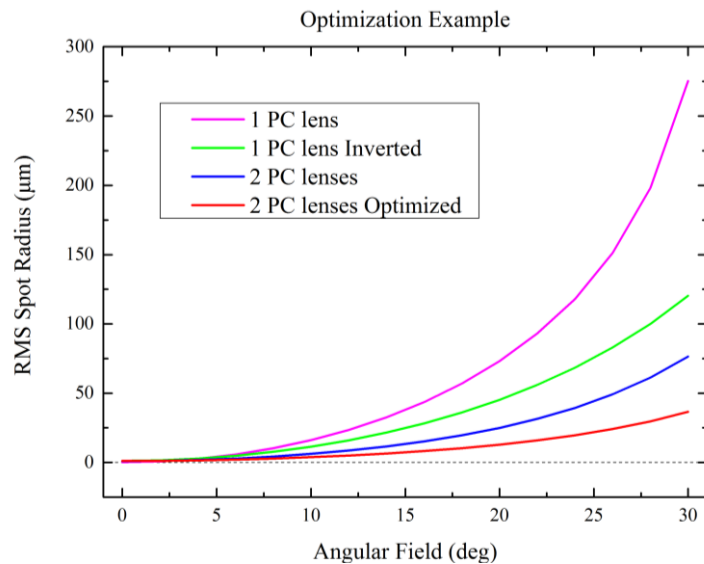


Fig. 3.11 Optimization example, showing the RMS Spot Radius as a function of Angular Field, for four different systems. One plano-convex lens with the convex surface facing front (magenta line), one plano-convex lens with the plano surface facing front (green line). two plano-convex lenses with the first having the plano surface facing front and the second having the plano surface facing back (blue line). Red line represents the system with the two plano-convex lenses after distances optimization. All lenses are identical with effective focal length 12 mm. Results were simulated in *Zemax*.

Following we present an initial design approach of the SALS system that was developed, using a very simple layout, as well as the final optimized optical system.

The Simple System

One of the most popular existing layouts for SALS is the one presented by Fabio Ferri in 1997⁹. In this layout (Fig. 3.12), a collimated laser beam passes through the sample and is focused on a beam stop. The light scattered from the sample is collected from the first lens L_1 and is directed to a second lens L_2 that is placed in the conjugate with the sample plane that finally focuses it on a CCD sensor, placed in a conjugate plane with the beam stop.

After including the limitations of the system to be developed, a similar optical system, to the system proposed by Ferri, was simulated in *Zemax*. At first thin ideal lenses were used to visualize and calculate the required lenses' focal lengths and relative positions. The optimized 2D ray-tracing simulation layout is presented in Figure 3.12. The angular field range covered by the system is from 1 to 30 degrees, with a total length of 166.8 mm.

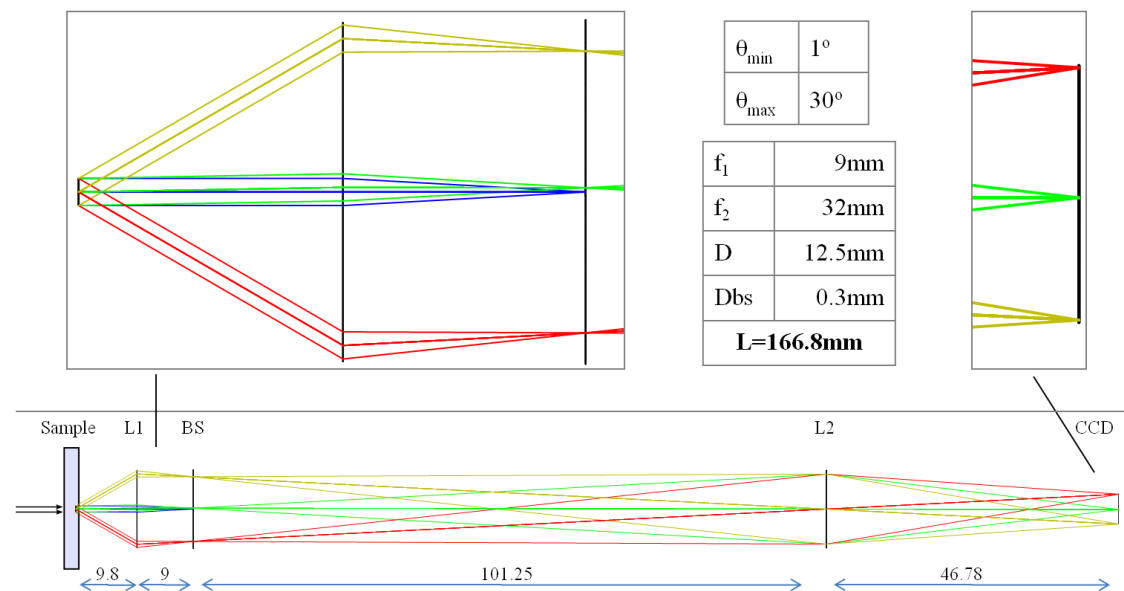


Fig. 3.12 2D ray-tracing simulation layout of Ferri's SALS approach, using thin lenses, simulated in *Zemax* (bottom). Zoomed regions of start (up left) and end (up right) of the system and information for it (up center). Blue rays stand for 0°, green for 1°, while red and yellow for 30° and -30° respectively. (Distances are expressed in mm)

From this simulation, the optical operation of a SALS apparatus becomes more apparent. All parallel rays outgoing from the sample plane (Fig. 3.12 up left) are finally focused on one single point on the sensor plane (Fig. 3.12 up right).

Thin lenses are usually initially used in the optical design procedure to visualize how a perfect system can be. This is because thin lenses are ideal and do not introduce aberrations as in the case of real thick lenses. After replacing thin ideal lenses with commercially available ones (a Plano-Convex and a Biconvex), aberrations appear, as seen in Figure 3.13.

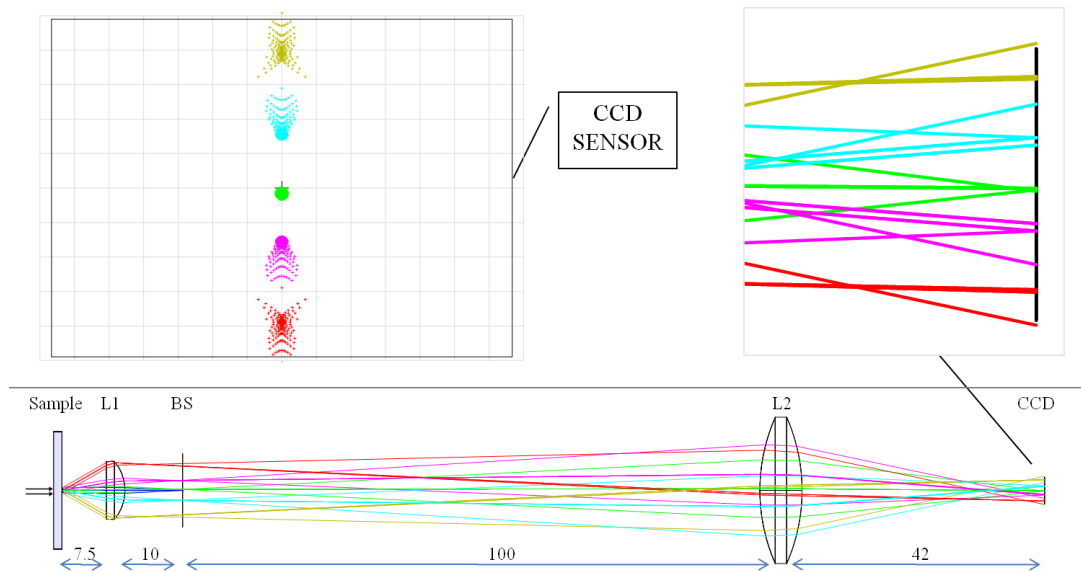


Fig. 3.13 2D ray-tracing simulation of Ferri's SALS approach, using commercially available single lenses, simulated in *Zemax* (bottom). Zoomed region of end of the system (up right) and footprint diagram of the sensor (up left). Blue rays stand for 0° , green for 1° , blue and violet for $\pm 10^\circ$, yellow and red for $\pm 30^\circ$. (Distances are expressed in mm)

Figure 3.14 shows the RMS spot radius as a function of the angular field (angle from optical axis), which reaches values over 360 microns. Considering the pixel physical size of the camera, being only $4.65 \mu\text{m}$, this kind of layout needs a lot of improvement, if used in a so small total length version and with single lenses. The results of this layout's simulation, reveals the need of a more complex system, using combinations of doublet lenses, to create lenses with small effective focal lengths (the overall focal length of the combined lenses) and minimize aberrations.

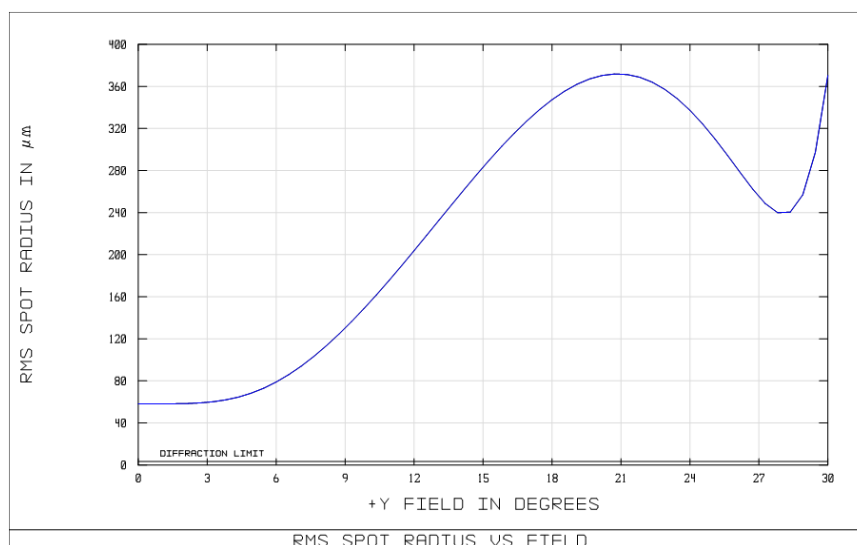


Fig. 3.14 RMS spot radius versus angular field covered by a simple two-lenses SALS setup, simulated in *Zemax*. Black line represents the theoretical diffraction limit (Rayleigh criterion).

Telecentric Approach

To create a small total length and diameter SALS apparatus, a layout consisted of a Fourier lens and an imaging part featuring telecentricity was adopted. Telecentricity occurs when the chief rays (rays from off-axis points in the object plane passing through the center of the aperture stop, being the physical element which limits the angle of acceptance of the imaging system) are parallel to the optical axis, in object and/or image space^{39,40}. When telecentricity is fulfilled in both object and image space, the system is termed double telecentric. Telecentricity was implemented in the system in order to achieve better focusing stability. In such systems, displacement of the camera or the object affects much less the acquired focus, since the chief rays are directed vertically to the sensor, providing nearly constant magnification over a range of working distances.

Figure 3.15 shows the *Zemax* ray tracing simulation of this layout, with the use of three thin lenses L_1 , L_2 and L_3 with focal lengths $f_1 = 8$ mm, $f_2 = 30$ mm and $f_3 = 15$ mm respectively. The lenses' diameters were set to half inch, while the CCD sensor matches in dimensions the one of the camera to be used.

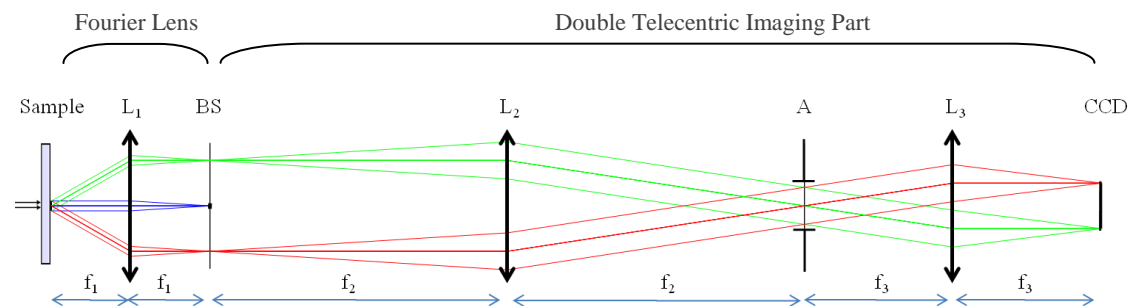


Fig. 3.15 2D layout of SALS telecentric approach, simulated in *Zemax*, with the use of thin lenses L_1 , L_2 and L_3 . BS is the beam stop plane and A is the aperture plane. Blue rays stand for 0° , while green and red for 30° and -30° respectively.

The first lens (L_1) acts as a Fourier lens, imaging in its back focal plane the far field intensity distribution of the light scattered from the sample. There a beam stop (BS) blocks the unscattered part of the beam. Then the double telecentric imaging part, formed by lenses L_2 and L_3 , which are confocal, with an aperture (A), placed on their common focal plane, images the BS plane on the CCD sensor. The aperture, is conjugate with the sample (the sample is imaged on the aperture plane) and acts as an aperture stop of the system, defining the cone angle of the bundle of rays that will pass through and finally be focused on the sensor. This way a sharper focus is achieved. In addition, rays scattered elsewhere (straylight), are prevented from reaching the sensor.

The adoption of this layout turned out to be crucial for the development of the compact SALS setup, since it enabled the approach of the optical design in a structured and systematic way. Following we describe the final optimized SALS layout.

3.2.2 Final Optimized Layout

After several trials and simulations, implemented in *Zemax*, using combinations of several commercially available lenses applied in the telecentric layout described above, we reached to a final system named SALSq05. An extension (named mode-2) of this setup was also developed. In this case, with the addition of optics, the system can image the sample surface, thus operating as an optical microscope.

SALSq05

A schematic of the final SALSq05 setup layout is presented in Figure 3.16. A collimated laser beam initially passes through a linear polarizer (P), needed to set the desired direction of polarization, and illuminates the sample placed below the top plate (TP) of the rheometer. A first lenset (L_1) is placed at a distance S_1 from the sample. This distance (S_1) stands for the effective focal length of L_1 , corrected for the refractive index of the bottom glass plate (BP). At the effective back focal plane (f_1) of L_1 , a beam stop (BS) is placed to remove the un-scattered beam. All parallel scattered light rays from the sample are focused on this plane.

Combined with L_1 , a second lenset (L_2), placed at a distance from the BS plane equal to its effective focal length (f_2), creates an inverted telescope that demagnifies the angle of the light rays scattered by the sample. L_2 , combined with a third lenset (L_3), forms a second inverted telescope. L_3 is placed at a distance from L_2 that equals to the sum of their effective focal lengths (f_3 and f_2 respectively), making them confocal, with an aperture (A) of varying diameter in their common focal plane. This way, a double telecentric imaging system is created, that sharply images the BS plane on the CCD sensor, with the appropriate magnification. The aperture plane is conjugate with the sample plane and acts as an aperture stop of the system. Such an aperture, defines the cone angle of the bundle of rays that pass through the whole optical system and finally focus on the sensor, determining brightness and preventing straylight from reaching it. A linear polarizer, acting as an analyzer, is placed between L_2 and L_3 . Finally each cone of light scattered at a certain angle from the sample, is mapped onto a ring, on the CCD sensor, centered to the optical axis of the system.

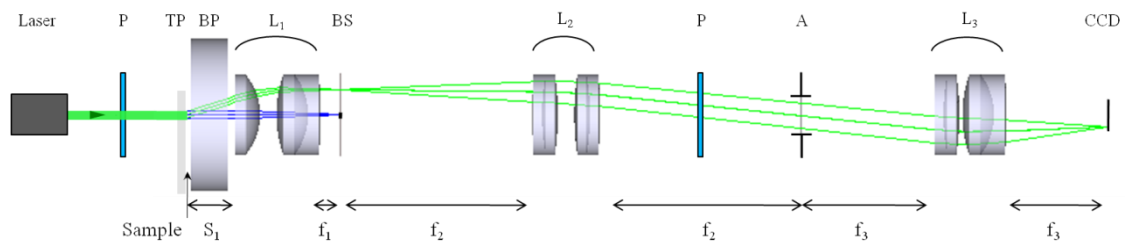


Fig. 3.16 SALSq05 setup layout. A laser beam passes through a polarizer (P) and the top plate (TP) and hits the sample. Parallel scattered light rays pass through the bottom plate (BP) and are focused on the beam stop (BS) plane by the 1st lenset (L_1), removing the transmitted beam. The 2nd (L_2) and 3rd (L_3) lensets, with an aperture (A) in their common focal plane and a polarizer (P) between them, telecentrically image the beam stop plane on the CCD sensor.

This setup conforms to all specifications described in section 3.1 and achieves an angular field ranging from 1 to 30 degrees in air. The minimum scattering angle is limited by the beam stop size, set to 300 μm of diameter in this simulation. The total length of the system, from the sample to the CCD sensor, is 148.2 mm, while the effective focal lengths of lensets L_1 , L_2 and L_3 are 8.7 mm, 35 mm and 18 mm respectively, using half inch diameter commercially available antireflection coated lenses.

The fine optimization of the relative distances between the lenses was implemented using a merit function (*Zemax* optimization Damped Least Squares algorithm), targeting the minimization of the spot size on the sensor. Since the system is spherically symmetric, the tests were performed using angular fields in the vertical (Y) direction. Figure 3.17 shows the footprint diagram (drawing of the sensor superimposed with intersecting rays) of SALSq05 setup, simulated in *Zemax*, using angular fields for $\pm 1^\circ$ (blue, pink), $\pm 10^\circ$ (green, cyan), $\pm 20^\circ$ (red, purple) and $\pm 30^\circ$ (yellow, light green). The actual size of the sensor is displayed (black square), onto which parallel rays inserting the system at different angles are focused.

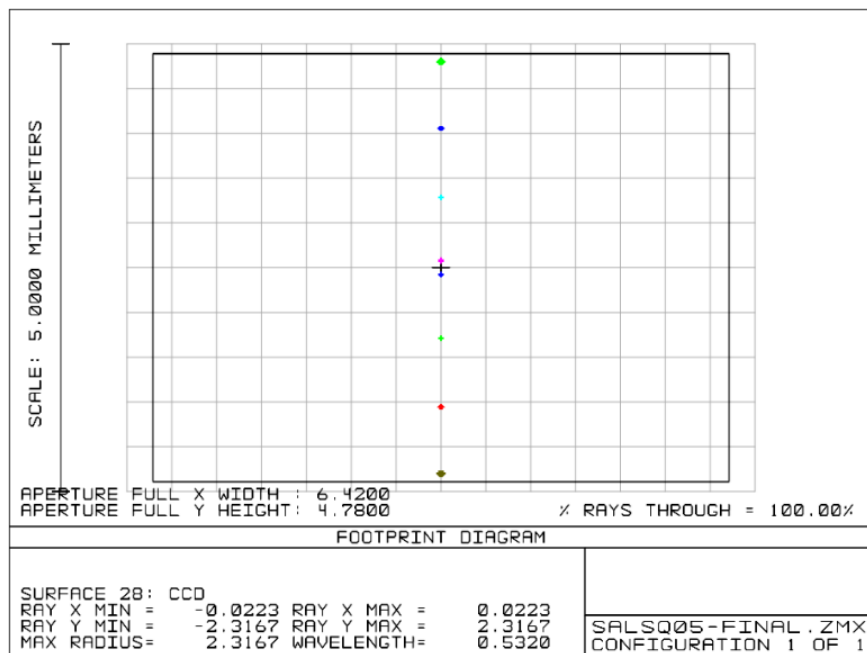


Fig. 3.17 Footprint diagram of SALSq05 setup, simulated in *Zemax*, showing rays focused on the sensor, corresponding to angular fields of $\pm 1^\circ$ (blue, pink), $\pm 10^\circ$ (green, cyan), $\pm 20^\circ$ (red, purple) and $\pm 30^\circ$ (yellow, light green). Black square stands for sensor's actual size, while black cross for the optical axis.

A better visualization of the setup's performance can be established with a spot diagram, shown in Figure 3.18. Angular fields of 1° (blue), 10° (green), 20° (red) and 30° (yellow) are tested, showing the really good results of the optimization until the 20° of angle and some aberration residues at 30° . It must be noted that the full scale is 100 μm , making these spot diagrams remarkably good.

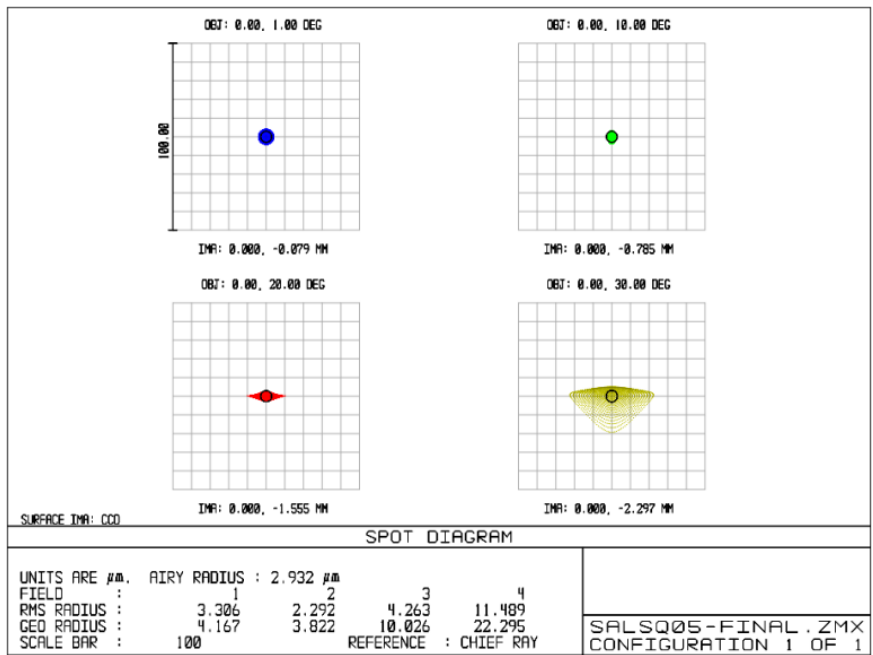


Fig. 3.18 Spot diagram of SALSq05 setup, simulated in *Zemax*, for angular fields of 1° (blue), 10° (green), 20° (red) and 30° (yellow). Full scale is 100µm, while black circles stand for the diffraction limit.

Using the whole angular field range of the setup, a diagram showing the RMS spot radius for each angle was simulated (Fig. 3.19).

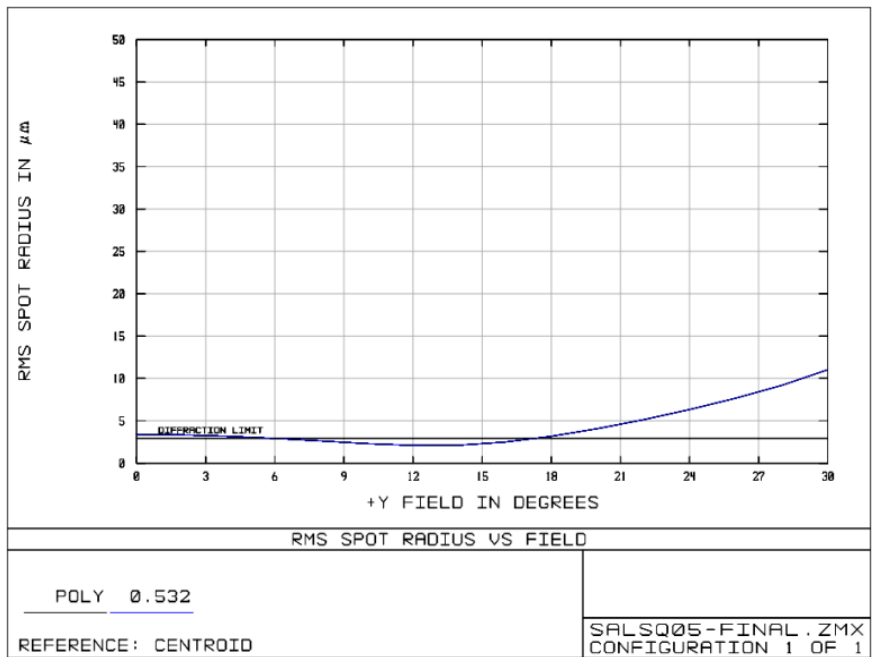


Fig. 3.19 RMS spot radius versus angular field covered by SALSq05 setup, simulated in *Zemax*. Black line represents the theoretical diffraction limit (Rayleigh criterion).

In this diagram the performance of SALSq05 can be fully evaluated. For light scattered at angles up until 18 degrees, the system appears to be diffraction limited, while for the rest angular field it remains within reasonable, acceptable spot radius values. It must be noted that the physical size of a CCD camera pixel is $4.65\mu\text{m}$. Until 20 degrees the RMS spot radius is smaller even than the actual pixel size, while the maximum RMS spot radius, being 11.5 microns, is ~ 2 pixels. Thus, the system's minimum and maximum angular resolution can be calculated to be 0.4° and 0.12° respectively.

To visualize the necessity of the optical design and optimization procedure followed in this SALS apparatus development, the RMS spot radius as a function of the angular field, for the initial simple and the final optimized system is presented in Figure 3.20. The initial simple system had a maximum RMS spot radius exceeding 350 microns, while the final optimized system concluded with a maximum RMS spot radius of 11.5 microns. Thirty times better performance was achieved.

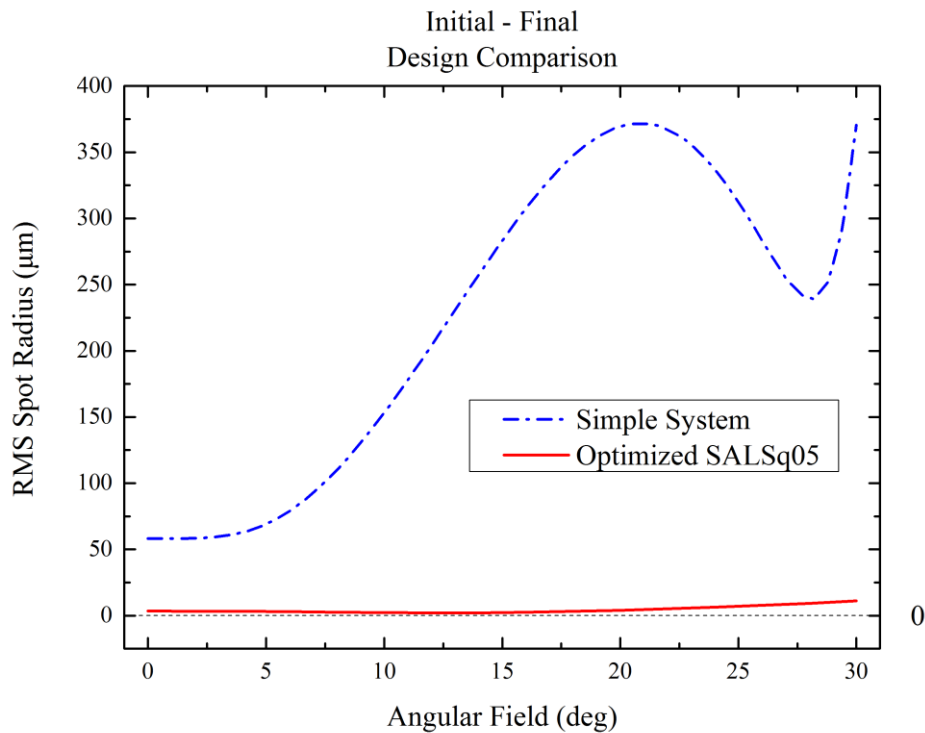


Fig. 3.20 RMS Spot Radius versus Angular Field for the initial simple system and the final optimized one, simulated in *Zemax*.

After the tests and simulations of various layouts, with different lenses and relative positions, the SALSq05 compact layout, having a maximum covered angular field of $\theta = 30^\circ$ and an average angular resolution of $\Delta\theta = \sim 0.2^\circ$, was physically realized. The fabrication involved the design of the mechanical part, which would mechanically constrain the optical parts of the setup and fit in the rheometer, as will be described in section 3.3.

SALSq05 Mode-2

The idea of having the possibility, with an additional component, the system to image the sample surface itself, was tested and a mode-2 version of SALSq05 setup was designed as well. In this mode, depending on the illumination and on the scattering conditions of the sample, the setup can be utilized either as a microscope or as to probe speckle fluctuation from multiple scattering samples. Using extended collimated white illumination in transparent samples, or a collimated coherent laser beam in opaque (multiply scattering) samples, microscopy or diffusing wave spectroscopy (DWS) measurements respectively are possible.

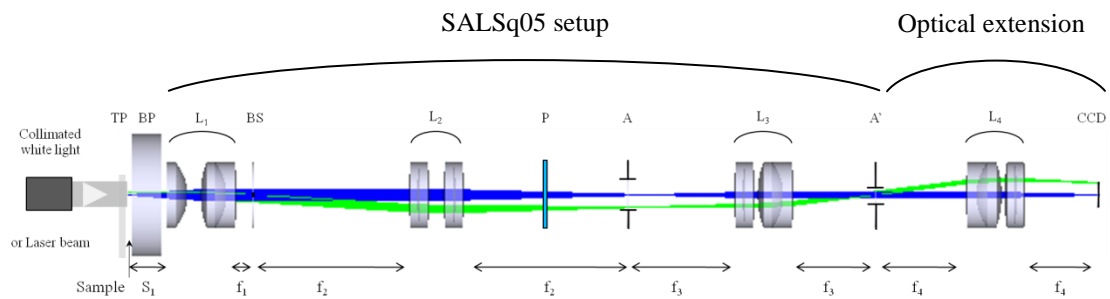


Fig. 3.21 SALSq05 mode-2 setup layout. Collimated white light or a laser beam illuminates a sample, placed between the top (TP) and bottom (BT) plate, which scatters. The setup is the same with SASLq05 with an additional lenset (L_4) placed at a distance equal to its effective focal length (f_4) from the previous CCD position. On the CCD sensor, being placed at the back focal plane of L_4 , rays from a point on the sample are focused. A second aperture (A') is placed on the common focal plane of L_3 and L_4 , acting as an aperture stop.

As seen in Figure 3.21, the additional component of mode-2 version is consisted of an aperture (A') and a fourth lenset (L_4), with 18mm effective focal length, placed between L_3 and the sensor. The additional L_4 lenset is placed at a distance equal to its effective focal length (f_4) from the back focal plane of L_3 (which was actually the previous CCD sensor position). The CCD sensor is now placed on the back focal plane of L_4 which now acts as a Fourier “inverter”. The sample, the 1st aperture and the CCD sensor planes are conjugate as well as the BS and the 2nd aperture plane. This time the first aperture (A) acts as a field stop, while the second (A') as an aperture stop of the system. The exact total magnification of the resulting system is $\times 4.25$.

A diagram showing the RMS spot radius for each point of the sensor’s vertical half field is presented in Figure 3.22. The system is diffraction limited, with an RMS spot radius of ~ 9 microns, i.e. 2 pixels, and $\sim 4 \mu\text{m}$ resolution.

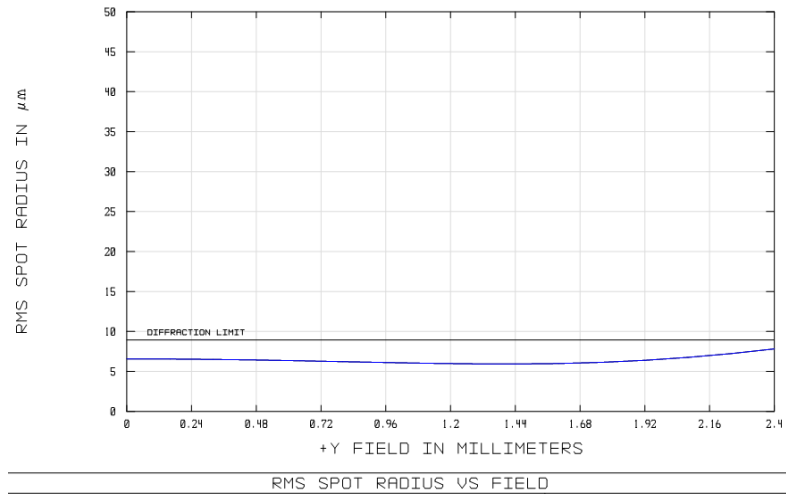


Fig. 3.22 RMS spot radius versus vertical sensor field covered by SALSq05 mode-2 setup, simulated in *Zemax*. Black line represents the theoretical diffraction limit (Rayleigh criterion).

Illumination

The illumination part of the setup was consisted of a *Roithner MSL-FN-532-20mW* laser system (specifications described in section 3.1), a *Bernhard Halle Glan-Thompson* polarizer (extinction ration better than 10^{-6}), an *Edmund Optics* neutral density (optical density OD = 3), to reduce beam power and two dielectric mirrors mounted on kinematic mirror mounts. Since the laser’s beam profile was acceptable, no additional collimation or beam manipulation was necessary. The main goal of the illumination’s part design was to bring the collimated laser beam on top of the bottom plate of the rheometer, directing it vertically through the sample and towards the acquisition part, as seen in Figure 3.23.

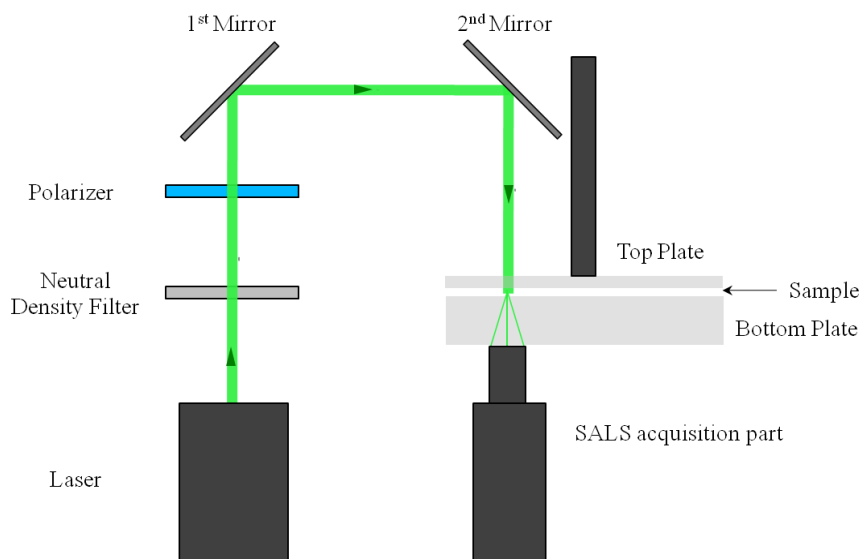


Fig. 3.23 Schematic of the illumination part, showing the beam direction from laser to SALS acquisition part.

3.3 Mechanical / Opto-mechanical Design

After the SALSq05 optical layout design was completed, the mechanical part of the system was designed. This included the acquisition part, including the lenses, the beam stop, the aperture, the analyzer and the camera, as well as the illumination part, consisting of the laser head, the polarizer, the neutral density filter and the mirrors. The whole design was implemented in a 3D CAD software.

Acquisition Part

The mechanical design process of the acquisition part was performed in parallel with the optical design of the system, since complying with space limitations introduced by the rheometer was a priority. For this part, mainly commercially available lens tubes and holders from *Thorlabs* were used in such a way, to create a user friendly device that will have the possibility to easily alternate between the two modes, give access to the user to easily rotate the analyzer and adjust the iris according to respective needs.

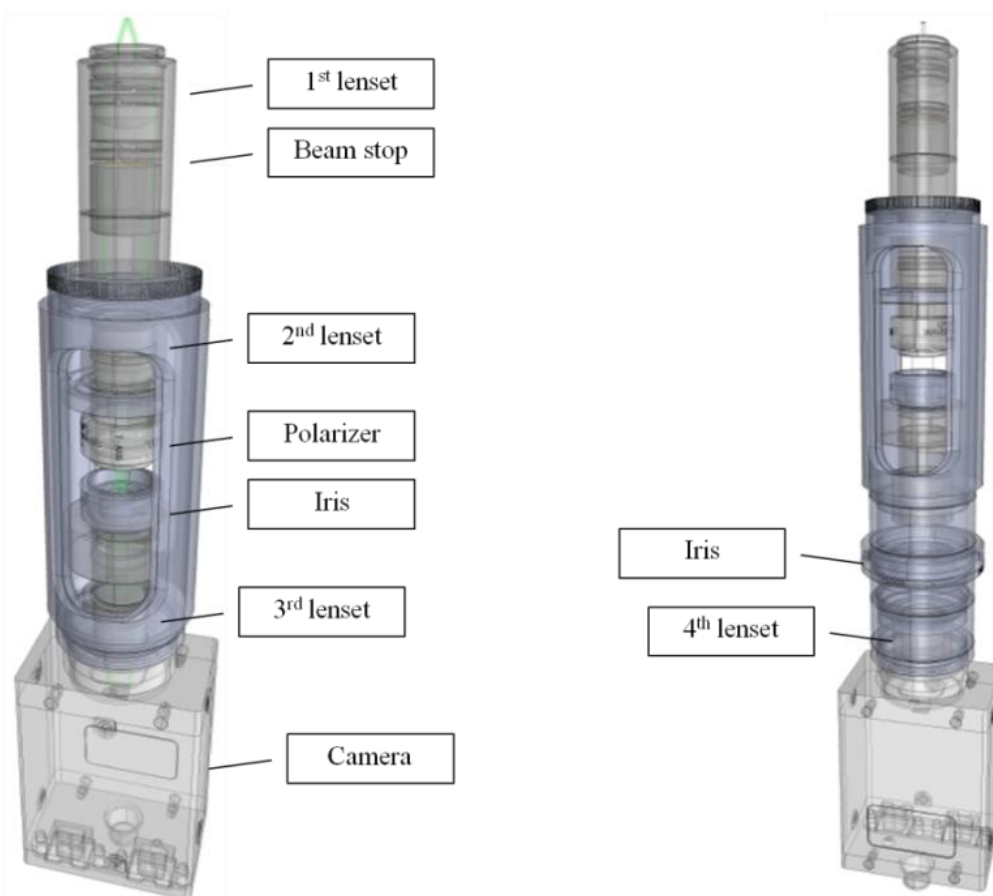


Fig. 3.24 Mechanical 3D drawing of SALSq05 (left) and mode-2 (right) acquisition part, showing the place of each element.

Figure 3.24 shows a mechanical 3D drawing of SALSq05 (left) and SALSq05 mode-2 (right) acquisition part. The positions of the elements described in the optical design are also shown. A custom made holder of the acquisition part (Fig. 3.25) was designed to connect it with the bottom plate of the rheometer, giving the ability to position the system in the right place.

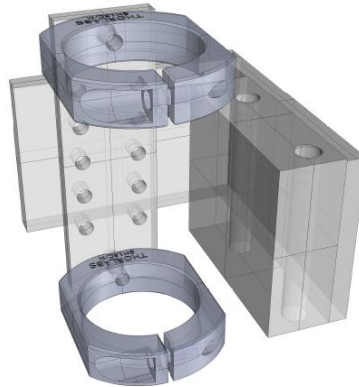


Fig. 3.25 Mechanical 3D drawing of SALSq05 acquisition part holder.

Rendered 3D images of the acquisition part of SALSq05 and SALSq05 mode-2 are presented in Figure 3.26 left and right respectively, while Figure 3.27 shows the whole acquisition part rendered, with the holder connecting it to the rheometer's bottom plate rough replica.

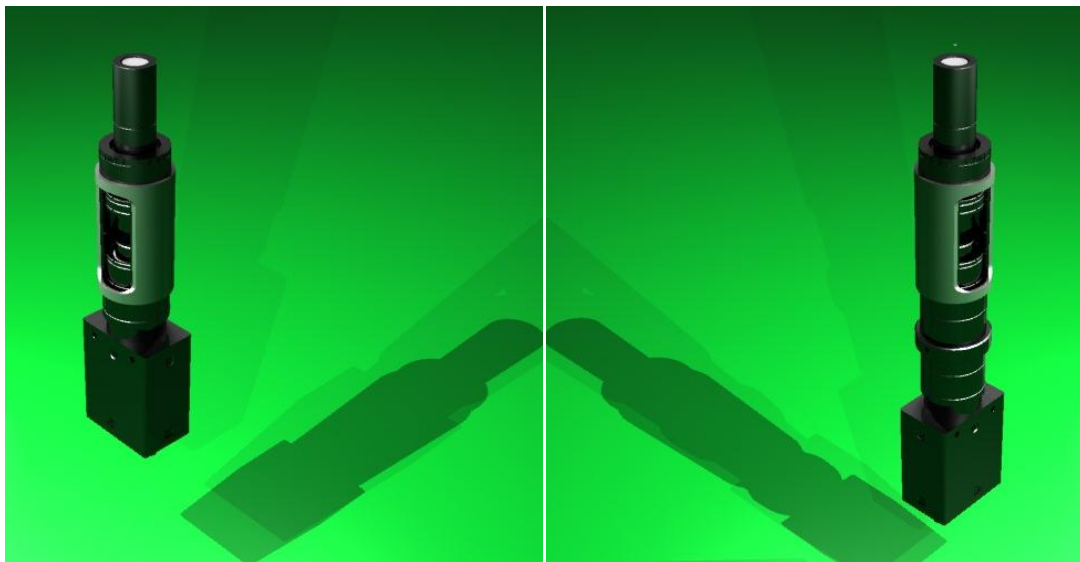


Fig. 3.26 Rendered 3D images of SALSq05 (left) and mode-2 (right) acquisition part.

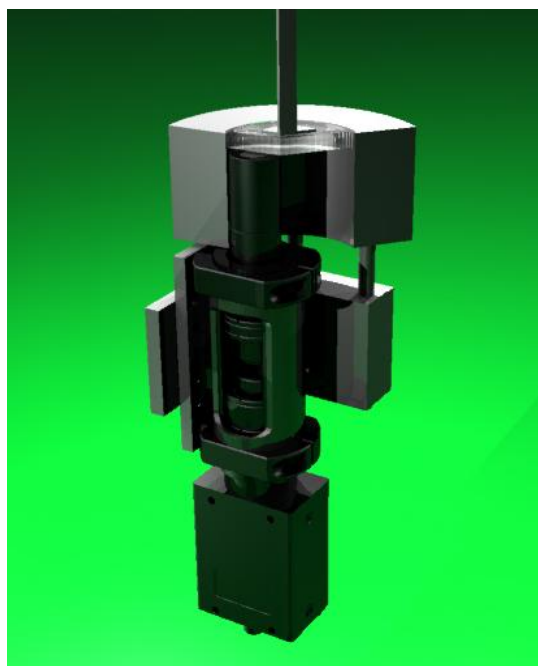


Fig. 3.27 Rendered 3D image of SALSq05 acquisition part with the holder connecting it to a rheometer's bottom plate replica.

Illumination Part

The illumination part of the setup was designed such that would bring the collimated laser beam on top of the bottom plate of the rheometer, directing it vertically through the sample and towards the acquisition part. The design had to support the laser head, a custom made mount for the neutral density filter, the polarizer and two dielectric mirrors. The two mirrors were mounted on commercially available kinematic mirror mounts (*Edmund Optics*), while the second one was additionally mounted on a x-y translation stage (*Owis*), for easier and more precise alignment. The whole arm was supported by a vertical post, mounted on the optical table. A 3D drawing of the illumination part's mechanical design is presented in Figure 3.28.

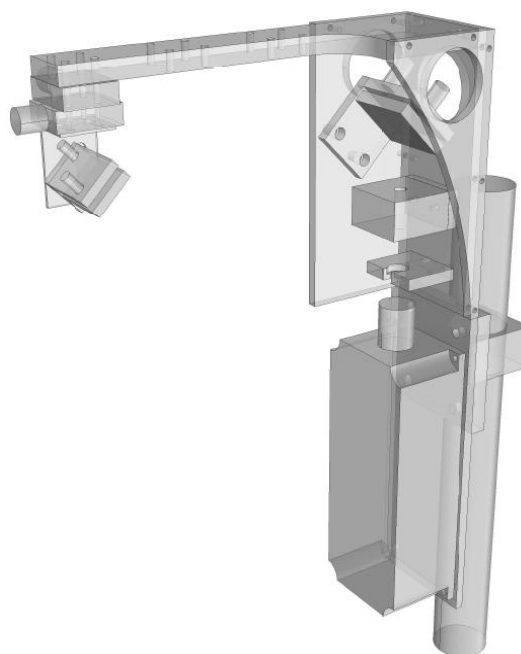


Fig. 3. 28 Mechanical 3D drawing of SALSq05 illumination part.

Full setup

To visualize the full SALSq05 mechanical setup mounted on a replica of the rheometer's bottom plate, a 3D rendered image is presented in Figure 3.29. The green laser beam is also illustrated and all parts of the system are denoted.

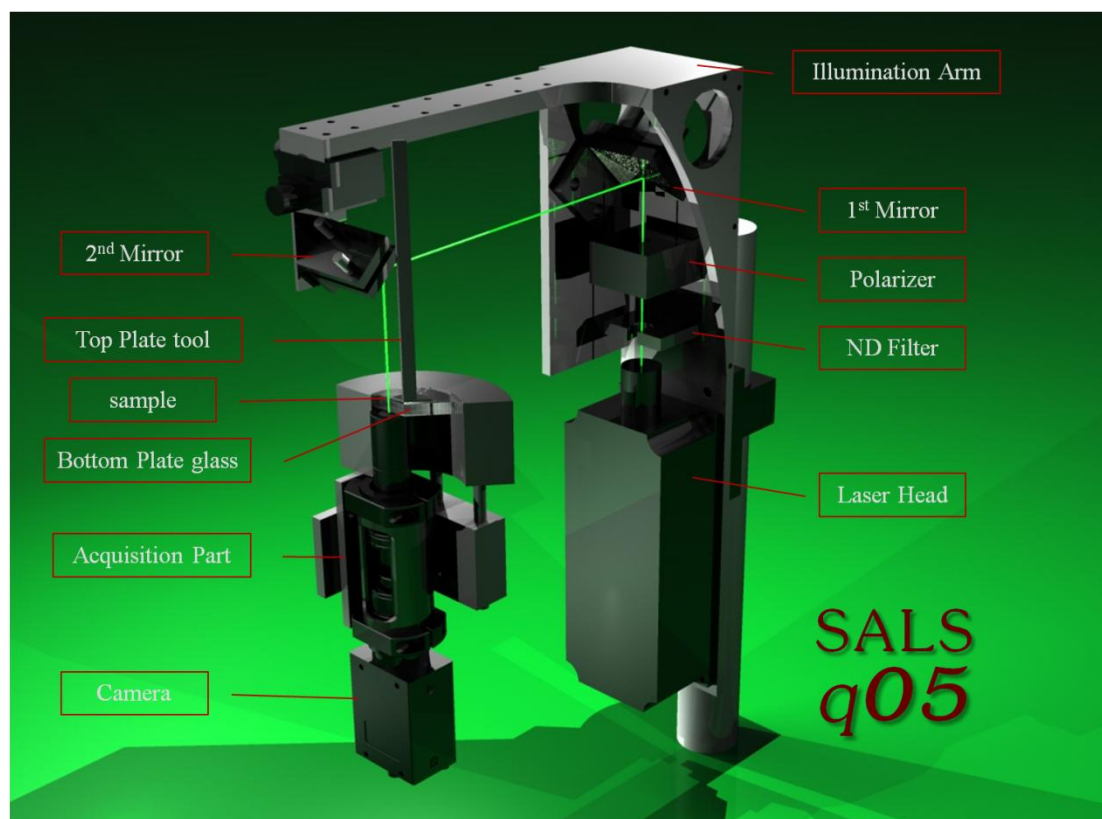


Fig. 3.29 Rendered 3D image of SALSq05 full setup, mounted on the rheometer's bottom plate replica, noting all parts of the system. The green laser beam is also illustrated.

3.4 SALSq05 Setup Realization

After the completion of both the optical and optomechanical design of SALSq05 setup, the commercially available parts required were ordered, while custom design parts were constructed.

One last part that has not been mentioned yet, is the beam stop. This part was custom made, using a 12.5 mm diameter, 150 μm thickness round glass coverslip, which was precisely marked in the center with black mat paint. The procedure was implemented using a guided needle that produced a uniform, centered, small black point on the coverslip. A typical example of the ones that were selected to be used in the system, was of 650 μm diameter and is shown mounted on a les tube in Figure 3.30.



Fig. 3.30 Photo of the 650 μm diameter beam stop, mounted on a lens tube.

Subsequently the assembling of the whole system took place. Figure 3.31 shows photos of the SALSq05 acquisition part (top) and the mode-2 version of it (bottom), while Figure 3.32 shows the SALSq05 acquisition part with the holder that connects it to the rheometer.



Fig. 3.31 Photos of the realized SALSq05 acquisition part (top) and mode-2 version of it (bottom).

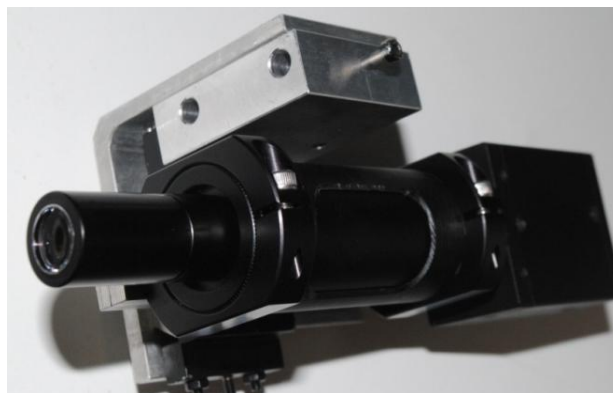


Fig. 3.32 Photo of the realized SALSq05 acquisition part with the holder that connects it to the rheometer.

The way the acquisition part is mounted on the rheometer can be seen in Figure 3.33, while the full setup is presented in Figure 3.34. The rheometer used is an *Anton Paar MCR 302 WESP*.

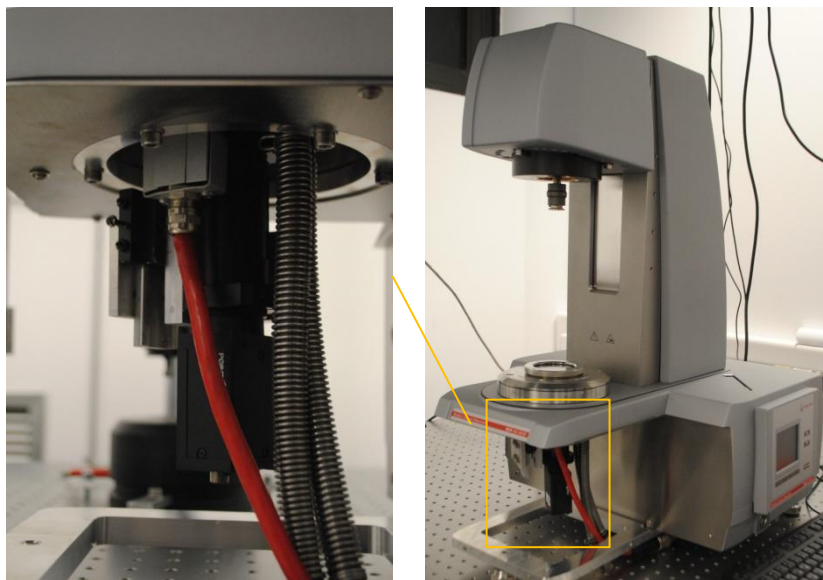


Fig. 3.33 SALSq05 acquisition part mounted on an *Anton Paar MCR 302 WESP* rheometer.

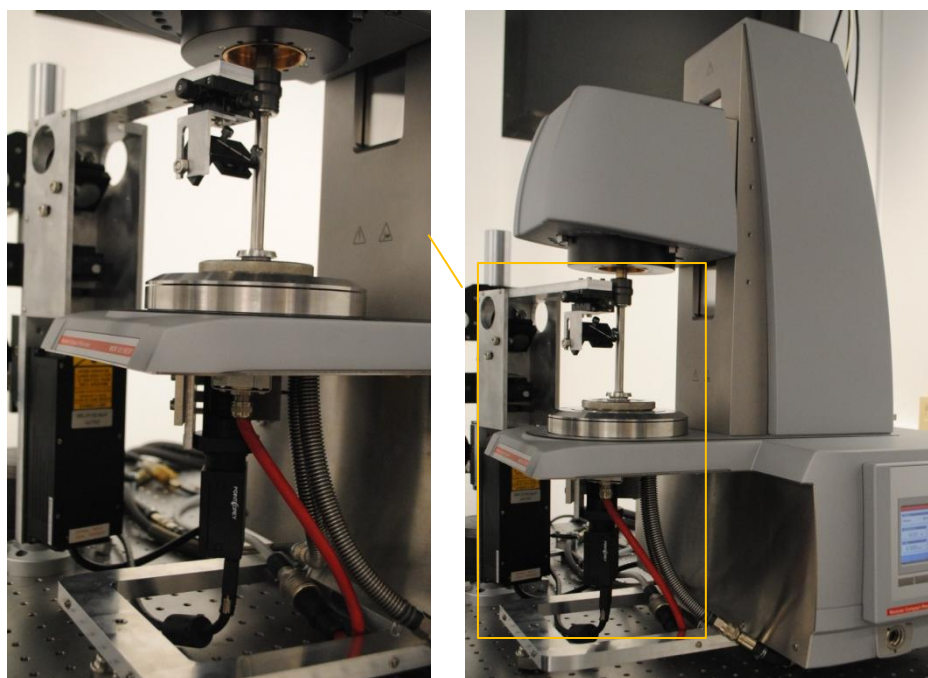


Fig. 3.34 SALSq05 full setup mounted on an *Anton Paar MCR 302 WESP* rheometer.

3.5 Angular Calibration

The SALSq05 apparatus was angularly calibrated with the use of a diffraction grating ruler. The calibration was verified by measuring the angular distribution of the diffraction pattern of a known circular pinhole.

3.5.1 Calibration using a Diffraction Grating

A graticule of 100 lines per millimeter from *GRATICULES LTD*, shown in Figure 3.35, was used as a diffraction grating to calibrate the angular distribution of the setup.

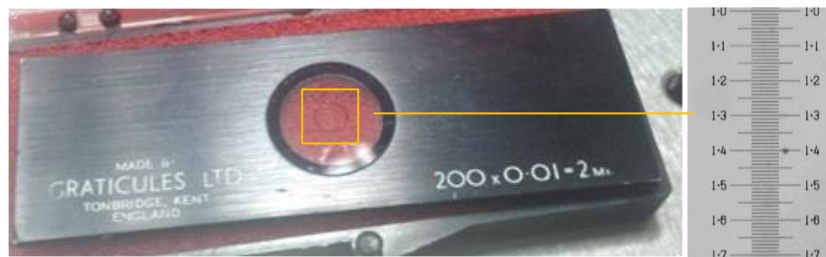


Fig. 3.35 Graticule of 100 lines/mm used for angular calibration

The graticule was placed in the sample position so that the collimated laser beam was diffracted in several orders as described in Figure 3.36. The angle of diffraction (θ) for several orders (m) depends on the laser wavelength (λ), and the spacing of the grating lines (d) following equation^{16,35}:

$$d \cdot \sin \theta = m \cdot \lambda \quad (3.2)$$

In our case the laser wavelength was $\lambda = 532\text{nm}$, while the spacing between the lines $d = 10\mu\text{m}$. With this arrangement, by acquiring an image of the diffraction pattern and analyzing it in respect to the optical axis, each diffraction order corresponds to a known diffraction angle and consequently a camera pixel mapping can be achieved.

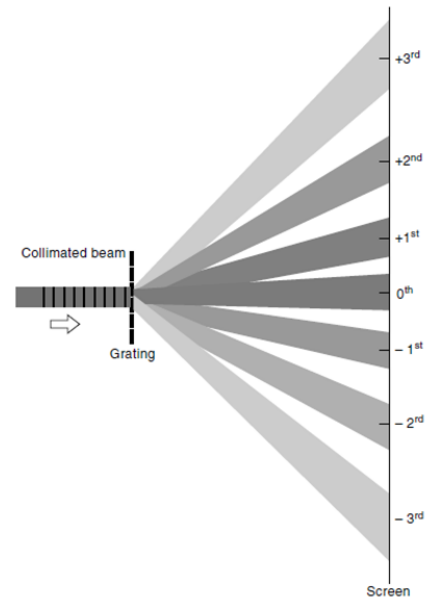


Fig. 3.36 Diffraction of a collimated beam from a grating.

Figure 3.37 shows a cropped image of the diffraction pattern resulted from the graticule and measured by the SALSq05 apparatus. An intensity look up table (LUT) has been applied through *ImageJ* to visually distinguish the diffraction orders (white spots).



Fig. 3.37 Diffraction pattern of a 100 lines/mm graticule as acquired by SALSq05 apparatus. (false colors)

The intensity distribution of the diffracted beam, measured in pixels from the zero order position is shown in Figure 3.38.

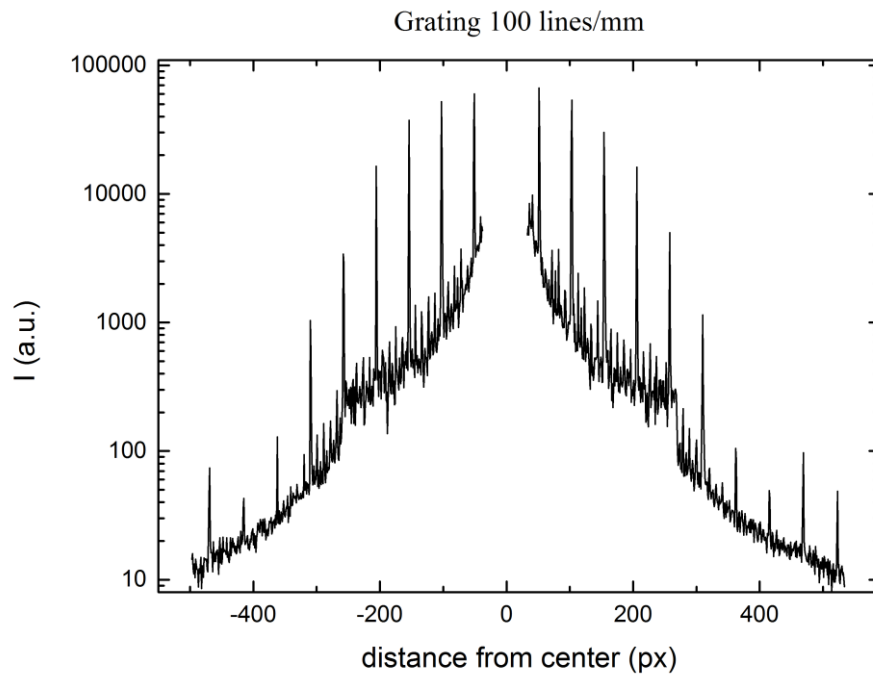


Fig. 3.38 Intensity distribution of the 100 lines/mm graticule diffraction pattern versus distance (in pixels) measured from the zero order.

The expected diffraction angle for each diffraction order was estimated using equation 3.2 and was plotted as a function of the corresponding position (in pixels) on the CCD image, measured from zero order, as shown in Figure 3.39. Then by applying a linear fit we get:

$$\theta = -0.2 + 0.061 \cdot px, \quad (3.3)$$

where θ is angle of diffraction in degrees and px is the distance from the optical axis measured in pixels. Thus the angular scaling factor in our setup is 0.061 deg/pixel. The result of the fit shows excellent angular linearity of the SALSq05 setup, since the adjusted coefficient of determination (R^2) equals to 0.999. Apart from this, the angular range of the setup was verified, confirming *Zemax* simulations and exceeding 30° in air.

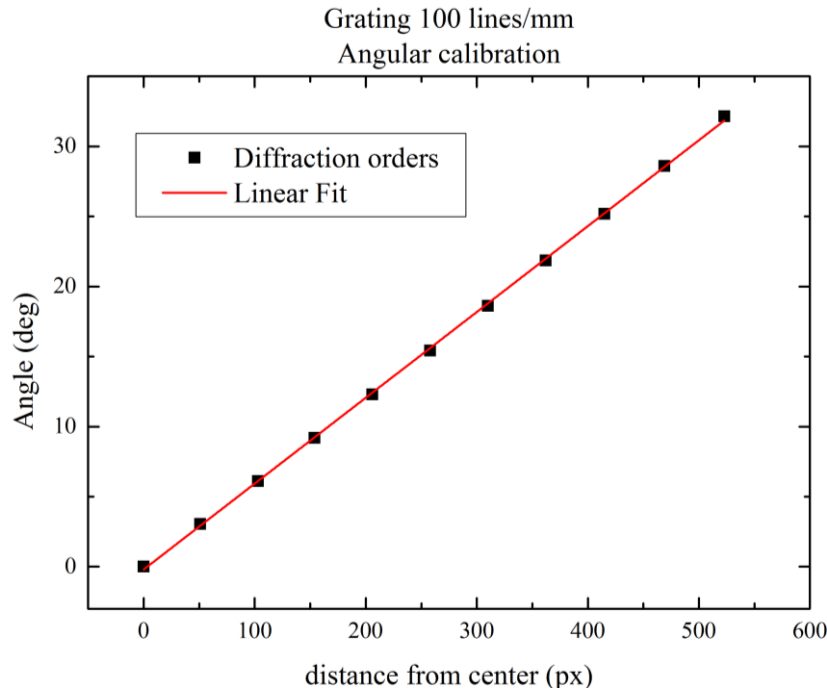


Fig. 3.39 SALSq05 angle to pixel mapping through the 100 lines/mm graticule measurement. Fitting shows systems angular linearity.

This way, an angle to pixel mapping was achieved, while the angular performance of the SALSq05 setup was remarkably good.

3.5.2 Calibration Verification using a Pinhole

A circular pinhole of 10 μ m diameter from *THORLABS* was used to verify the angular calibration of SALSq05 setup.

The pinhole was placed in the sample position with the use of a x-y translation mount, such that the collimated laser beam was passing from the center of the pinhole resulting in maximum intensity in the camera. The resulting diffraction pattern is predicted in theory to be a disk surrounded by concentric rings, also known as Airy disk. Measurements with and without the beam stop were performed (Fig. 3.40), to inspect for possible effects of the beam stop. Two acquisition times were used for each measurement to cover a larger dynamic intensity range.

The intensity distributions were radially averaged, using *ImageJ*, in respect to the optical axis and using the measured angular scaling factor (0.061 deg/pixel). The normalized results are shown in Figure 3.41 together with the Airy function distribution as predicted by the Fraunhofer diffraction theory^{16,35}. The pinhole inspection under an optical microscope revealed a diameter of 10.3 \pm 0.7 μ m and some deviations from a perfectly circular shape, which can justify some discrepancies of the measured intensity values in respect to theory. Another cause of these discrepancies can be silver highly reflecting material of the pinhole.

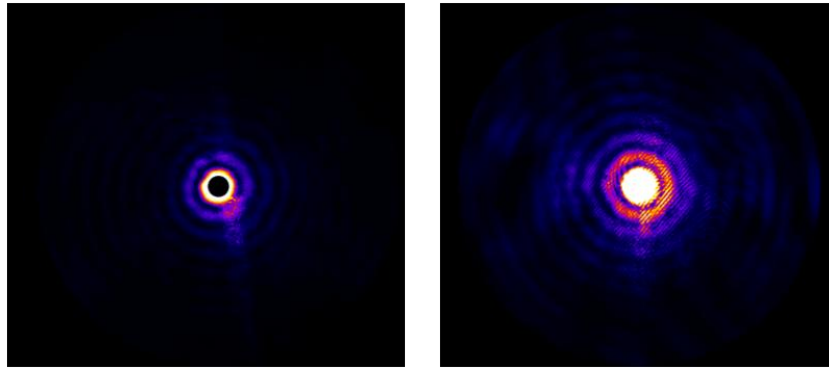


Fig. 3.40 Airy disk images from 10 μm pinhole, with (left) and without beam stop (right), measured with the SALSq05 apparatus.

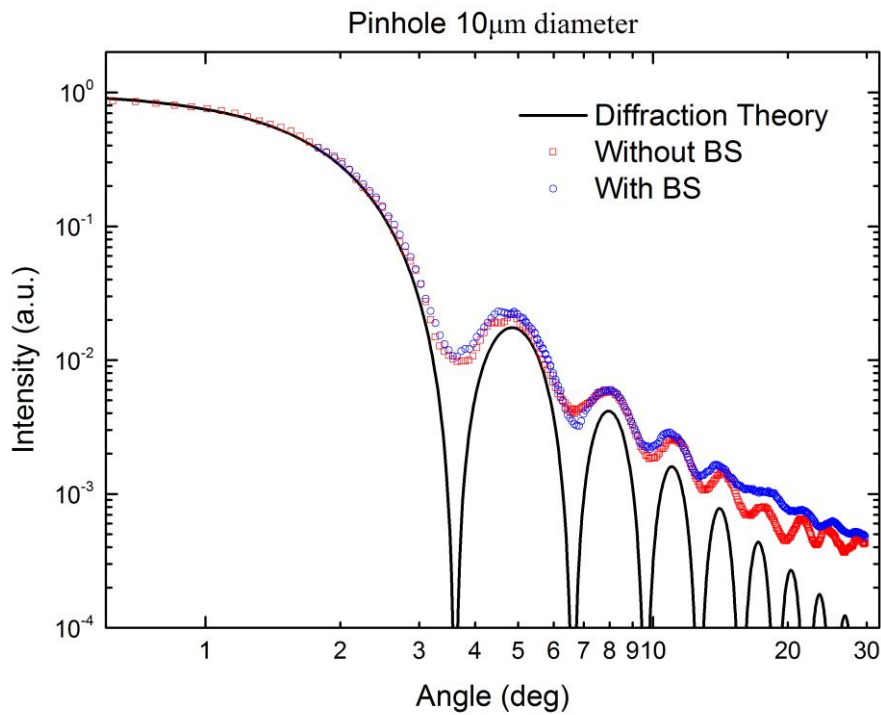


Fig. 3.41 Normalized radially averaged intensity distribution of diffracted beam by 10 μm pinhole, measured with SALSq05 apparatus, with (\circ) and without (\square) beam stop and theoretical Airy function curve (black line).

Our angular calibration is verified since the maxima/minima positions of the Airy distribution are well reproduced in Figure 3.41. The presence of the beam stop may have a small effect in higher angles due to additional straylight.

Concluding, the SALSq05 setup was successfully calibrated and verified for its angular performance and following its intensity distribution performance was tested.

3.6 Depth of Field Correction

Sample thickness and position can have an effect on the angular distribution of the intensity on the image, a phenomenon known as vignetting. In order to quantify and correct (by a post processing calibration function) for any vignetting effects we have used a ground glass diffuser as a uniform scatterer, at various distances from the entrance face of the SALSq05 setup. There is an obvious difference in measured intensity scattered at different angles when the scattering medium is displaced (Fig. 3.42). This is caused by the narrow depth of field (DOF) of the SALSq05 setup, an inevitable side loss to meet size and angular field requirements.

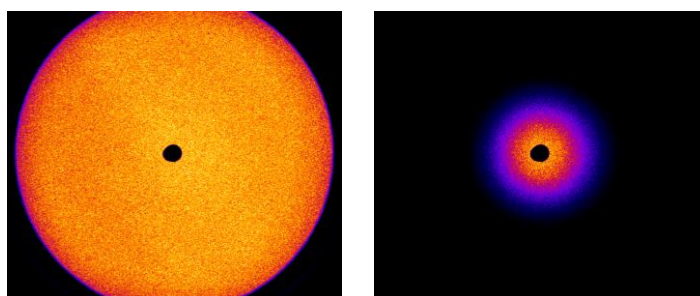


Fig. 3.42 Scattered intensity by a ground glass diffuser placed at optimum focus (left) and at -4mm from optimum focus (right), measured with the SALSq05 apparatus.

Nevertheless, this DOF caused vignetting is fully predictable, and can be calculated and corrected as a function of sample thickness. Figure 3.43 shows the acquired radially averaged scattered intensity (I) over scattering angle for different diffuser distances from optimum focus plane (4 mm from entrance face of the system).

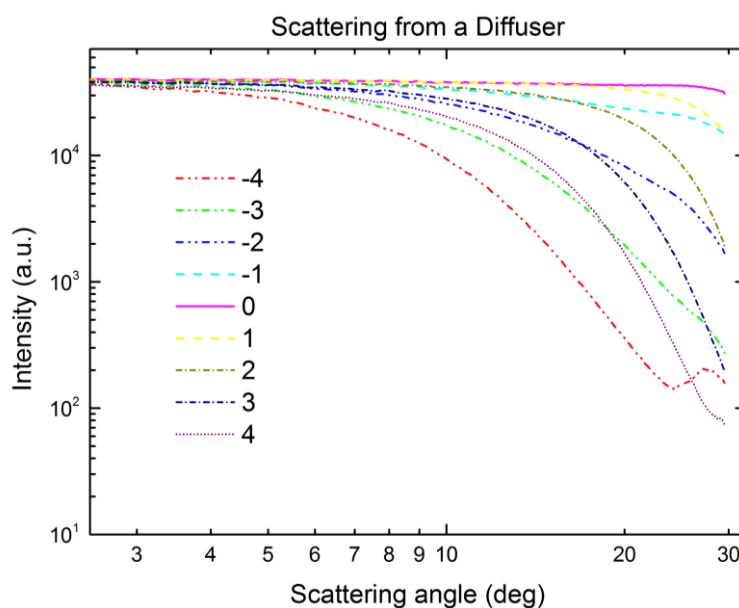


Fig. 3.43 Radially averaged scattered intensity distribution from a ground glass diffuser versus scattering angle at various distances from optimum focus plane, measured with the SALSq05 apparatus.

The intensity distribution at optimum focus is apparently ideal, while when the scattering plane changes the scattered intensity collected by SALSq05 setup decreases at high angles. Taking the normalized intensities at various angles as a function of scattering plane distance from optimum focus, one can identify the Gaussian profile of most distributions, as seen in Figure 3.44.

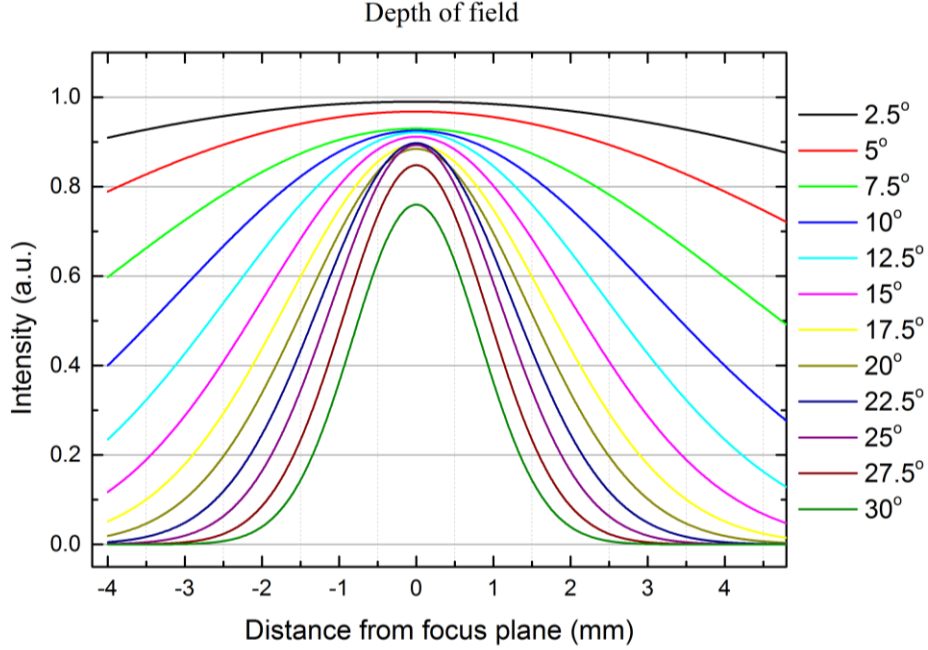


Fig. 3.44 Gaussian fits of the radially averaged scattered intensity distributions from a ground glass diffuser versus distance from optimum focus plane, for various scattering angles as acquired from the SALSq05 apparatus.

The Gaussian fit performed for each scattering angle according to the following equation:

$$y = y_o + \left(\frac{A}{w \sqrt{\frac{\pi}{4 \ln(2)}}} \right) e^{-4 \ln(2) \left(\frac{x-x_c}{w} \right)^2}, \quad (3.4)$$

where y_o is the base, x_c the center, A the area and w the full width at half maximum (FWHM). Here we set the parameters of base y_o and center x_c equal to zero.

Consequently the varying parameters for the different profiles are the total area A and the FWHM w . These are indicators of the acquired depth of field at each angle, being wide at low angles and narrower at higher angles. This means that for a sample of $L = 5$ mm thickness for example, placed with its center on the optimum focus plane of the setup, the setup will acquire at 2.5° the scattered intensity almost equally from scatterers being anywhere in the sample. On the other hand, at 30° although the scattered intensity from scatterers in the center of the sample will be acquired, that

from ones that are at the edges of it will not reach the detector. These variations depend on the thickness of the sample, for which a correction of the acquired scattering data must be applied.

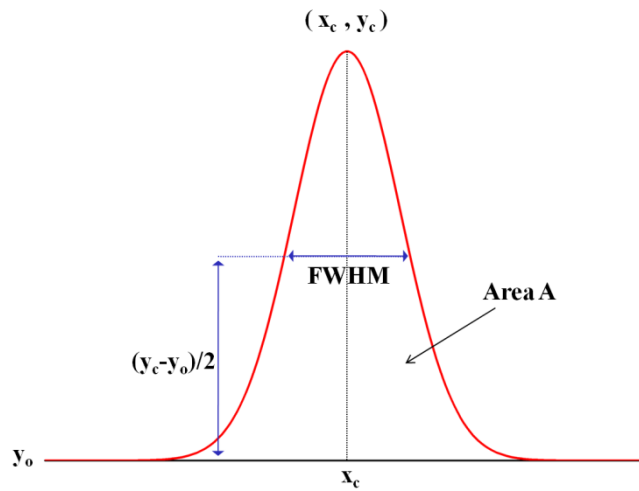


Fig. 3.45 Gaussian function representation and parameters.

For each scattering angle intensity profile, shown in Figure 3.44, the fitting parameters A and w were extracted. After plotted as a function of scattering angle they were finally fitted to asymptotic curves $y = a - b \cdot c/x$ (Fig. 3.46). These curves represent the change of the depth of field and the acquired scattered intensity of the setup as a function of scattering angle.

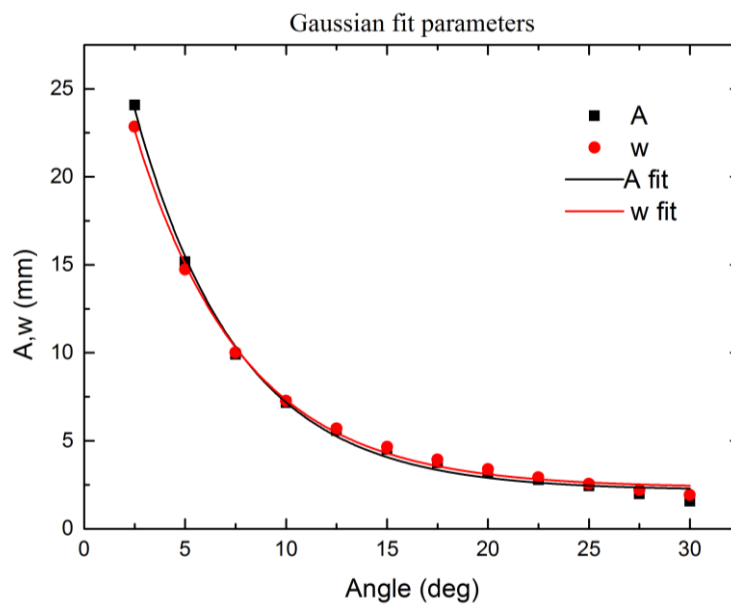


Fig. 3.46 Gaussian fit parameters A (Area) and w (FWHM) as a function of scattering angle (\blacksquare, \bullet) and asymptotic curve fittings (lines), representing the change of the depth of field and the acquired scattered intensity of the setup as a function of scattering angle.

Consequently, the acquired scattered intensity I for a certain scattering angle θ at a distance x from the optimum focal plane will be:

$$I(\theta, x) = \left(\frac{A(\theta)}{w(\theta) \sqrt{\frac{\pi}{4 \ln(2)}}} \right) e^{-4 \ln(2) \left(\frac{x}{w(\theta)} \right)^2} \quad (3.5)$$

Considering a sample of thickness L , the definite integration of equation 3.5 with upper and lower limits of $L/2$ and $-L/2$ respectively will give the expected scattered intensity distribution of the sample, which will account for its thickness L .

$$I(\theta, L) = \frac{A(\theta)}{w(\theta) \sqrt{\frac{\pi}{4 \ln(2)}}} \int_{-L/2}^{L/2} e^{-4 \ln(2) \left(\frac{x}{w(\theta)} \right)^2} dx \quad (3.6)$$

$$C(\theta, L) = A(\theta) \operatorname{erf} \left[\frac{L \sqrt{\ln(2)}}{w(\theta)} \right], \quad \operatorname{erf}(x) = \frac{2}{\sqrt{\pi}} \int_0^x e^{-u^2} du \quad (3.7)$$

The result of the integration (equation 3.7) provides the correction factor $C(\theta, L)$ which is a function of the sample thickness L and scattering angle θ and can be used to correct the scattered intensity profile acquired by the SALSq05 setup, accounting for system vignetting and sample thickness. The correction application is implemented by dividing the acquired scattering profile with $C(\theta, L)$.

Figure 3.47 shows an example of this correction application on the radially averaged scattered intensity profile of polystyrene spherical particles ($R = 0.98 \mu\text{m}$, $n = 1.604$) diluted in water solvent ($n = 1.332$) as measured with the SALSq05 setup. The sample thickness was $L = 1 \text{ mm}$. Comparing the uncorrected and corrected data to the corresponding Mie theory curve, the necessity of this correction is outlined.

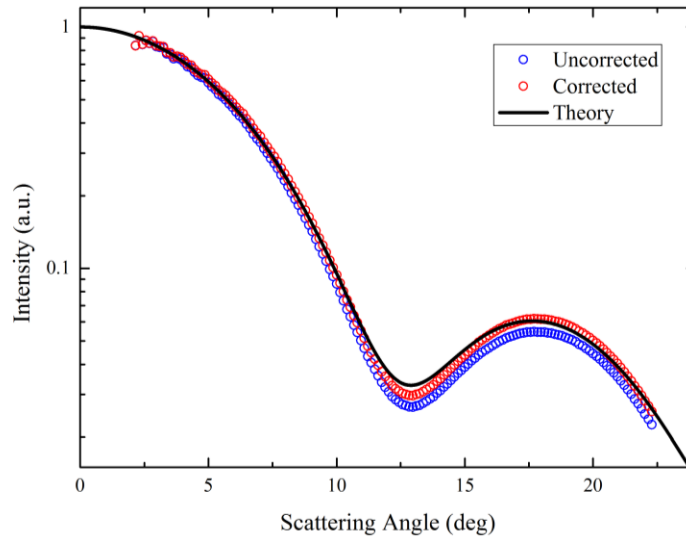


Fig. 3.47 DOF correction application example showing the radially averaged scattered intensity profile of polystyrene spherical particles ($R = 0.98 \mu\text{m}$, $n = 1.604$) diluted in water solvent ($n = 1.332$), measured with the SALSq05 setup (\circ), the same data after correction application (\circ) and the corresponding Mie theory curve (solid line).

CHAPTER 4

DILUTE COLLOIDAL SUSPENSIONS

A series of different samples, containing a variety of spherical particles, solvents and sample thickness both in cuvettes and on a rheometer were measured to assess the SALSq05 performance. Dilute colloidal suspensions of spherical particles were chosen for this evaluation, since the scattering patterns from such particles, at the single scattering regime, can be also analytically described through Mie scattering theory, thus a direct comparison can be performed.

4.1 Samples

In Table 4.1 all the characteristics of the samples that were measured and analyzed are summarized. All particles were spherical.

Sample Name	PS10	PS5	PS2	M3	P689
Particle Material	Polystyrene	Polystyrene	Polystyrene	Melamine	PMMA
Particle Nominal Radius	5.22 μm	2.45 μm	0.98 μm	1.5 μm	0.64 μm
Medium	Pure Water	Pure Water	Pure Water	Dodecane	Dodecane
Particle RI	1.604	1.604	1.604	1.68	1.493
Medium RI	1.332	1.332	1.332	1.42	1.42

Table 4.1 Measured samples' properties.

The PS10, PS5, PS2 and M3 particles' nominal sizes refer the supplier's catalog values, while the nominal size of P689 was measured with a conventional static light scattering *ALV* goniometer apparatus. The refractive index of each medium was measured with an *Atago Abbe Refractometer 3T*, while all samples were dilute enough to remain in the single scattering regime.

It must be noted that all solvents used, were filtered through 0.2 μm filters to avoid scattering from dust or particles other than the ones of interest.

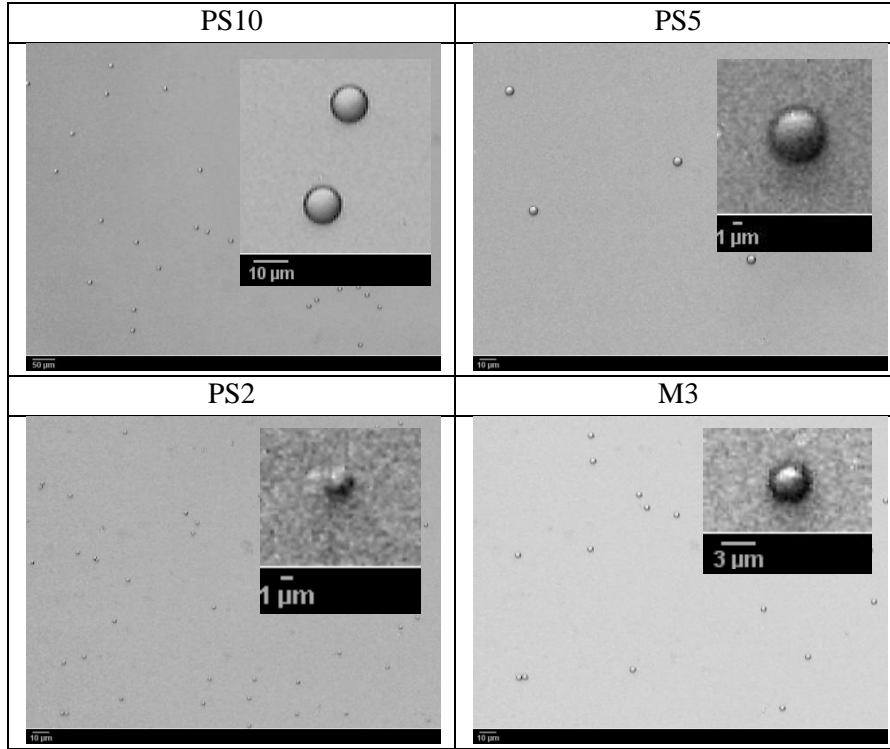


Table 4.2 Images of the samples PS10, PS5, PS2 and M3 through an optical microscope.

4.2 Measurement & Analysis

For each measurement, the sample was prepared and stored at room temperature. The cuvettes used (*Hellma* quartz glass cuvettes of different thicknesses, from 1mm to 5 mm) or the rheometer's (*Anton Paar MCR 302 WESP*) bottom and top plate were thoroughly cleaned, since dust particles and impurities affect a lot the scattering pattern acquired. After the SALSq05 setup was prepared for measurement, the sample was loaded and left at rest for 30 minutes with the laser beam blocked (to avoid thermal effects). Afterwards the laser beam was unblocked, the exposure time of the camera was alternated to measure at an extended dynamic intensity range without saturation and 100 images of the sample's scattering pattern were captured with a framerate of 20 frames per second. Keeping the same exposure time, the laser beam was blocked and 50 images of the camera's dark noise were captured. Then the sample was unloaded, the cuvette or the top and bottom plate of the rheometer was thoroughly cleaned again and the solvent alone was loaded, at the same position. 50 images of the solvent scattering pattern were then captured.

Using *ImageJ* image processing software and a macro code written for this purpose each stack of images was averaged. The averaged dark noise image was subtracted from the averaged sample and solvent separately and finally the dark subtracted solvent image was subtracted from the dark subtracted sample image, following equation:

$$\text{Image}_{\text{subtracted}} = [\text{Image}_{\text{sample}} - \text{Image}_{\text{dark}}] - T \cdot [\text{Image}_{\text{solvent}} - \text{Image}_{\text{dark}}] \quad (4.1)$$

Before the final subtraction the dark subtracted solvent was corrected for the sample transmission ($T = \text{Transmission}_{\text{Sample}} / \text{Transmission}_{\text{Solvent}}$), because the straylight contribution is decreased when part of the incident beam is scattered by the sample⁹. Transmission was measured by a power meter and using a pinhole that was letting only the transmitted laser beam pass.

The necessity of dark subtraction for the sample and the solvent is shown in Figure 4.1. Here we show all intermediate images until the final subtracted image, in false colors and brightness adjusted (maximum is set to 1000 counts out of 65536), in order to easily distinguish the effect of dark noise to the data. From the dark noise image (Fig. 4.1 c) one can see that here dark noise varies from 1 to 1000 counts and is distributed unevenly among the pixels of the sensor. This makes the dark noise subtraction imperative, since it affects each pixel's intensity value differently.

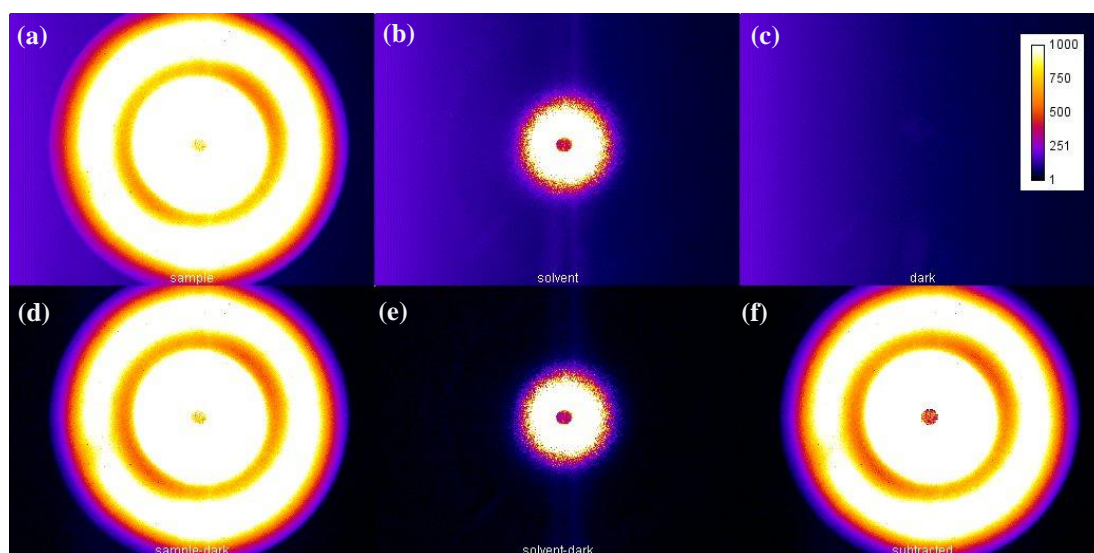


Fig. 4.1 Series of all intermediate images until the final subtracted image, in false colors and brightness adjusted (maximum set to 1000 counts out of 65536), to visualize the necessity of dark noise subtraction. (a) Sample image, (b) Solvent image, (c) Dark noise image, (d) Dark subtracted Sample image, (e) Dark subtracted Solvent image, (f) Final subtracted image. Dark noise varies here from 1 to 1000 counts and is distributed unevenly among the pixels of the sensor, affecting each pixel's intensity value differently.

The same set of images is shown in Figure 4.2 with full intensity representation of the captured and edited images. Here the necessity of the solvent subtraction is visually evaluated. The raw solvent image (Fig. 4.2 b) and consequently the dark - subtracted solvent image (Fig. 4.2 e) contains scattered light not only from the solvent alone but also from the optical elements of the system and the cuvette or rheometer top and bottom plate. Thus it is imperative, for the data to be reliable, to measure it at exactly the same conditions with the sample and subtract it to keep the net scattered intensity that is due to the probed particles.

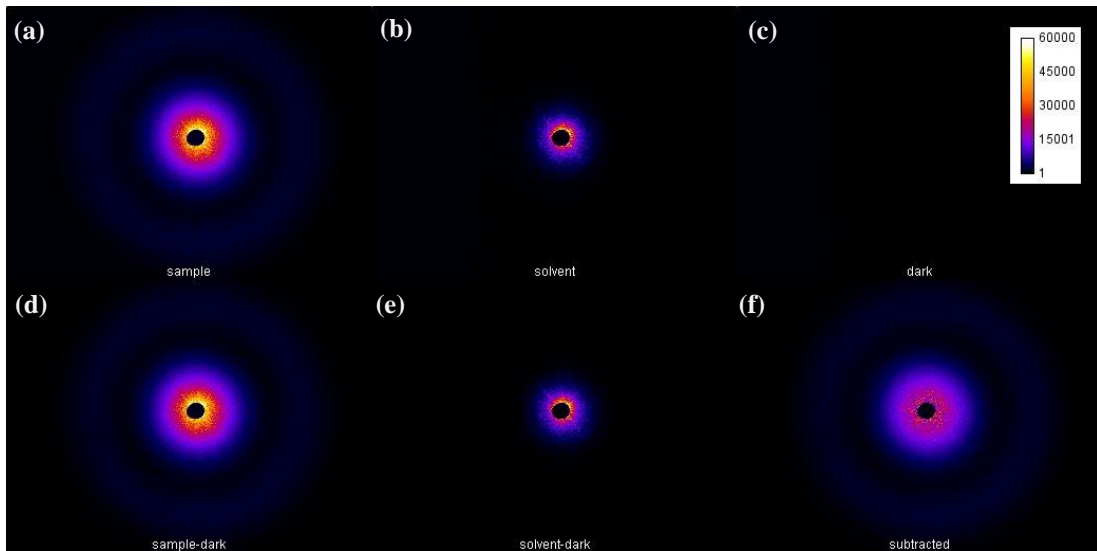


Fig. 4.2 Series of all intermediate images until the final subtracted image, in false colors and with full intensity representation. (a) Sample image, (b) Solvent image, (c) Dark noise image, (d) Dark subtracted Sample image, (e) Dark subtracted Solvent image, (f) Final subtracted image. Solvent image contains light scattered from the solvent and the optical elements of the setup, making its subtraction imperative, in order to extract the net scattering from the probed particles.

The final subtracted image was then imported and analyzed using a specialized, Matlab based, analysis software that was developed in this thesis. The analysis software is autonomous (executable file) and the user interacts through a user-friendly graphical interface, shown in Figure 4.3. With the SALSq05 analysis software the user can automatically, or manually, find the center of the scattering pattern, plot the radial average of the scattered intensity as a function of scattering angle, apply the depth of field correction calibration $C(\theta, L)$ of the SALSq05 setup by setting the thickness of the sample, and compare the measured data with theoretical Mie scattering curves. Finally, the user can fit the results to Mie theory and thus estimate the nominal radius of the sample, with its 95% confidence intervals.

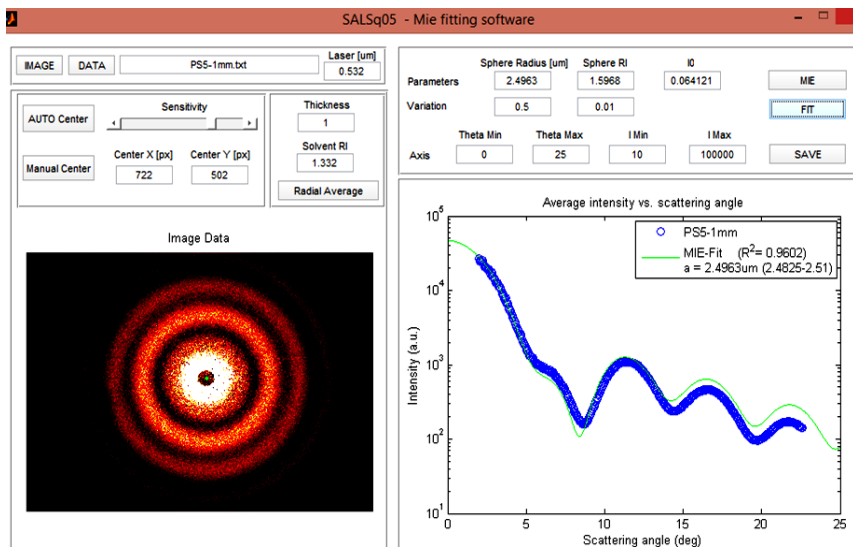


Fig. 4.3 SALSq05 software with user friendly graphic interface used for SALS image analysis.

Using SALSq05 software we plotted the radially averaged scattered intensity of each measurement, fitted the result with Mie theory and thus estimated the nominal radius of the measured spherical particles (R). For all fits, the coefficient of determination was greater than 0.95, denoting that our results are in very good agreement with Mie theory.

4.3 Standard Deviation Alternative Analysis

An alternative novel way of image data analysis was also tested. Since the dynamic variation of the solvent alone is expected to be negligible in comparison to the dynamics of the measured particles, analysis of the standard deviation (STD) of the images taken from the sample, without solvent subtraction, could give the same relative intensity distribution with the ‘‘Solvent Subtracted Average’’ way of analysis, already described.

Standard deviation σ is the square root of variance σ^2 which is defined as the mean quadratic deviation of the variable from its mean value⁴¹. Here for each pixel would be:

$$\sigma_{px}^2 = \langle (I_t - \langle I \rangle)^2 \rangle, \quad (4.2)$$

where brackets denote average and I_t is the intensity at frame t .

The intensity I is the sum of the actual scattered intensity from the sample S and the background intensity B . Thus equation 4.2 becomes:

$$\sigma_{px}^2 = \langle (S_t + B_t - \langle S \rangle - \langle B \rangle)^2 \rangle \quad (4.3)$$

Since the background intensity fluctuation is expected to be negligible, each frame’s background intensity will be equal to the average one, $B_t = \langle B \rangle$, resulting to:

$$\sigma_{px}^2 = \langle (S_t - \langle S \rangle)^2 \rangle \quad (4.4)$$

Now S is fluctuating due to Brownian motion of the particles around the mean value $\langle S \rangle$, which is a random process. So it will be $S_t = \langle S \rangle + A_t \cdot \langle S \rangle$, where A_t is a factor ranging from -1 to 1. Consequently equation 4.4 becomes:

$$\sigma_{px}^2 = \langle (A_t \cdot \langle S \rangle)^2 \rangle = \langle A_t^2 \rangle \cdot \langle S \rangle^2, \quad (4.5)$$

$$\sigma_{px} = \sqrt{\langle A_t^2 \rangle} \cdot \langle S \rangle \quad (4.6)$$

where now A_t^2 takes values from 0 to 1. If the system is ergodic, the average $\langle A_t^2 \rangle$ will be the same at every pixel. This results to the same distribution between the standard deviation and the average of the scattered intensity from an ergodic sample, differentiated by a factor of $\sqrt{\langle A_t^2 \rangle} = 0.7$.

An STD analysis was implemented using the sample PS2 which consisted of polystyrene spherical particles with 0.98 μm nominal radius diluted in pure water and measured on a rheometer with 1mm sample thickness. Using *ImageJ*, the standard deviation image of the 100 sample images, captured at 20 frames per second, was estimated, from which the standard deviation of the dark noise images was subtracted as:

$$\text{Image}_{\text{STD}} = \{\text{Image}_{\text{sample}}\}_{\text{STD}} - \{\text{Image}_{\text{dark}}\}_{\text{STD}} \quad (4.2)$$

Figure 4.4 shows the “Average”, the “Solvent Subtracted Average” and the “Standard Deviation” of the sample.

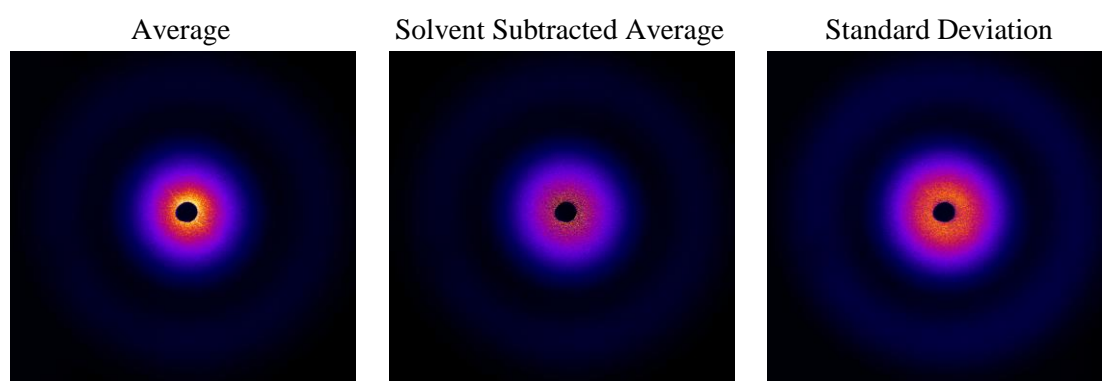


Fig. 4.4 Average of the sample images (left), Average of the sample images with solvent subtraction (center) [conventional way of analysis followed also in this work] and standard deviation of sample (right) [novel way of analysis to be tested].

The scattering pattern of the STD way of analysis (Fig. 4.4 right) shows great similarity to the Solvent Subtracted Average one (Fig. 4.4 center). It is remarkable how the central high intensities close to the beam stop (black center circle), which are caused by straylight scattering of the laser beam by the optical elements (obvious in Fig. 4.4 left), are diminished the same way in both cases.

For a better comparison Figure 4.5 shows the normalized radially averaged values of both ways of analysis (Mean - STD) in the same plot. The values actually overlap, implying that this novel way of standard deviation analysis can be very promising, since there is no need for an extra measurement of the solvent alone, allowing for inline and flow measurements useful for particle sizing. Nevertheless, further tests should be performed to validate this kind of analysis.

Following the same way of analysis, another sample was tested. Melamine spherical particles diluted in dodecane solvent and measured in a 2 mm sample thickness cuvette were analyzed with both ways. The normalized results are presented in Figure 4.6. Again the STD way of analysis is in agreement with the Solvent Subtracted Average one. This time, some deviations appear at high q values ($q > 3 \mu\text{m}^{-1}$). These may be due to some possible flow of the particles in the cuvette.

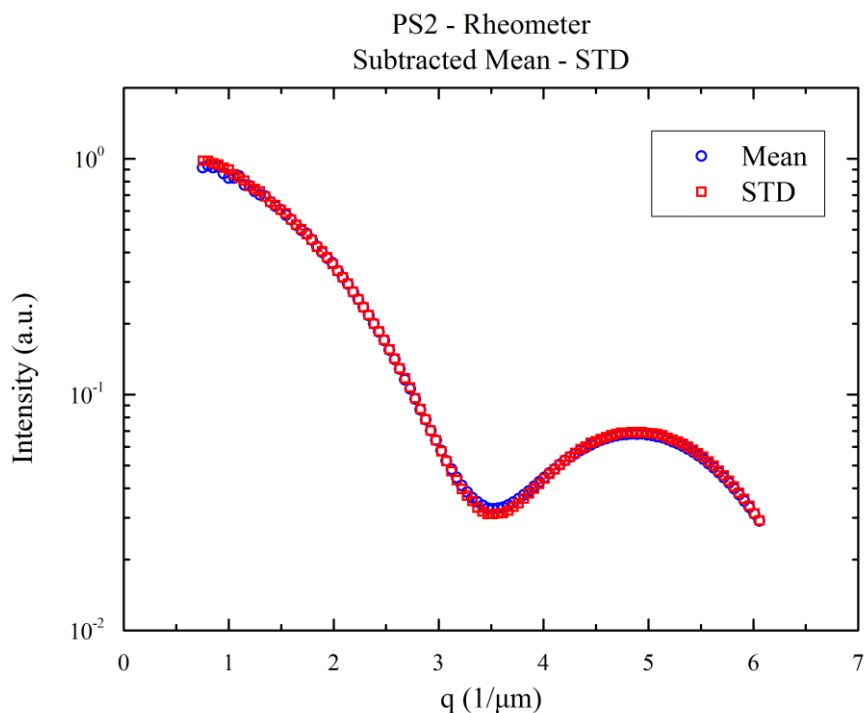


Fig. 4.5 Radially averaged intensities over scattering vector q of Solvent Subtracted Average way of analysis (\circ) and Standard Deviation one (\square) for PS2 sample measured on a rheometer with 1 mm sample thickness. Sample was polystyrene spherical particles ($R = 0.98 \mu\text{m}$) diluted in pure water. Data are normalized to maximum value.

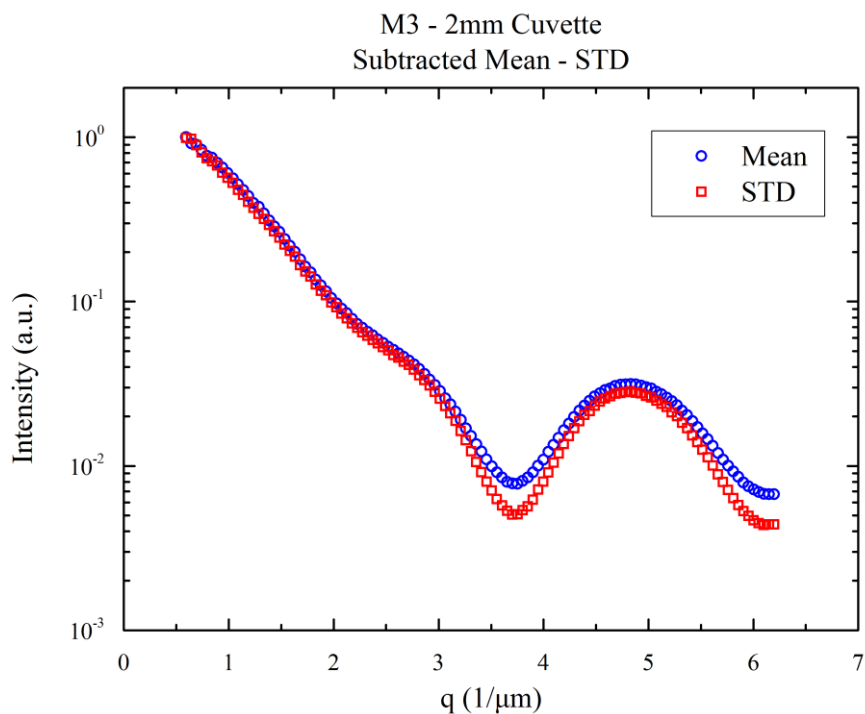


Fig. 4.6 Radially averaged intensities over scattering vector q of Solvent Subtracted Average way of analysis (\circ) and Standard Deviation one (\square) for M3 sample measured in a 2 mm sample thickness cuvette. Sample was melamine spherical particles ($R = 1.5 \mu\text{m}$) diluted in dodecane solvent. Data are normalized to maximum value.

Before adopting this novel way of SLS analysis, rigorous tests must be performed to quantify the effects of various parameters on it and define its advantages and disadvantages over the conventional one. For this reason in this work the conventional solvent subtraction average way of analysis was followed.

4.4 Evaluation Tests Results

Bellow we present results from various performance tests conducted with the previously described samples and methods. Apart from the Mie fitting analysis, the simpler Rayleigh-Gans-Debye (RGD) analysis was performed as well, to compare the two extracted size values.

PS10

The sample PS10, which was polystyrene spheres with 5.22 μm nominal radius diluted in pure water, was measured in a cuvette of 5 mm sample thickness. Figure 4.7 shows the results of this measurement after image data analysis. The final result of the Mie fit yields a particle radius of $R = 5.06 \mu\text{m}$. The fit is relatively good and the result shows less than 5% deviation from the nominal radius value. The discrepancies between experimental and theoretical minima may be due to sample's small amounts of polydispersity which smooth out the scattering pattern minima. The specific sample, due to the large relative refractive index ($m = 1.2$) and particles' size, it does not satisfy the RGD criterion. This results in the observed discrepancies between Mie and RGD fits.

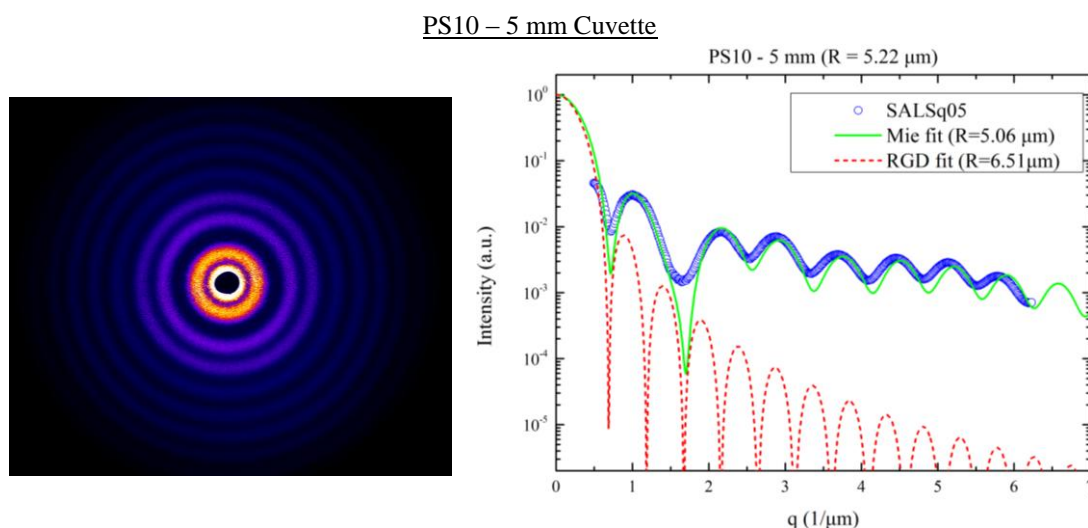


Fig. 4.7 Subtracted scattering pattern image of PS10 sample measured in a 5 mm sample thickness cuvette with SALSq05 setup (left). Experimental radially averaged scattered intensity versus scattering vector (right, \circ) and fitted curves according to Mie (right, green solid line) and RGD (right, red dashed line) theory.

PS5

Polystyrene spherical particles of 2.45 μm nominal radius diluted in pure water (sample PS5), were measured in two different cuvettes. Their sample thickness was 1 mm and 5 mm. Figure 4.8 and 4.9 show the results of the two measurements after image data analysis respectively. Again the RGD criterion is not satisfied resulting in large discrepancies between the experimental data and RGD fit. On the other hand, the Mie fits are relatively good, resulting in a particle radius of $R = 2.52 \mu\text{m}$ for the 1 mm sample thickness and $R = 2.53 \mu\text{m}$ for the 5 mm sample thickness. Both results deviate less than 5% from the nominal radius value.

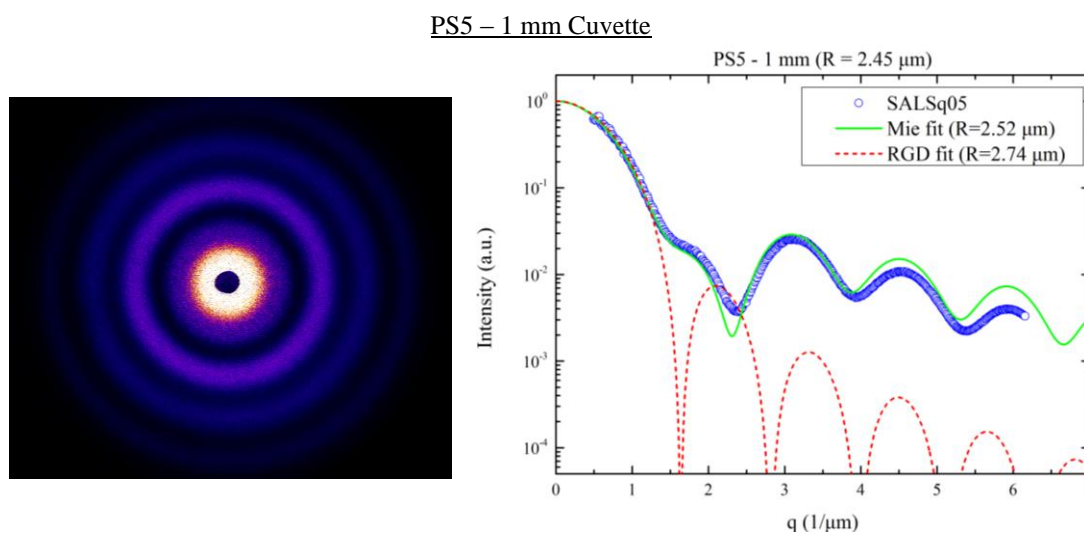


Fig. 4.8 Subtracted scattering pattern image of PS5 sample measured in a 1 mm sample thickness cuvette with SALSq05 setup (left). Experimental radially averaged scattered intensity versus scattering vector (right, \circ) and fitted curves according to Mie (right, green solid line) and RGD (right, red dashed line) theory.

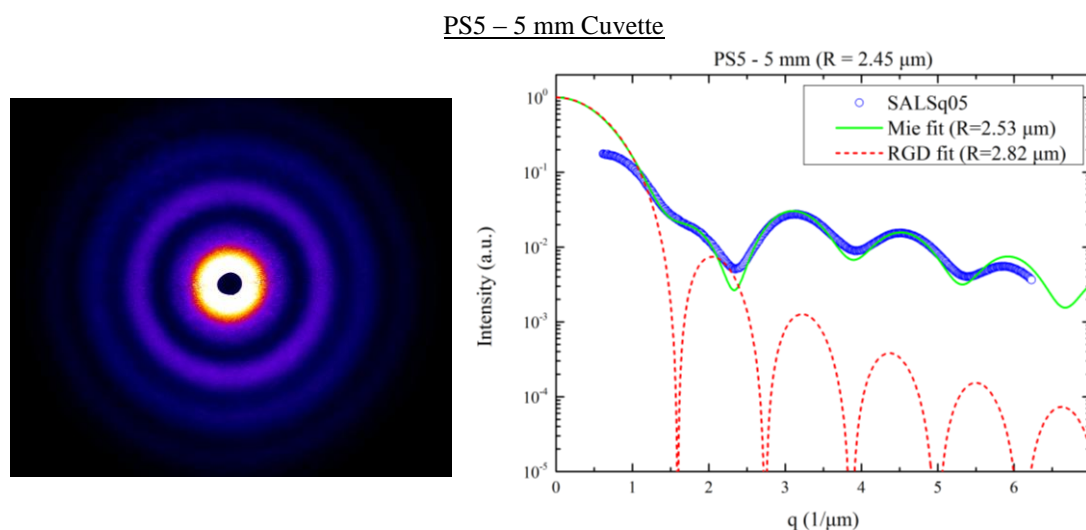


Fig. 4.9 Subtracted scattering pattern image of PS5 sample measured in a 5 mm sample thickness cuvette with SALSq05 setup (left). Experimental radially averaged scattered intensity versus scattering vector (right, \circ) and fitted curves according to Mie (right, green solid line) and RGD (right, red dashed line) theory.

The small discrepancies in the first minimum between experimental and Mie theory values may again be attributed to possible small amounts of polydispersity. Furthermore, since the same sample measured at two different sample thicknesses resulted practically to the same result, confirms that the depth of field correction, that was described in the previous chapter, is correct. Thus the SALSq05 setup is capable of reliably measuring samples of different thickness.

PS2

Following some even smaller polystyrene spherical particles (nominal radius $R = 0.98 \mu\text{m}$) diluted in pure water (sample PS2), were measured in a cuvette of 2 mm sample thickness and on a rheometer having 1mm sample thickness. The results of the two measurements after image data analysis are presented in Figures 4.10 and 4.11. The Mie fits are excellent and result to a particle radius of $R = 0.94 \mu\text{m}$ and $R = 0.95 \mu\text{m}$ for the cuvette and rheometer measurement respectively. These results show less than 3% deviation from the nominal radius value. Although the RGD criterion is not yet satisfied, from the RGD fitted curves, one can observe an excellent agreement with the experimental scattered intensities at very low scattering angles ($q < 3 \mu\text{m}^{-1}$). On the other hand, significant deviations appear at higher scattering angles ($q > 3 \mu\text{m}^{-1}$), since the refractive index contrast between the particles ($n_{particle} = 1.604$) and the solvent ($n_{solvent} = 1.332$) is large. Still the RGD theory is not applicable.

Again, two different sample thicknesses were used, this time in a cuvette and on a rheometer. Both measurements result in relatively the same radius value, denoting that SALSq05 setup can reliably measure samples loaded on a rheometer as well.

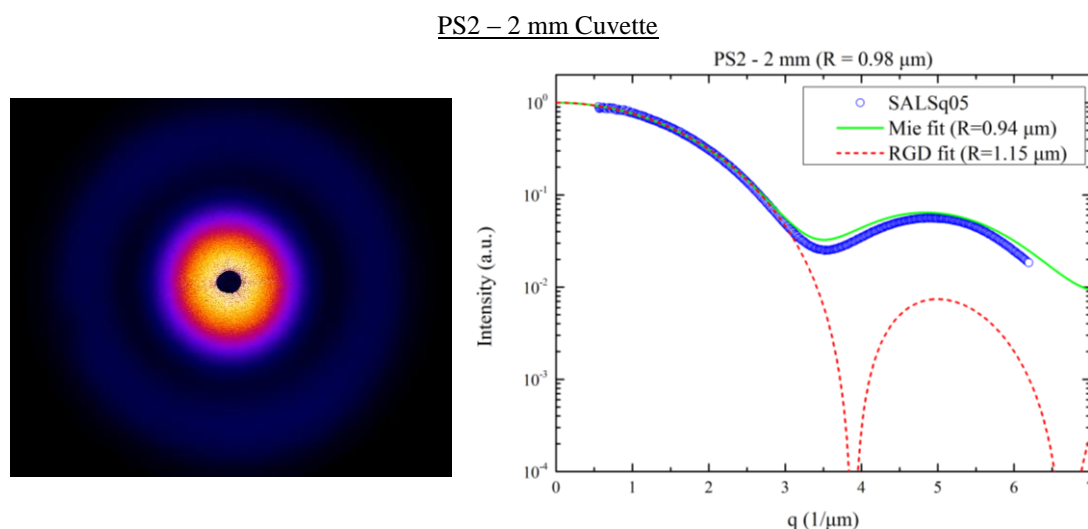


Fig. 4.10 Subtracted scattering pattern image of PS2 sample measured in a 2 mm sample thickness cuvette with SALSq05 setup (left). Experimental radially averaged scattered intensity versus scattering vector (right, \circ) and fitted curves according to Mie (right, green solid line) and RGD (right, red dashed line) theory.

Remarkably, the measurement on the rheometer shows excellent agreement with Mie theory. The goodness of this measurement, compared to the respective in the cuvette, lays on the fact that SALSq05 was optimized for measurements on the

rheometer. The rheometer's bottom plate was taken into account in the optical design of the setup, slightly affecting its performance positively.

PS2 – 1 mm gap on Rheometer

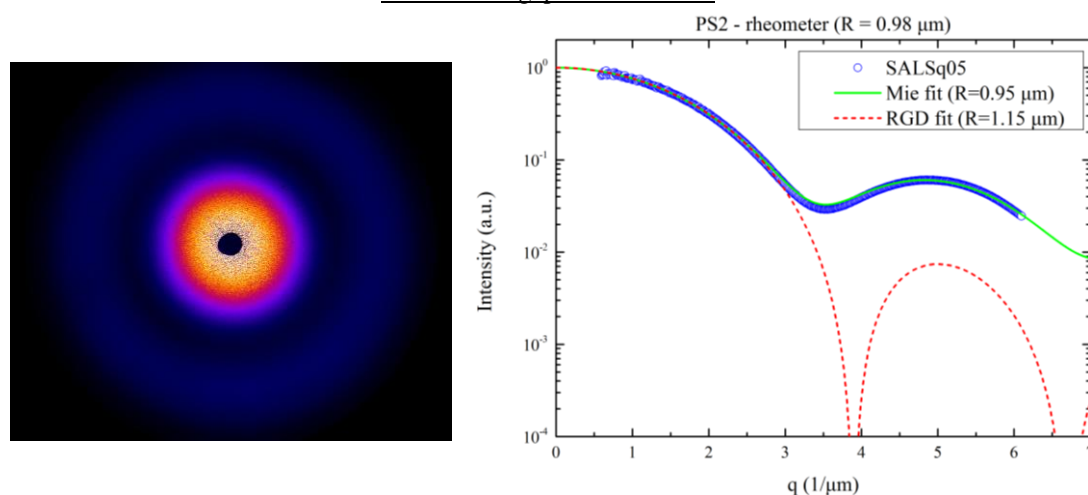


Fig. 4.11 Subtracted scattering pattern image of PS2 sample measured on a rheometer having 1 mm sample thickness with SALSq05 setup (left). Experimental radially averaged scattered intensity versus scattering vector (right, \circ) and fitted curves according to Mie (right, green solid line) and RGD (right, red dashed line) theory.

M3

After measuring polystyrene particles of different size in water, we proceeded with particles of different material in another solvent to further test the setup's response in a completely different sample. This time, melamine spherical particles of 1.5 μm nominal radius diluted in dodecane solvent, were measured in a cuvette of 2 mm sample thickness. In Figure 4.12 are presented the results of this measurement after image data analysis. The final result of the Mie fit provides a particle radius of $R = 1.5 \mu\text{m}$ which is an exact match to the nominal radius value.

M3 – 2 mm Cuvette

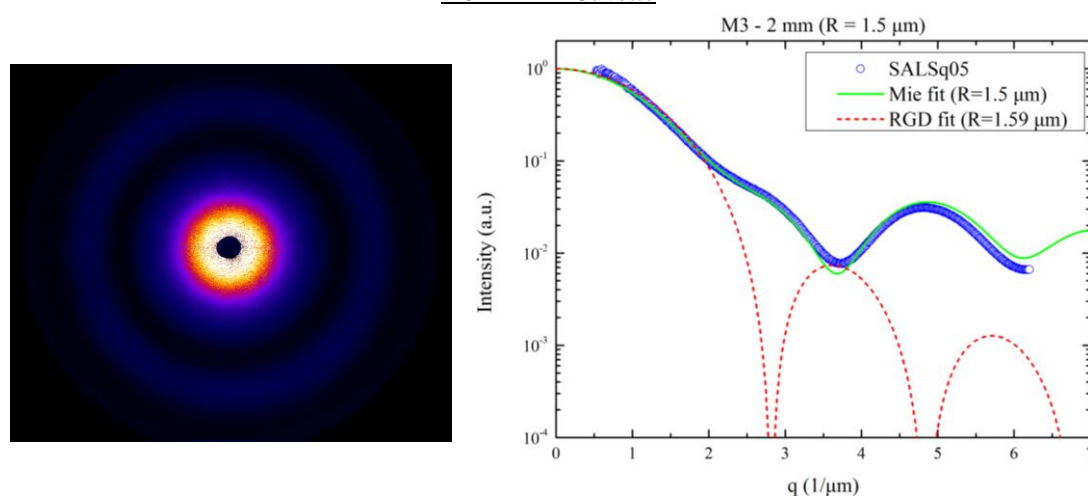


Fig. 4.12 Subtracted scattering pattern image of M3 sample measured in a 2mm sample thickness cuvette with SALSq05 setup (left). Experimental radially averaged scattered intensity versus scattering vector (right, \circ) and fitted curves according to Mie (right, green solid line) and RGD (right, red dashed line) theory.

Finally PMMA spherical particles of 640 nm nominal radius diluted in dodecane solvent, were measured. This measurement was implemented on the rheometer, having 1 mm sample thickness. The results of this measurement after image data analysis are presented in Figure 4.13. The final result of the Mie fit gives a particle radius of $R = 0.64 \mu\text{m}$. The fit is excellent and the result is an exact match to the nominal radius value. This time, the RGD fitted curve shows a good agreement to the respective Mie one throughout the scattering angles experimental window, since the refractive index contrast between the particles ($n_{\text{particle}} = 1.493$) and the solvent ($n_{\text{solvent}} = 1.42$) is relatively small.

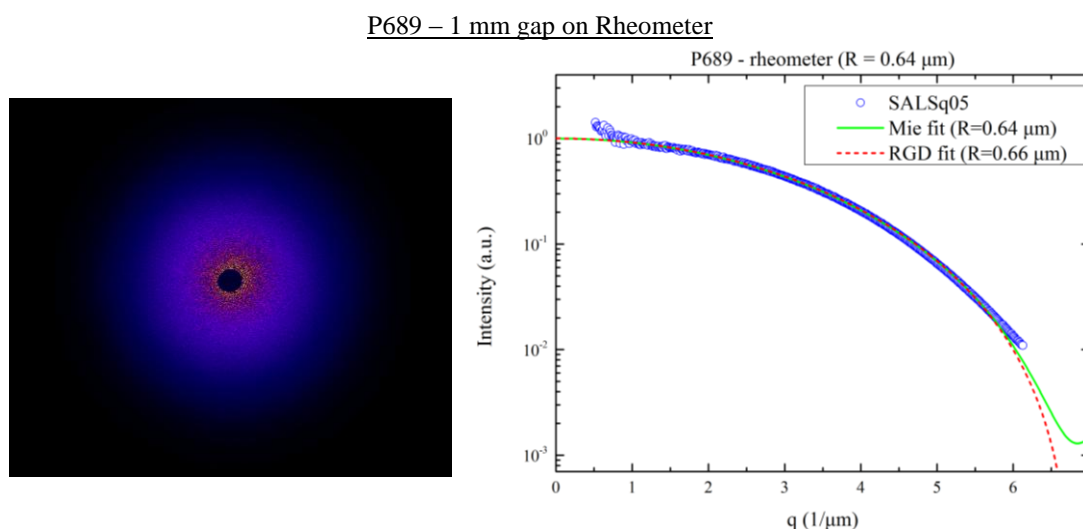


Fig. 4.13 Subtracted scattering pattern image of P689 sample measured on a rheometer having 1 mm sample thickness with SALSq05 setup (left). Experimental radially averaged scattered intensity versus scattering vector (right, \circ) and fitted curves according to Mie (right, green solid line) and RGD (right, red dashed line) theory.

As mentioned in the “*Samples*” section, the nominal radius for the sample P689 was experimentally measured using a conventional static light scattering ALV goniometer apparatus. Since the ALV goniometer measurement was conducted at the same wavelength with the SALSq05 setup ($\lambda = 532 \text{ nm}$), it was possible to combine both measurements and plot the full form factor of the sample (Fig. 4.14). The agreement of the two different setups in the small overlapping region, after normalizing the SALS data to the corresponding intensity measured at 20° with the goniometer, is excellent. Fitting the whole scattering profile of the sample to Mie theory extracts a radius value equal to $R_{\text{Mie}} = 0.64 \mu\text{m}$, while fitting it to the RGD theory the extracted radius value is $R_{\text{RGD}} = 0.68 \mu\text{m}$. Although the agreement between the RGD and Mie fits only to the SALS data was good, at higher scattering angles ($\theta > 20^\circ$) discrepancies appear, resulting in the particles’ size overestimation, despite the small refractive index contrast between the particles and the solvent.

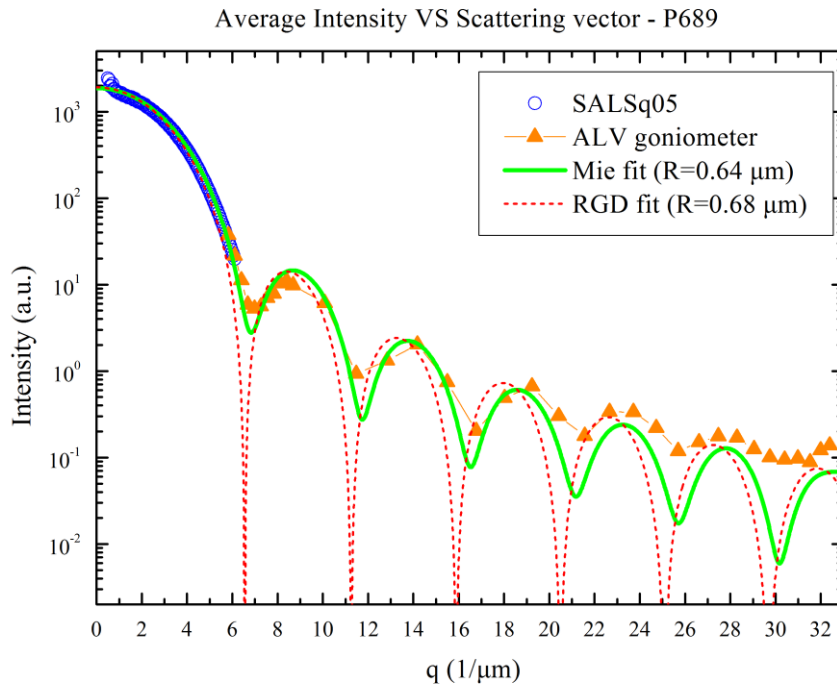


Fig. 4.14 Normalized average scattered intensity of P689 sample versus scattering vector experimentally measured with SALSq05 setup for 2-21 degrees (\circ) and with an ALV goniometer for 20-160 degrees (\blacktriangle). The green solid line represents the fitted curve according to Mie theory, while the red dashed line represents the fitted curve according to RGD theory.

Conclusions

A series of evaluation tests were carried out using the SALSq05 apparatus to verify its ability to perform small angle static light scattering measurements with real 3D scatterers and provide reliable measurements.

The evaluation tests involved dilute colloidal suspensions with:

- Different sample thicknesses.
- Measurements with cuvettes and on rheometer.
- Different particle sizes and materials.
- Different solvents.

All the experimentally measured radii values, by fitting the experimental curves with Mie and Rayleigh-Gans-Debye theoretical models as well as the straightforward calculation of the radius using the 1st minimum position (fulfilling $R = 4.49/q_{(1st\ min)}$), compared to the corresponding nominal values are shown in Figure 4.15. It can be easily noticed that Mie theory is the most applicable for the specific measured samples, although RGD theory can also be used for the smaller particles.

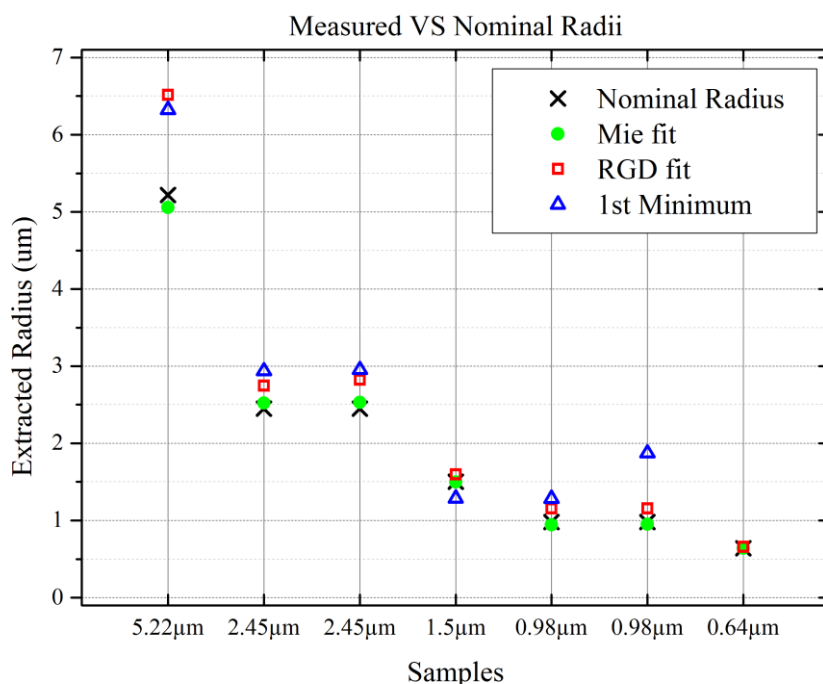


Fig. 4.15 Experimentally measured radii for the samples PS10, PS5, PS2, M3 and P689 extracted using Mie theory (●), RGD theory (□) and the position of the 1st minimum (Δ), and known nominal radii values (x).

A more detailed estimate of the SALSq05 measurement results, according to each previously mentioned ways of radius extraction, can be seen in Figure 4.16. There, the percentage deviation from the nominal radius value as a function of radius of the experimentally measured radii for all the samples, extracted using Mie theory, RGD theory and the position of the 1st minimum, are presented.

The radius estimation through the 1st minimum is obviously not accurate, since the minima are seriously affected by the increasing refractive index contrast between the particles and the solvent, even with small particles, resulting up to 30% deviation. Values extracted through RGD theory have a maximum deviation of 25% for the larger particles ($R = 5.22 \mu\text{m}$), decreasing to less than 5% for the smaller ones ($R = 0.64 \mu\text{m}$). RGD theory should be used with caution and considering its required criterion.

All extracted radii values, using Mie theory, deviate less than 5% from the company provided nominal ones. Consequently, we can safely declare that the SALSq05 apparatus can perform small angle static light scattering measurements with reliability. It can also be combined with goniometers to create a full form factor profile of a probed sample, since the scattering angles collected ($2^\circ < \theta < 30^\circ$) are overlapping with the lower scattering wavevectors q collected by a light scattering goniometer ($\theta > 20^\circ$).

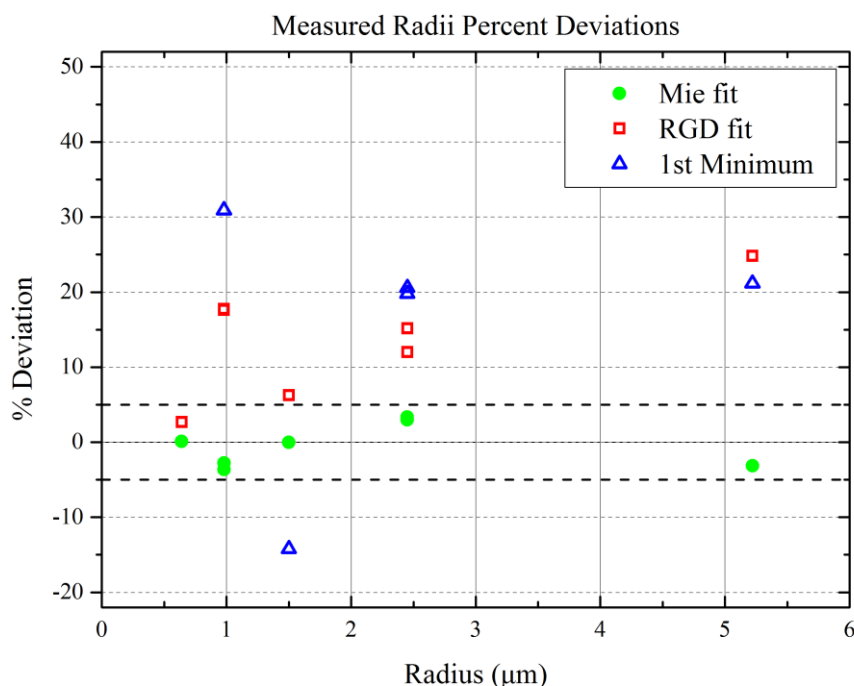


Fig. 4.16 Percentage Deviation from company provided nominal size as a function of radius of the experimentally measured radii for the samples PS10, PS5, PS2, M3 and P689 extracted using Mie theory (●), RGD theory (□) and the position of the 1st minimum (▲).

The capabilities of the SALSq05 apparatus can be numerous when combined with a rheometer. In chapter 5 “Concentrated Colloidal Suspensions”, some of these capabilities are presented as preliminary feasibility of various interesting applications that can be implemented with the use of this setup.

4.5 Dark Field Microscopy (DFM)

As described in Chapter 3 “Development” the SALSq05 setup has a mode-2 version, in which, with the addition of an optical extension before the camera, images now the sample itself. Using spatially extended incoherent source of illumination (3W white LED zoom torch), replacing the laser, the light rays (parallel) that pass through the sample without being scattered from the particles are blocked by the beam stop, while the scattered light from the particles creates a dark field image of them on the CCD sensor.

The magnification of the resulting microscope is relatively small (x4.25). The instrument, being optimized for the SALS mode and having the current space limitations, cannot achieve higher magnification. but used on the rheometer can become a very useful tool. In Figure 4.17 is shown an image of a 100 lines/mm graticule, with 10 μm line spacing. The lines are easily distinguished, since the

system's resolution is $\sim 4 \mu\text{m}$. To show the capabilities of this version, a sample of $5.22 \mu\text{m}$ radius polystyrene spherical particles diluted in pure water was loaded on the rheometer and imaged. The sample was not well dispersed so aggregates are formed, as seen in Figure 4.18. The SALSq05 mode-2 setup, when mounted on the rheometer, can image the loaded sample at planes from 0 to 1 mm from the top of the bottom plate upwards in the z direction. By slightly moving the whole setup the imaging plane changes, while the z-scan is limited by the thickness of the bottom plate.

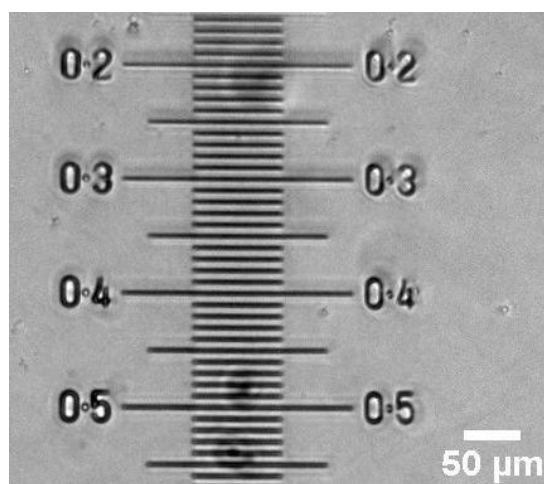


Fig. 4.17 Image of a 100 l/mm graticule, acquired with the SALSq05 mode-2 apparatus. The space between the lines is $10 \mu\text{m}$.

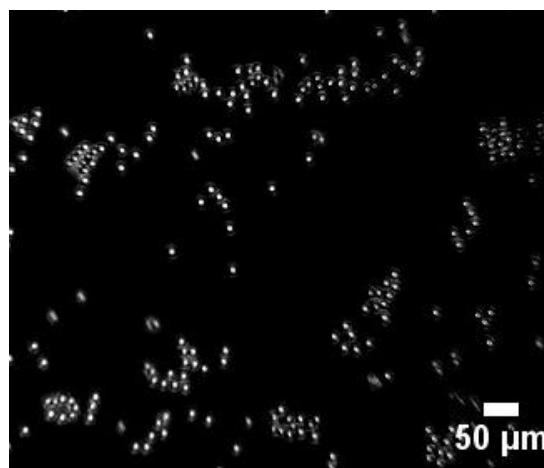


Fig. 4.18 Image of $5.22 \mu\text{m}$ radius spherical polystyrene particles diluted in pure water loaded on a rheometer, acquired with the SALSq05 mode-2 apparatus.

This mode-2 version of SALSq05 apparatus, imaging the sample on a rheometer while being manipulated, would be advantageous if implemented at the same time with the original version, imaging the scattering vectors. That way, a better understanding of a rheologically treated sample would be possible, especially when probing aggregation or crystallization phenomena.

CHAPTER 5

CONCENTRATED COLLOIDAL SUSPENSIONS

Since the SALSq05 setup was validated through dilute colloidal suspension measurements providing characterization of particle size, we extended our studies to further possible application with concentrated colloidal suspensions, to show the setup's capabilities. Systems of higher volume fraction were measured, through Static Light Scattering (SLS) at rest, to extract the structure factor induced by interparticle interactions and under shear, to visualize the effect of shear on them. The Diffusing Wave Spectroscopy (DWS) capabilities of the setup's mode 2 version were also tested. The results presented in this chapter are only preliminary results.

5.1 Static Light Scattering (SLS)

Static Light Scattering measurements were performed on the *Anton Paar MCR 302 WESP* rheometer, with the use of SALSq05 apparatus. The probed samples were PMMA spherical particles ($n_{particles} = 1.493$) of 640 nm radius, named ASM84, in squalene solvent ($n_{solvent} = 1.495$). The solvent was chosen to have a refractive index very close to the one of the probed particles for the sample to remain relatively transparent, thus in the single scattering regime. Three samples were prepared and stored at room temperature. The difference among the three samples was volume fraction (ϕ), covering values from $\phi = 0.59$ and $\phi = 0.51$, down to the dilute case with $\phi = 0.05$. The samples were measured at rest, while the sample with volume fraction $\phi = 0.59$ was tested under shear as well.

5.1.1 Measurements At Rest

Following the measurement procedure described in section 4.2 “*Measurement and Analysis*” for each one of the three samples, the scattering pattern of each was generated, as presented in Figure 5.1. The exposure time of the camera for all measurement was the same (5 ms) for better comparison. This exposure time was chosen, despite the fact that there was some saturation in very low angles (close to the beam stop), to acquire a stronger overall signal, since the refractive index matching results in decreased scattering intensities.

The averaged scattered intensity from homogenous particles, as a function of the scattering vector q , is proportional to their number N , their form factor $P(q)$ and their structure factor $S(q)$.

$$\langle I(q) \rangle \propto N P(q) S(q) \quad (5.1)$$

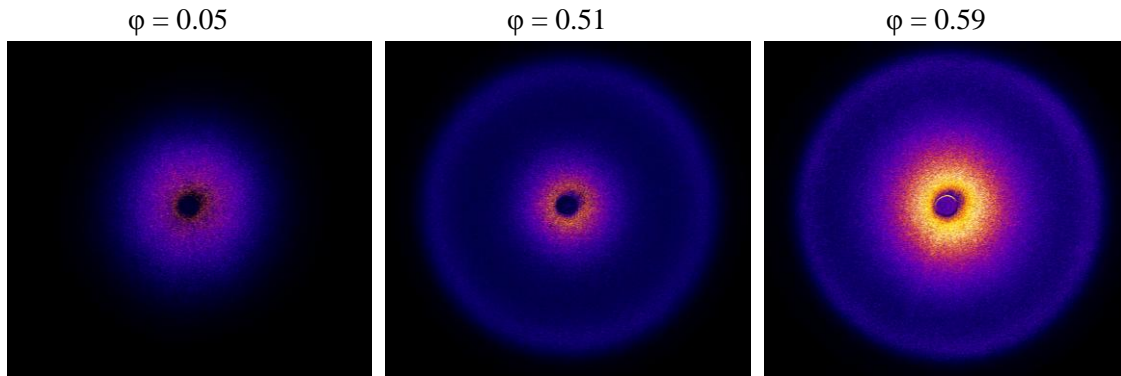


Fig. 5.1 Small angle light scattering patterns acquired with SALSq05 setup on a rheometer for samples of different volume fractions (ϕ). The samples were PMMA spheres ($R = 640$ nm) in squalene solvent.

The dilute scattering pattern (Fig. 5.1 left) contains only the form factor $P(q)$ of the sample, i.e. the scattering generated by the size and shape of the particles alone, since the particles are far enough from each other, compared to the wavelength of the laser beam. On the contrary, the higher volume fraction scattering patterns (Fig. 5.1 center and right) appear to lead to an overall increase of the scattered intensity. This is due to the presence of more effective scatterers and the appearance of a second annulus peak at a higher angle of the experimental window. This annulus is caused by the structure factor $S(q)$, i.e. the scattering generated by interparticle interactions, since at these volume fractions the particles are not far enough from each other, compared to the wavelength of the laser beam. Radially averaging the scattering pattern of each sample and plotting it as a function of scattering vector (q), gives us a more clear view of the volume fraction effect (Fig. 5.2).

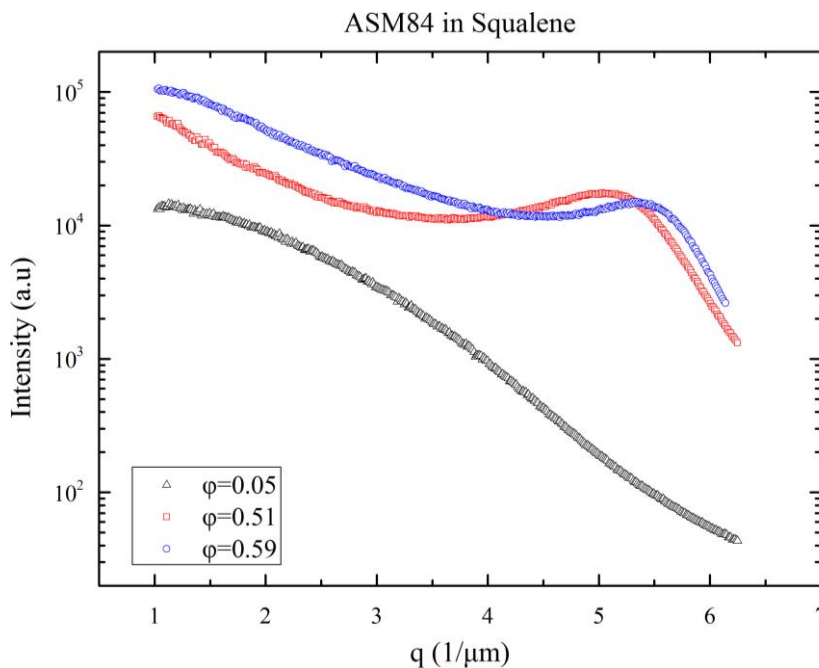


Fig. 5.2 Radially averaged scattered intensity (I) versus scattering vector (q) for samples of different volume fractions (ϕ). The samples are PMMA spheres ($R = 640$ nm) in squalene solvent.

In Figure 5.2 the dilute sample curve ($\phi = 0.05$) contains the form factor of the corresponding sample ($S(q) = 1$), while the higher volume fraction curves ($\phi = 0.51$, $\phi = 0.59$) contain both the form factor and the structure factor of each sample. In order to extract the structure factors from these data, each of the two curves were divided by the dilute one and corrected for the respective volume fraction, since the form factor is the same for all three samples. This way the structure factor $S(q)$ of each sample is revealed, as seen in Figure 5.3. The peak of the structure factor is moving to higher qR values as the volume fraction increases, since distances between the particles become more narrow. To validate the results, each structure factor was plotted together with the equivalent values estimated using the Percus – Yevick model for hard sphere suspensions⁴² (Fig. 5.4). The fit is excellent, denoting that the SALSq05 apparatus can reliably perform absolute measurements of the structure factor.

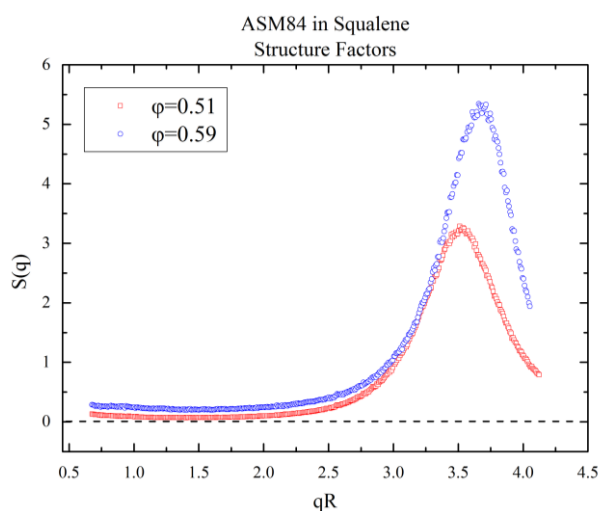


Fig. 5.3 Structure factors versus qR of samples with different volume fractions (ϕ). The samples were PMMA spheres ($R = 640$ nm) in squalene solvent.

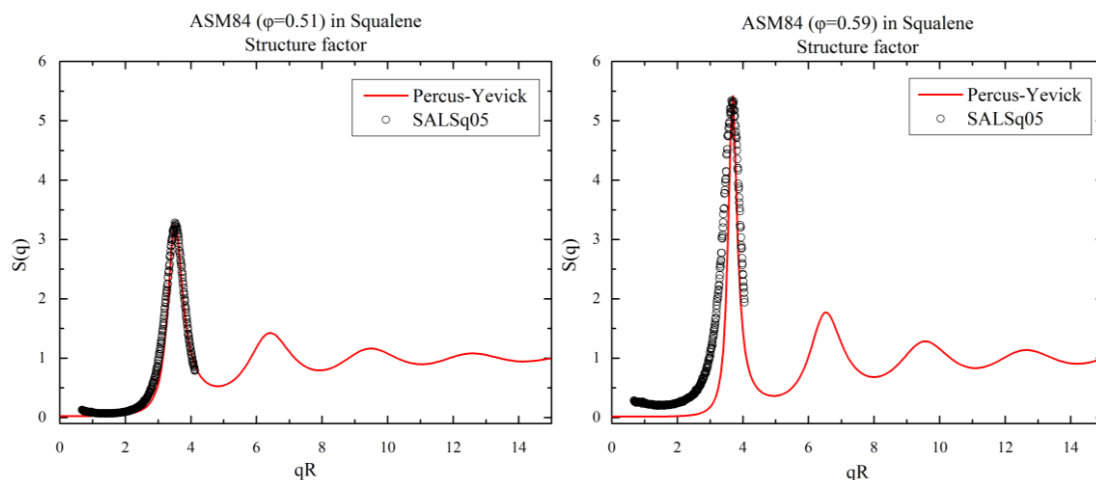


Fig. 5.4 Structure factor versus qR of samples of volume fraction $\phi = 0.51$ (\circ top) and $\phi = 0.59$ (\circ bottom) measured with the SALSq05 apparatus and equivalent Percus-Yevick theoretical values (red solid line). The samples were PMMA spheres ($R = 640$ nm) in squalene solvent.

5.1.2 Measurements Under Shear

Concentrated colloidal suspensions of hard sphere particles have been shown to present shear induced crystallization⁴³, resulting in scattering patterns with Bragg peaks caused from the crystal. Some preliminary experiments were performed using a concentrated colloidal suspension. The sample consisted of PMMA spherical particles ($R = 640$ nm) in squalene solvent at volume fraction $\phi = 0.59$. The measurement was implemented on the *Anton Paar MCR 302 WESP* rheometer using parallel glass plates. The sample, of 0.5 mm thickness, was set under oscillatory shear at 1000% shear strain and frequency $1 \text{ rad}\cdot\text{s}^{-1}$. A series of 100 images, captured at a framerate of 10 frames per second, were analyzed in *ImageJ*.

During the oscillatory shear the scattering pattern was changing periodically, denoting particle ordering structural changes in the sample. For comparison, in Figure 5.5 the averaged scattering patterns acquired by the dilute sample (a), the sample with volume fraction $\phi = 0.59$ at rest (b), the same sample under oscillatory shear (c) and an image where we subtract the image of the sample at rest from that under shear (c) are presented.

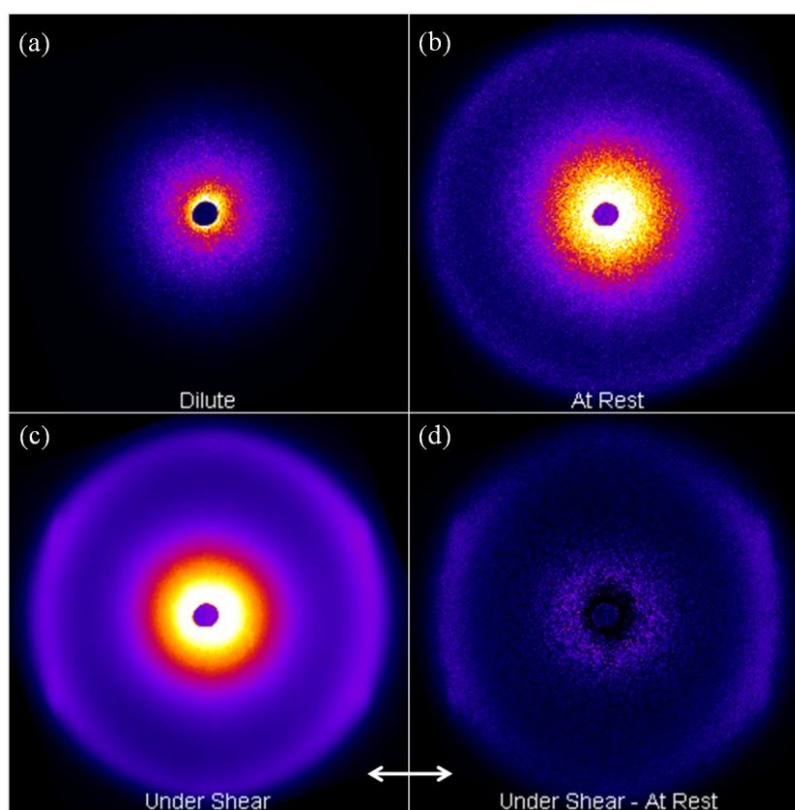


Fig. 5.5 Averaged scattering patterns acquired with SALSq05 on a rheometer and produced by the dilute sample ($\phi = 0.05$) at rest (a), the sample with $\phi = 0.59$ at rest (b) and the sample with $\phi = 0.59$ under oscillatory shear (c). Bottom right (d) is the sample with $\phi = 0.59$ under oscillatory shear after subtraction of the equivalent values measured at rest. The sample was PMMA spheres ($R = 640$ nm) in squalene solvent. The arrow indicates shear direction.

Four small broad regions of increased intensity can be observed (Fig. 5.5 c,d). These are caused by the partial crystallization of the sample, due to the inhomogeneous strain introduced when using parallel glass plates. A full crystallization would lead to a formation of localized intense peaks, known as Bragg peaks, as observed by Koumakis et al (2008)⁴³ where a cone-plate geometry was used. SALSq05 setup can be adapted to work with con-plate by slightly changing the incident beam alignment to account for the angle change introduced by the cone.

To better visualize various aspects of the shear effect on the scattering pattern, images of the minimum, maximum, average and standard deviation of the scattering pattern sequence acquired under oscillatory shear, after subtraction of the equivalent “at rest” values, were retrieved (Fig. 5.6). The full analysis of such experiments is beyond the scope of this thesis, though some points can be noted. Observing Figure’s 5.6 maximum (b) and standard deviation images (c), a “line” of relatively higher intensities can be recognized. At the same direction the minimum image (a) has an identical dark one. This direction can be identified as the direction vertical to the one of the oscillatory shear (white arrow). Similarly to the way light is diffracted by a slit transversely to it, the flow of the particles produce a greater intensity variation in the transverse direction. Remarkably, this dynamic effect of flow on the scattering pattern over time, cannot be identified in the averaged image. This may be a drawback of the standard deviation alternative way of analysis described previously, or a useful tool when flow is to be examined.

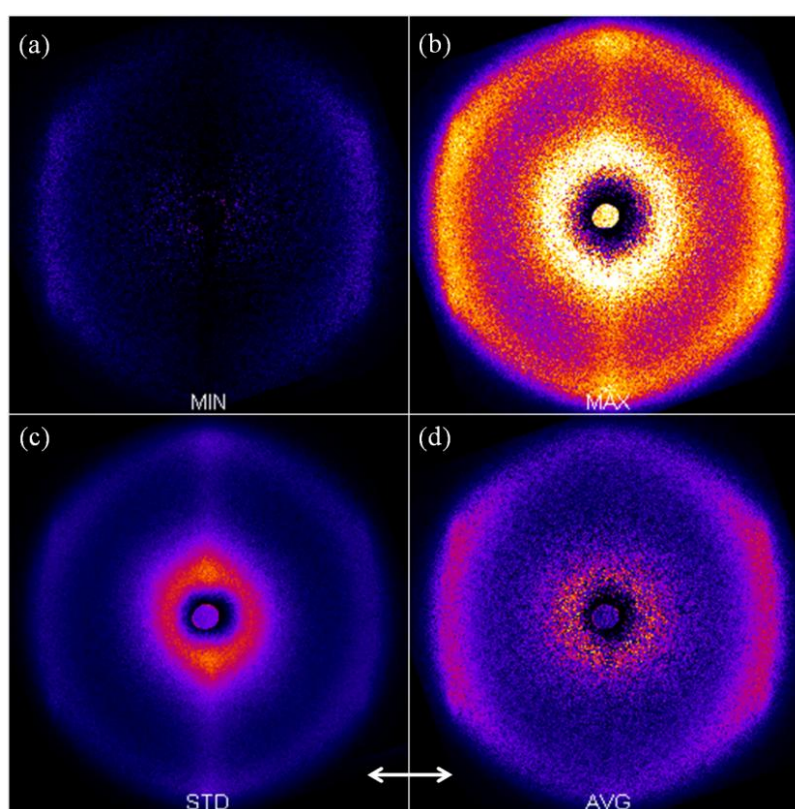


Fig. 5.6 Minimum (a), maximum (b), standard deviation (c) and average (d) of the scattering pattern acquired with SALSq05 on a rheometer and produced by a sample under oscillatory shear, after subtraction of the equivalent values measured at rest. The sample was PMMA spheres ($R = 640$ nm) in squalene solvent with volume fraction $\phi = 0.59$. The arrow indicates shear direction.

The change in the structure, induced by the oscillatory shear, can be clearly observed in Figure 5.7, where the form factor has been removed. The averaged scattering patterns of the “at rest” and “under shear” measurements have been divided by the corresponding average of the “dilute” one, producing images of the structure factor alone in space for each condition. Comparing the two structure factors, an obvious change is apparent when shear is applied, caused by particles’ ordering and partial crystallization.

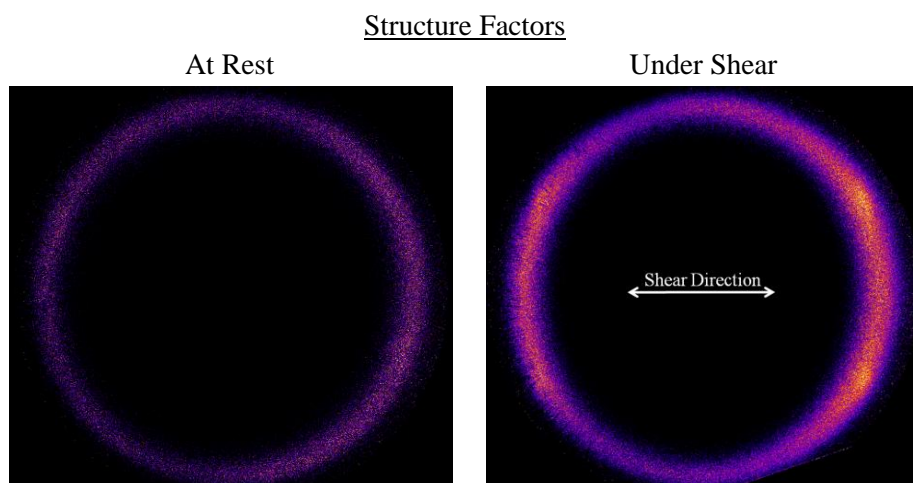


Fig. 5.7 Structure factor images of PMMA spherical particles ($R = 640$ nm) in squalene solvent at volume fraction $\phi = 0.59$, measured with SALSq05 setup on a rheometer, at rest (left) and under oscillatory shear (right). The arrow indicates shear direction.

A very interesting aspect is revealed when the structure factor is calculated using the STD of the images. Figure 5.8 shows the STD of the scattering pattern under shear minus that at rest and then divided by the STD of the dilute. This image can be assessed to be the STD of the structure factor under shear. This time, one can identify six small regions of higher intensities, more similar to the expected Bragg peaks in the case of full crystallization. In our case a partial crystallization was induced by the shear that can be described by these higher intensity regions of the structure factor STD. Quantifying these regions, by taking the radial distribution of the intensities at $q \cdot R = 3.7$ and in respect to shear direction, the peaks become more apparent, as seen in Figure 5.8 right. Remarkably, the peaks are located exactly at 30° , 90° , 150° , 210° , 270° and 330° , equally spaced by 60° . Furthermore, the minimum intensity is ~ 5.5 , which was the maximum of the structure factor of the same sample at rest calculated in the previous section and found at $q \cdot R = 3.7$.

Again, these are preliminary measurements that need further analysis and quantification. The scope of this section was to bring up some possible interesting applications that SALSq05 setup can perform in combination with rheology.

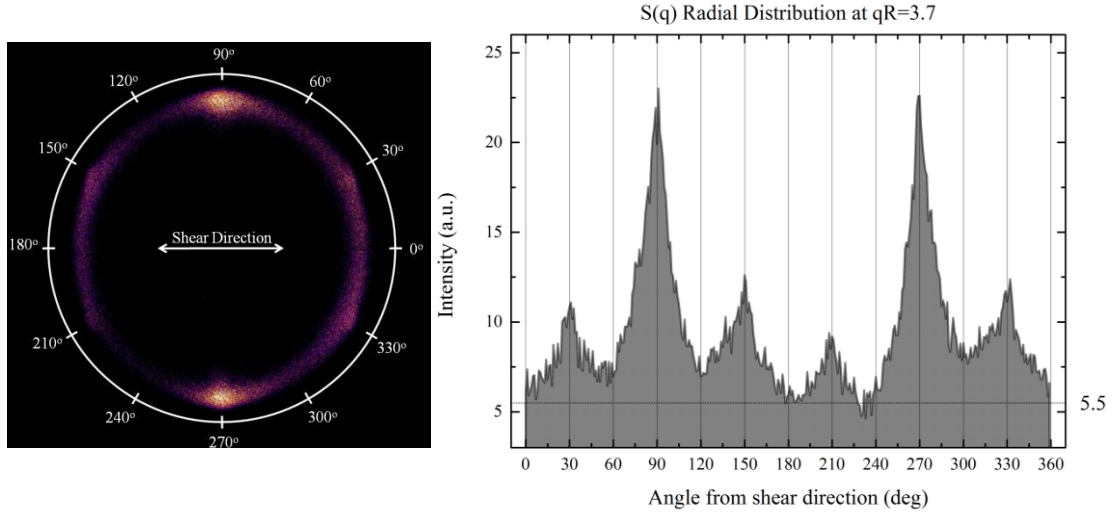


Fig. 5.8 Image of the structure factor STD of PMMA spherical particles ($R = 640$ nm) in squalene solvent at $\phi = 0.59$, under oscillatory shear, measured with SALSq05 setup (left). Structure factor radial distribution at $q \cdot R = 3.7$ in respect to the shear direction (arrow). 5.5 is the $S(q)$ maximum of the sample at rest, found at the same qR .

5.2 Diffusing Wave Spectroscopy (DWS)

Using the SALSq05 mode-2 setup, another possible application was tested. Diffusing Wave Spectroscopy is a dynamic light scattering technique used for optically thick (opaque) media which exhibit a very high degree of multiple scattering and relates the temporal fluctuations of the multiply scattered light to the motion of the scatterers^{44,45}. This technique is implemented either in the backscattering or the transmitted geometry. In our case the transmitted light through an opaque sample was measured. Usually the scattered laser beam is collected and analyzed with a photomultiplier (PMT) that can detect fast dynamics. Though CCD based DWS techniques are also common¹¹, but since they are limited by the sensor frame rate, they are measuring the slow part of a sample's dynamic relaxation.

The temporal fluctuations of the collected scattered intensity I is analyzed through the calculation of the ensemble averaged temporal autocorrelation function of the transmitted intensity⁴⁶.

$$g_2(t, \tau) = \frac{\langle I(t)I(t+\tau) \rangle}{\langle I(t) \rangle \langle I(t+\tau) \rangle} \quad (5.1)$$

where t is the time when the reference intensity is measured and τ is the delay time. Brackets denote averaging.

The Diffusing Wave Spectroscopy measurements were performed on the *Anton Paar MCR 302 WESP* rheometer, with the use of SALSq05 mode-2 setup. For the collection of light a *Basler A311f* camera or a *Correlator Single Photon Detector Module PMT-120B* with an optical fiber placed on the CCD sensor plane, was used. The probed sample consisted of PMMA spherical particles ($n_{particles} = 1.493$) of radius $R = 640$ nm, named ASM84, in octadecene solvent ($n_{solvent} = 1.471$) at volume fraction $\varphi = 0.5$. The solvent was chosen so that the particle - solvent refractive index contrast is high enough for the sample to be opaque and thus in the multiple scattering regime. The sample was prepared, stored at room temperature and finally measured and analyzed using both the correlator and the camera. For the camera analysis, 50000 frames of a 156x82 pixels region (Fig. 5.9 inset) were captured at a framerate of 82 frames per second. In Figure 5.9, the corresponding correlation functions are presented.

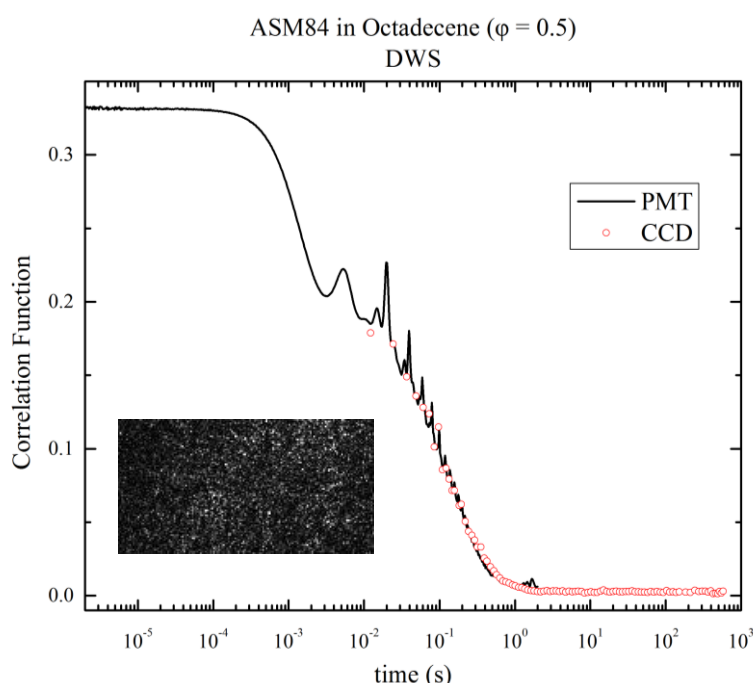


Fig. 5.9 Correlation functions of PMMA spherical particles ($R = 640$ nm) in octadecene on a rheometer, produced through SALSq05 mode-2 DWS measurements with a photomultiplier (black solid line) and a camera (\circ). Inset shows an image of the speckles acquired.

Although the photomultiplier (PMT) measurement was affected by periodic mechanical vibrations in the setup (probably caused by the rheometer's fan), the two measurements seem to follow the same trend, denoting the reliable Diffusing Wave Spectroscopy measurements SALSq05 mode-2 setup can perform, becoming a useful tool for studying slow relaxation and time-dependent dynamics.

All measurements presented in this chapter are preliminary, further tests and analysis will be performed in the near future.

CHAPTER 6

CONCLUSIONS

In this work, the development and optimization of a compact, high resolution, small angle light scattering (SALS) setup that can be used for rheological applications, was presented. Although the target rheometer, for which the SALS apparatus was designed, is an *Anton Paar MCR-501*, the developed setup can be used with all *Anton Paar MCR* rheometers.

Calculations and simulations were performed in optical design software that offered the opportunity to optimize the system and create a novel layout, suitable for the set objective. A novel SALS layout, featuring telecentricity, was adopted, providing sharper focusing and reduced straylight, as well as the opportunity to approach the optical design in a structured and systematic way. The finally developed SALSq05 setup has a scattering angle range of 2° to 30° , corresponding to a q vector range of $0.4\mu\text{m}^{-1}$ to $6.2\mu\text{m}^{-1}$ and an angular resolution of 0.2° . The optomechanical support of the system is such, to allow for easy alignment and adjustment. At the same time, the polarizer and analyzer can be set as required, to conduct polarized or depolarized SALS measurements (VV, VH, HH, HV). Furthermore, with the addition of an extra optical component, the system is utilized as a microscope. In this mode, the setup images the sample with a $\times 4.25$ magnification and $4\ \mu\text{m}$ resolving power. Depending on the illumination of the sample, Dark Field Microscopy (DFM) and Diffusing Wave Spectroscopy (DWS) measurements are possible.

The SALSq05 setup was successfully calibrated and verified for its angular performance, with a $100\ \text{l/mm}$ diffraction grating and a $10\ \mu\text{m}$ diameter pinhole, showing excellent linearity. Its scattered intensity distribution performance was also tested with a ground glass diffuser and a novel way of correction, accounting for sample's thickness and vignetting, was produced.

A series of evaluation tests were carried out to verify the system's ability to perform SALS measurements with real 3D scatterers and export reliable results. These evaluation tests involved measurements of dilute colloidal suspensions with different sample thicknesses, in cuvettes and on a rheometer, different particle sizes and materials and different solvents. All results were in excellent agreement with the expected values. Thus the SALSq05 setup can reliably perform SALS measurements, even under several different conditions. Measurement analysis was implemented with homemade software that was developed to accompany SALSq05 setup, having a user friendly graphic interface and various capabilities.

Furthermore, an alternative novel way of analysis, using the standard deviation of the sample's scattering pattern, was tested and turned out to be very promising. Not needing for an extra solvent measurement, it allows for inline and flow measurements. Nevertheless, further testing is required to validate this kind of analysis.

In combination with rheology, the setup's capabilities are numerous. Systems of higher volume fractions ($\phi = 0.51$, $\phi = 0.59$) were measured, through Static Light Scattering (SLS) at rest, and their structure factors were extracted with absolute agreement with the expected ones. Thus SALSq05 apparatus can reliably perform absolute measurements of the structure factor. Furthermore, a sample with volume fraction $\phi = 0.59$ was measured under oscillatory shear and the effect of the shear on its structure factor was visualized. The Dark Field Microscopy and the Diffusing Wave Spectroscopy capabilities of the SALSq05 mode-2 version were also tested with success.

There are some possible future modifications and improvements that could be useful and advantageous for the developed setup. One of them is the necessity to synchronize the SALS data with the respective rheometric data, in order to easily evaluate SALS changes induced by rheological manipulation of the sample. Another improvement could be the combination of the two versions of SALSq05 setup in one. This would give the possibility to image a sample, loaded on a rheometer, while being manipulated, at the same time with SALS measurements. Such a setup would provide a better understanding of a rheologically treated sample, especially when probing aggregation or crystallization phenomena.

Although application measurements in concentrated colloidal suspensions presented were preliminary and trial, they can support the promising capabilities of this apparatus, since it can reliably perform Static Light Scattering (**SLS**), Dynamic Light Scattering (**DLS**) (not presented but can be performed), Diffusing Wave Spectroscopy (**DWS**) and Dark Field Microscopy (**DFM**) in combination with rheology. This multi-functionality of the setup provides the opportunity with a single instrument to probe a wide variety of samples (transparent and opaque) using different techniques. This combination of rheology with SLS, DLS, DFM or DWS through a single apparatus makes this setup a unique tool for laboratory and industrial use.

APPENDIX

CAMERA EVALUATION

The *Point Grey Grasshopper 14S3* camera was tested for its linearity intensity performance.

Linearity over the Exposure Time. (Fixed Intensity)

The camera was placed with a plain white paper in front, at a distance of 20cm from a black surface that was illuminated by a 12w halogen lamp. 50 frames at 5fps were captured with different exposure times, varying from 0.004ms to 20ms until the camera was saturated. All other camera settings were set to absolute.

Afterwards, 50 frames were captured with the camera sensor blocked and an exposure time of 0.004ms to define the dark noise. There was no difference of the mean dark noise counts when the exposure time was altered, so this dark noise applies for all exposure times.

Using ImageJ the 50 frames for each exposure were averaged (I) and from each one of them the average of the 50 dark frames (DN) was subtracted ($I-DN$). The averaged intensity of each result image was calculated and is shown in Figure A.1.

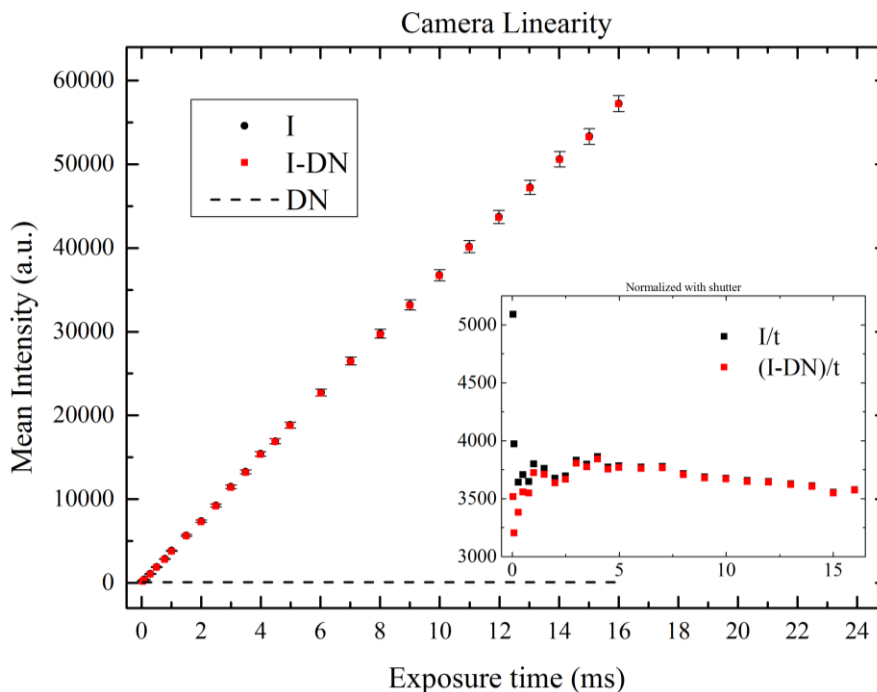


Fig. A.1 Averaged intensity of a black illuminated surface acquired with the camera, for different exposure times (\bullet), after dark noise subtraction (\blacksquare) and dark noise ($---$). The inset shows the same values normalized with exposure time.

The inset in Figure A.1 shows the averaged intensity for each exposure normalized over the exposure time. The camera's linearity appears to be relatively good, since increasing the exposure time the intensity captured increases linearly. Although the normalized values shown in the inset of Figure A.1 should ideally be a straight horizontal line, they appear to be within ± 100 counts over the 65536 total available counts of a stored image, thus within $\pm 0.1\%$. A small deviation appears to take place in small exposure times due to the fact that the measured intensities were comparable to the dark noise values making such measurements unreliable.

Linearity over the Intensity. (Fixed Exposure Time)

An additional study for camera's linearity was done by projecting known interference pattern on the CCD sensor. The interference pattern was generated by two pinholes on an aluminum sheet illuminated by a laser beam. The configuration was similar to the Young's double-slit experiment³⁵. This interference pattern is a result of the superposition of overlapping light waves originating from the two pinholes, as seen in Figure A.2.

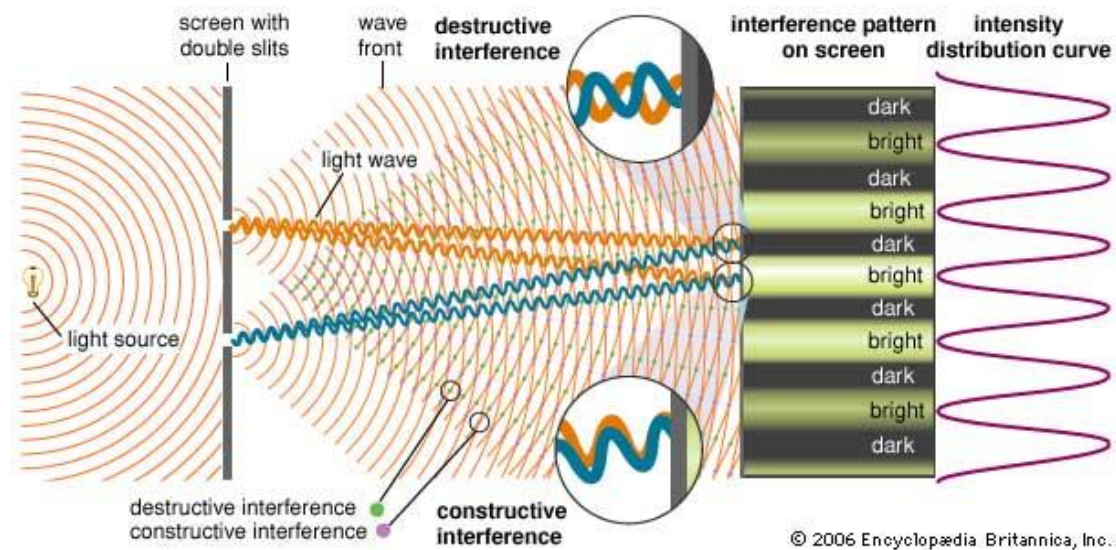


Fig. A.2 Young's double slit experiment.

The intensity distribution in this case follows a sinusoidal curve.

$$I = I_1 + I_2 + 2\sqrt{I_1 I_2} \cos\left(\frac{2\pi}{\lambda} \cdot r + \varphi_o\right) \quad (\text{A.1})$$

The CCD sensor was placed about a meter away from the pinholes, to resolve enough fringes to analyze. Three images with 1ms exposure time were captured, one for each pinhole (I_1 , I_2) and one for both (I_{12}) as seen in Figure A.3.

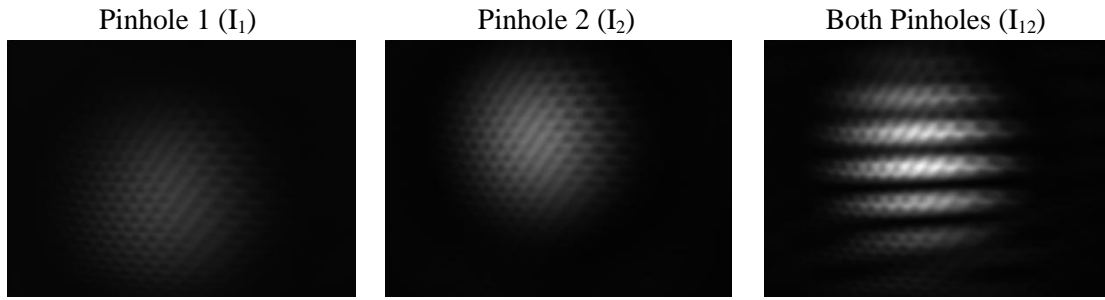


Fig. A.3 Images captured from illuminated pinholes.

After normalizing for the intensity envelope of the two pinholes, the phase of the resulting interference was extracted as shown in Figure A.4, using equation A.2.

$$\theta(px) = \cos^{-1} \left[\frac{I(px) - I_1(px) - I_2(px)}{2\sqrt{I_1(px) \cdot I_2(px)}} \right] \quad (\text{A.2})$$

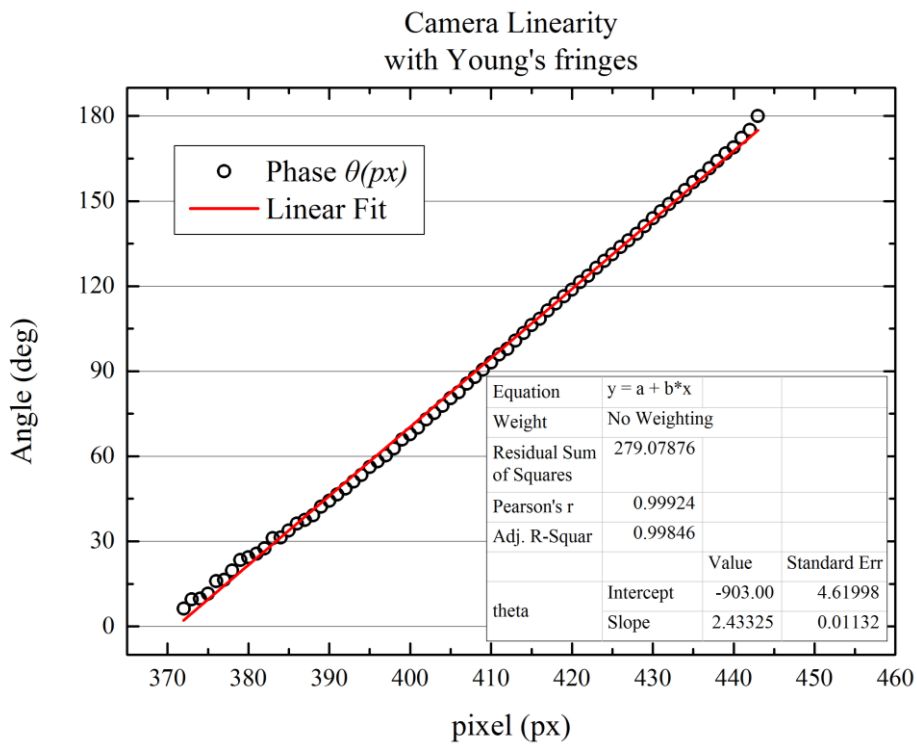


Fig. A.4 Extracted phase from interference pattern from two pinholes illuminated by a laser source, projected on the camera (o) and linear fit (red line).

The camera appears to respond linearly in known variations of light intensity, since the phase in Figure A.4 changes in a linear fashion over pixel distance, as expected.

BIBLIOGRAPHY

1. Black, D. L., Mcquay, M. Q. & Bonin, M. P. Laser-based techniques for particle-size measurement: A review of sizing methods and their industrial applications. *Prog. Energy Combust. Sci.* **22**, 267–306 (1996).
2. Jones, A. R. Light scattering for particle characterization. *Prog. Energy Combust. Sci.* **25**, 1–53 (1999).
3. Poon, W. C. K. & Haw, M. D. Mesoscopic structure formation in colloidal aggregation and gelation. *Adv. Colloid Interface Sci.* **73**, 71–126 (1977).
4. Fuller, G. G. *Optical Rheometry of Complex Fluids*. (Oxford University Press, 1995).
5. Scharl, W. *Light Scattering from Polymer Solutions and Nanoparticle Dispersions*. (Springer, 2007).
6. Berne, B. J. & Pecora, R. *Dynamic Light Scattering : with applications to chemistry, biology, and physics*. (Wiley, New York, 1976).
7. Tamborini, E. & Cipelletti, L. Multiangle static and dynamic light scattering in the intermediate scattering angle range. *Rev. Sci. Instrum.* **83**, (2012).
8. Stein, R. S. & Srinivasarao, M. Fifty years in light scattering: A perspective. *J. Polym. Sci.* **31**, (1993).
9. Ferri, F. Use of a charge coupled device camera for low-angle elastic light scattering. *Rev. Sci. Instrum.* **68**, 2265–2274 (1997).
10. Cipelletti, L. & Weitz, D. A. Ultralow-angle dynamic light scattering with a charge coupled device camera based multispeckle , multitau correlator. *Rev. Sci. Instrum.* **70**, (1999).
11. Scheffold, F. & Cerbino, R. New trends in light scattering. *Curr. Opin. Colloid Interface Sci.* **12**, 50–57 (2007).
12. Caprinetti, M., Ferri, F., Giglio, M., Paganini, E. & Perini, U. Salt-induced fast aggregation of polystyrene latex. *Phys. Rev.* **42**, (1990).
13. Romo-Uribe, A., Alvarado-Tenorio, B. & Romero-Guzmán, M. E. A small-angle light scattering instrument to study soft condensed matter. *Rev. Latinoam. Metal. y Mater.* **30**, 190–200 (2010).

14. Ferri, F. & Greco, M. Growth kinetics and structure of fibrin gels. *Am. Phys. Soc.* **63**, 1–17 (2001).
15. Nishida, K., Ogawa, H., Matsuba, G., Konishi, T. & Kanaya, T. High Resolution Small-Angle Light Scattering Instrument for Soft Matter Study. *J. Appl. Crystallogr.* **41**, 723–728 (2008).
16. Goodman, J. W. *Introduction to Fourier Optics*. (McGraw-Hill, 1996).
17. Lehner, D., Kellner, G., Schnablegger, H. & Glatter, O. Static Light Scattering on Dense Colloidal Systems : New Instrumentation and Experimental Results. *J. Colloid Interface Sci.* **201**, 34–47 (1998).
18. Nakatani, A. I., Waldow, D. A. & Han, C. C. A rheometer with two dimensional area detection for light scattering studies of polymer melts and solutions. *Rev. Sci. Instrum.* **3590**, (1992).
19. Lauger, J. & Gronski, W. A melt rheometer with integrated small angle light scattering. *Rheol. Acta* **34**, 70–79 (1995).
20. Kume, T., Asakawa, K., Moses, E., Matsuzaka, K. & Hashimoto, T. A new apparatus for simultaneous observation of optical microscopy and small-angle light scattering measurements of polymers under shear flow. *Acta Polym.* **46**, 79–85 (1995).
21. Matsuzaka, K. & Hashimoto, T. A rheo-optical apparatus for simultaneous detection of rheology , small-angle light scattering , and optical microscopy under transient , oscillatory , and continuous shear flows. *Rev. Sci. Instrum.* **70**, 2387–2397 (1999).
22. Rheometers with SALS add-on. at <www.anton-paar.com>
23. Bohren, C. F. & Huffman, D. R. *Absorption and Scattering of Light by Small Particles*. (Wiley, New York, 1983).
24. Kerker, M. *The Scattering of Light*. (Academic Press, New York, 1969).
25. Berg, J. C. *An Introduction to Interfaces and Colloids: The Bridge to Nanoscience*. (World Scientific, 2010).
26. Podzimek, S. *Light Scattering, Size Exclusion Chromatography and Asymmetric Flow Field Flow Fractionation: Powerful Tools for the Characterization of Polymers, Proteins and Nanoparticles*. (Wiley, New York, 2011).
27. Van de Hulst, H. C. *Light Scattering by Small Particles*. (Dover Publications, 1981).
28. Dhont, J. K. G. *An Introduction to Dynamics of Colloids*. (Elsevier, 1996).

29. Pusey, P. N. *Colloidal Suspensions*.
30. Laven, P. Mieplot. at <www.philiplaven.com/mieplot.htm>
31. Maetzler, C. *Matlab function for mie scattering and absorption*. (University of Bern, 2002).
32. Zemax optical design software. at <www.zemax.com>
33. Malacara, D. & Malacara, Z. *Handbook of Optical Design*. (Marcel Dekker, 2004).
34. Hecht, E. *Optics 4th edition*. (Addison Wesley, 2002).
35. *Modern Optical Engineering*. (McGraw-Hill, 2000).
36. Laikin. Lens Design. 506 (2007).
37. *Military Standardization Handbook - Optical Design*. (USA Department of Defense, 1962).
38. Murphy, D. B. *Fundamentals of Light Microscopy and Electronic Imaging*. (Willey-Liss, 2001).
39. Telecentric lens resources. at <www.opto-engineering.com>
40. Optics, imaging and lens resources. at <www.edmundoptics.com>
41. Bohm, G. & Zech, G. *Introduction to Statistics and Data Analysis for Physicists*. (Verlag Deutsches Elektronen-Synchrotron).
42. Percus, J. K. & Yevick, G. J. Analysis of Classical Statistical Mechanis by Means of Collective Coordinates. *Phys. Rev.* **110**, (1958).
43. Koumakis, N., Schofield, A. B. & Petekidis, G. Effects of shear induced crystallization on the rheology and ageing of hard sphere glasses. *Soft Matter* **4**, 2008–2018 (2008).
44. Weitz, D. A., Zhu, J. X. & D, D. J. Diffusing-Wave Spectroscopy : The Technique and Some Applications. *Phys. Scr.* **49**, 610–621 (1993).
45. Pine, D. J., Weitz, D. A., Zhu, J. X. & Herbolzheimer, E. Diffusing-wave spectroscopy : dynamic light scattering in the multiple scattering limit. *J. Phys.* **51**, 2101–2127 (1990).
46. Viasnoff, V., Lequeux, F. & Pine, D. J. Multispeckle diffusing-wave spectroscopy: a tool to study slow relaxation and time-dependent dynamics. *Rev. Sci. Instrum.* **73**, 2336–2344 (2002).

